Chapter 4

Satellites See the World's Atmosphere

S. A. ACKERMAN,[a,b] S. PLATNICK,[c] P. K. BHARTIA,[c] B. DUNCAN,[d] T. L'ECUYER,[a,b] A. HEIDINGER,[e]
G. SKOFRONICK-JACKSON,[f] N. LOEB,[g] T. SCHMIT,[e] AND N. SMITH[h]

[a] *Cooperative Institute for Meteorological Satellite Studies, University of Wisconsin–Madison, Madison, Wisconsin*
[b] *Department of Atmospheric and Oceanic Sciences, University of Wisconsin–Madison, Madison, Wisconsin*
[c] *Code 610, NASA Goddard Space Flight Center, Greenbelt, Maryland*
[d] *Code 614, NASA Goddard Space Flight Center, Greenbelt, Maryland*
[e] *Advanced Satellite Products Branch, NOAA/NESDIS/STAR/CoRP, University of Wisconsin–Madison, Madison, Wisconsin*
[f] *Earth Science Division, NASA Headquarters, Washington, DC*
[g] *NASA Langley Research Center, Hampton, Virginia*
[h] *Science and Technology Corporation, Columbia, Maryland*

ABSTRACT

Satellite meteorology is a relatively new branch of the atmospheric sciences. The field emerged in the late 1950s during the Cold War and built on the advances in rocketry after World War II. In less than 70 years, satellite observations have transformed the way scientists observe and study Earth. This paper discusses some of the key advances in our understanding of the energy and water cycles, weather forecasting, and atmospheric composition enabled by satellite observations. While progress truly has been an international achievement, in accord with a monograph observing the centennial of the American Meteorological Society, as well as limited space, the emphasis of this chapter is on the U.S. satellite effort.

1. Introduction

Satellite observations have fundamentally transformed how we observe and understand the Earth. From the earliest days of the satellite era, observations have been used to make quantitative measurements of Earth's atmosphere. The modern satellite atmospheric data record includes temperature and moisture soundings, wind fields, trace gas concentrations, cloud and aerosol properties, precipitation patterns, and radiative budgets. This chapter highlights some of the key advancements over the last six decades of atmospheric satellite observations, along with selected examples to demonstrate the importance of space-based assets to our current understanding of the atmosphere. While progress truly has been an international achievement, in accord with a monograph observing the centennial of the American Meteorological Society, as well as limited space, our emphasis is on the U.S. satellite effort.

The notion of viewing the Earth from high above was conceived well before the birth of the American Meteorological Society. The first patent for a camera boosted by a rocket came in 1891 by Ludwig Rohrmann; his concept was for a picture to be taken while the payload floated back to Earth. Alfred Nobel patented a refined version in 1896 for "an improved mode of obtaining photographic maps." Just over a quarter century later in *The Problem of Space Travel: The Rocket Motor*, published in 1928, Herman Potočnik defined the geostationary orbit for use as a communications platform. In 1945, Arthur C. Clarke popularized the orbit in his article "Extra-terrestrial relays: Can rocket stations give worldwide radio coverage?" (Clarke 1945). After World War II, rockets lifted cameras high in the atmosphere to photograph weather systems and demonstrate the potential for weather observations by Earth-orbiting satellites (Wexler 1954).

Inspired by photographs taken during rocket flights, including one that revealed an unknown tropical storm in the Gulf of Mexico, Dr. Harry Wexler commissioned an artist (name unknown) to paint a simulated image of Earth from a satellite 4000 miles above Amarillo, Texas,

---

Corresponding author: Steven A. Ackerman, stevea@ssec.wisc.edu

DOI: 10.1175/AMSMONOGRAPHS-D-18-0009.1

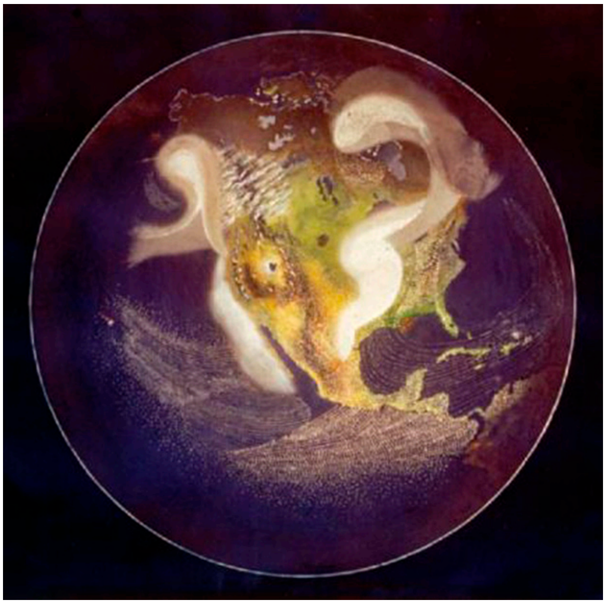

FIG. 4-1. Dr. Harry Wexler, director of meteorological research, U.S. Weather Bureau, commissioned a painting in 1954 to demonstrate the bird's eye view of storms that satellites could provide (image source: https://www.nesdis.noaa.gov/sites/default/files/Wexler%20Drawing.JPG).

at noon on 21 June 1954 (Fig. 4-1). Wexler, the director of meteorological research for the U.S. Weather Bureau (the predecessor to the National Weather Service), was a strong proponent of the possibilities satellites held for weather forecasting and atmospheric research. He hoped the artwork would help inspire others to consider the value of a future weather satellite program.

The beginning of the weather satellite era coincided with the space race in the 1950s. The 1957/58 International Geophysical Year (IGY) gathered the global community (68 nations) in a study of our planet. As a contribution to the IGY, the Soviet Union launched the world's first satellite, *Sputnik*, in October 1957, followed by the United States's first satellite, *Explorer 1*, launched in January 1958. In 1959, *Explorer 7* monitored Earth's heat budget, the first successful remote sensing of Earth from space. These missions transformed how future scientists would study Earth. Since that time there have been vast improvements in instrumentation, data technologies, satellite buses, and observational strategies.

Observational strategies begin with defining an appropriate satellite orbit. Specific scientific objectives can be addressed by a variety of satellite orbits. Satellites in a low-Earth orbit (LEO), nominally altitudes between 300 and 1500 km, provide several advantages for remote sensing instruments, including allowing for high-spatial-resolution observations and unique control over temporal and spatial sampling. The orbital inclination describes the angle between the orbital plane and the equator. A polar-orbiting satellite provides global or near-global sampling and has an inclination angle near ±90°; a subclass is the sun-synchronous orbit, where the inclination is chosen so that the orbital plane precesses at the same rate as Earth's revolution about the sun. The sun-synchronous orbit enables a fixed equatorial local solar time satellite ground track. As an example, the latest series of U.S. operational polar satellites [Joint Polar Satellite System (JPSS)] fly at a nominal altitude, inclination, orbital period, and daytime mean equatorial crossing of 824 km, 98.8°, 101 min, and 1330 local time, respectively. For LEOs in particular, regular adjustments to the orbit are required to compensate for perturbations due to atmospheric drag. Geostationary (GEO) satellites fly at an altitude of approximately 35 800 km above the equator and have an orbital period that matches Earth's rotation so the satellite appears approximately fixed over the equator at a selected longitude. Another orbit type is the highly elliptical orbit (HEO) with a low-altitude perigee (often under 1000 km) and a high-altitude apogee (often over 35 000 km). An example is the Molniya orbit used by Soviet/Russian satellites starting in the 1960s to provide favorable coverage of polar regions not accessible to GEO views. While HEOs have not yet been used for Earth science observations, the utility of such orbits continues to be discussed in the literature (Kidder and Vonder Haar 1990; Trishchenko et al. 2016). Finally, there is a unique perspective provided by a satellite located at the first Lagrange point (L_1), about 1.6 million km from Earth toward the sun. From this relatively stable orbit, Earth-viewing instruments can continually observe the daylit hemisphere of the planet. An example is the National Oceanic and Atmospheric Administration (NOAA)–National Aeronautics and Space Administration (NASA) Deep Space Climate Observatory (DSCOVR) satellite that was launched in 2015. While L_1 missions have primarily been used for heliophysics and space weather observations, DSCOVR was the first platform to include instrumentation for Earth imaging [Earth Polychromatic Imaging Camera (EPIC)] and broadband radiation measurements [National Institute of Standards and Technology Advanced Radiometer (NISTAR)]. Having a novel backscattering solar-view geometry, the potential of this orbit for trace gas, cloud, and aerosol observations is being investigated (Marshak et al. 2018). The optimum orbit of the satellite is partly driven by the research program objectives.

Two research programs of special note in the development of U.S. environmental satellite capabilities include Nimbus and the Earth Observing System (EOS). Both programs flew several satellite missions in polar orbits. Nimbus, a seven-satellite program with launches from 1964 to 1978 (NASA 2014; Ward 2015), played a crucial role in the pathway to sensor development for NASA, NOAA, and the U.S. Geological Survey (USGS) and is discussed further in section 4. EOS had its start in the 1980s, in part, with the recognition of the need for a more integrated, interdisciplinary observation program to better advance Earth system processes and climate science. While considerable programmatic changes occurred over the years, a total of 10 different missions were eventually flown, including the flagship *Terra* (1999), *Aqua* (2002), and *Aura* (2004) satellites. Various EOS sensors are mentioned throughout this chapter. A comprehensive history of EOS can be found in King and Platnick (2018) and 12 collated articles from the EOS Project Science Office *Earth Observer* newsletter (https://eospso.nasa.gov/earthobserver/new-perspectives-eos). Of course, other programs and individual missions have made important contributions to understanding Earth's weather and climate. A view of the history of satellite meteorology could proceed along many paths (e.g., Purdom and Menzel 1996; Smith et al. 1986), including a chronological discussion of satellite missions. The approach taken here is to explore the contributions satellite measurements made to scientific advances in weather and climate sciences.

While the satellite-based scientific advances made over the last several decades are ultimately connected, we have divided this chapter into four broad scientific areas: the radiative energy budget, the hydrological cycle, weather systems and prediction, and atmospheric composition. Observations from satellite missions are required to advance our understanding in these broad areas.

a. Radiative energy budget

There is no more fundamental measure of Earth's climate than the top-of-the-atmosphere (TOA) energy budget. The TOA[1] Earth Radiation Budget (ERB) includes the input of solar energy into the Earth system and the loss of energy to space through reflection of solar radiation and the emission of thermal radiation. Geographic variations in the flow of energy between the sun, the atmosphere, and the surface establish mean atmospheric and oceanic temperature patterns that drive global wind patterns and ocean currents, and dictate the amount of water cycling through evaporation and precipitation processes. As nearly all other aspects of our climate follow from these fundamental quantities, quantifying Earth's energy balance is central to understanding the climate system and predicting the effects of global climate change. Since the first weather satellites were launched, they have played a critical role in shaping our knowledge of the global energy budget.

b. Hydrological cycle

The hydrological cycle describes the circulation of water throughout the Earth system. A major source of atmospheric water vapor is evaporation from the oceans; evapotranspiration from the ground surface and plants is also a key component. Water vapor comprises only 1%–4% (by volume) of the atmosphere, yet it plays a critical role in weather and in Earth's energy balance. Water vapor absorbs and radiates electromagnetic radiation in a broad range of spectral bands that provide the basis for remote sensing of tropospheric and stratospheric water in all its phases. Clouds are critical not only in cycling water through the atmosphere and transporting it throughout the globe, but also in modulating the radiative energy budget of the planet through interactions with solar and infrared (IR) radiation. As a key source of freshwater, precipitation and knowing when, where, and how much it rains or snows around the world is important for science and society. Precipitation also represents an important energy (latent heat) and hydrologic exchange between Earth's atmosphere and its surface. Viewing from above, satellites quantify and monitor global distributions of clouds, precipitation, and atmospheric water vapor (Peters-Lidard et al. 2019).

c. Weather monitoring and prediction

Satellite observations provide a routine global assessment of the atmosphere that is critical to weather forecasting. Their measurements of Earth have revolutionized synoptic meteorology by tracking weather systems and providing information of atmospheric dynamics at spatial and temporal scales impossible from other platforms. Satellite observations are also critical for model initiation and data assimilation in order to resolve the dynamics of weather systems leading to improved forecasts. Today's system of satellites routinely monitors weather patterns across the globe and is an essential component in daily weather briefings and public weather awareness.

d. Atmospheric composition

Aerosols and trace gases influence Earth's weather, air quality, and climate in many ways. The direct cooling effect of aerosols on climate is conceptually well understood, yet the global distribution of aerosol optical parameters needs to be better constrained for climate model assessment. Aerosols in the form of cloud condensation nuclei (CCN) and ice nuclei (IN) can also indirectly affect climate by modifying cloud optical properties and thereby influence a range of cloud

---

[1] In radiation budget studies, the TOA is considered 20 km; above that altitude the optical mass of the atmosphere is negligible.

properties, including radiative properties. Long-term aerosol datasets are needed to help separate anthropogenic aerosol effects from those of natural origin. Specialized satellite sensors are capable of retrieving numerous trace gas species, providing essential information for understanding the quality of the air we breathe at the surface to the state of ozone in the stratosphere.

A wide variety of satellites carry a broad range of instruments that have generated an enormous volume of data. These sensors observe energy using active or passive techniques that are calibrated and georeferenced. In some cases the observed radiances are made into an image. Weather forecasting and briefings make use of animated satellite imagery to monitor atmospheric conditions. Radiances are also directly assimilated in numerical weather prediction models. For many other applications, the measured radiances are transformed into geophysical parameters (e.g., energy flux, temperature profiles, aerosol optical depth) using computer algorithms. These algorithms are grounded in both physical and statistical frameworks. Validation of the algorithm products is achieved through comparison with some combination of ground network observations (e.g., Holben et al. 2001; De Mazière et al. 2018), sondes (e.g., Nalli et al. 2018a,b), airborne (e.g., Cox et al. 1987), and independent satellite methodologies (e.g., Ackerman et al. 2008). Retrieval uncertainty estimates can also be calculated explicitly on a scene-dependent basis within the algorithm itself by using specific covariances for the known error sources, and reporting the uncertainty as a dataset along with the retrieval (e.g., Austin et al. 2009; Poulsen et al. 2012; Platnick et al. 2017).

Observing Earth from satellite platforms has resulted in rapid advances in the study and understanding of Earth system science. This understanding has led to societal benefits such as improved weather forecasting and air quality monitoring.

2. Radiative energy budget

Space-based observations have revolutionized our understanding of Earth's radiative balance by providing the first truly global estimates of the spatial distribution of the net solar and outgoing thermal radiation at the TOA (e.g., Weinstein and Suomi 1961; Raschke and Bandeen 1970; Harrison et al. 1990). One of the first Earthbound satellite missions was to observe the ERB.

Launched in 1959 and carrying a flat plate radiometer developed by Verner Suomi and Robert Parent (House et al. 1986), *Explorer 7* provided the first successful measurements of the ERB from space. In early spacecraft, moving parts were avoided as much as possible; Suomi and Parent created a simple design consisting of two pairs of flat plates that were mounted on opposite sides of the spinning spacecraft. One pair was painted black while the other pair was white. The black pair absorbed sunlight, both directly from the sun and reflected from Earth, as well as Earth-emitted radiation. The white pair reflected most sunlight but absorbed Earth-emitted radiation. The temperatures of these flat plates were measured and then thermal balance equations were used to calculate the amount of sunlight and Earth-emitted radiation incident on the device. This experiment provided the first crude measurements of Earth's radiation balance and established the important role played by clouds in the radiative energy budget. In the years that followed, we learned that Earth was darker and warmer than ground-based instruments suggested and that the gradient of absorbed solar energy between the tropics and the midlatitudes was much larger than previously thought (Vonder Haar 1994). The Environmental Science Services Administration's *ESSA-5* through *ESSA-9* spacecraft (launched between 1967 and 1969) carried radiometers similar to those on *Explorer 7*.

In 1964 the polar-orbiting Nimbus program was designed to determine the ERB from simultaneous measurements of the incoming solar radiation and the outgoing Earth-reflected and Earth-emitted radiation. Raschke et al. (1973) used *Nimbus-3* observations to estimate Earth's annual global radiation budget, including planetary albedo, absorbed solar radiation, and infrared radiation loss to space at global, hemispheric, and zonal averages. They also presented global maps at a spatial resolution near synoptic scale. An analysis of data collected by the scanning bolometers aboard the *Nimbus*-3 satellite in 1969 revealed that Earth's planetary emitting temperature was approximately 254 K and it reflected approximately 29% of the sunlight incident upon it (Vonder Haar and Suomi 1969; Vonder Haar et al. 1972).

The *Nimbus-6* and *-7* satellites carried an ERB instrument, which consisted of a wide-field-of-view (WFOV) instrument that measured the radiation of Earth from limb to limb, and a scanning narrow-field-of-view (NFOV) instrument, which measured the radiation from Earth with higher spatial resolution (on the order of 10–100 km). With a footprint that is several thousand kilometers, the WFOV radiometer prohibits discriminating between clear sky and cloudy scenes. These instruments captured Earth's radiation by scanning at various viewing zenith angles, and fundamentally measured radiance, not a flux. Converting the radiance observation to a flux estimate required an angular distribution model (ADM).

Stephens et al. (1981) derived the ERB from a composite of 48 months of observations from Nimbus, concluding that the annual, global average emitted infrared flux is 234 W m^{-2}, the planetary albedo is 0.30, and the net flux is zero within measurement uncertainty. While the observed variance from year to year is large, the annual cycle of the observed globally averaged net flux is of a similar magnitude and phase to the annual cycle imposed by the influence of sun–Earth distance variations on solar radiation input into the atmosphere. A study of the geographical distribution of net flux annual variability reveals that generally more than 95% of this variability occurs as a result of the semiannual and annual cycles that may be forced by the regular variation in solar input throughout the year. The Nimbus measurements showed the influence of continents on the radiation budget and the zonal variation (Kubota and Imai 1986), while also confirming that the latitudinal variations of ERB components are larger than the longitudinal variations; the longitudinal variation is primarily determined by land–sea distribution.

a. Earth Radiation Budget Experiment

The Earth Radiation Budget Experiment (ERBE; Barkstrom 1984; Barkstrom and Smith 1986) was a follow-on and improvement to the Nimbus radiation measurements. ERBE was designed around three Earth-orbiting satellites: the NASA Earth Radiation Budget Satellite (ERBS) and two NOAA satellites. The ERBS was in a 57° inclined orbit while the ERBE scanners on board *NOAA-9* and *NOAA-10* were in a polar orbit; the precessing orbit of ERBS allowed measurements of the variations in the Earth radiation components during the day. Each satellite carried scanning (Kopia 1986) and nonscanning (Luther et al. 1986) radiometers, as well as solar radiometers. ADMs developed using the *Nimbus-7* NFOV instrument were then applied to the ERBE NFOV instruments (Suttles et al. 1988, 1989), which were able to measure the radiation budget of both clear areas and cloudy ones. ERBE observations became an important reference for general circulation models (GCMs; e.g., Ramanathan et al. 1989). Comparisons with ERBE demonstrated the need for improved characterization of cloud radiative properties in GCMs.

Clouds modulate the TOA, within-atmosphere, and surface radiation budgets. Clouds increase Earth's albedo and thus reduce the amount of solar radiation absorbed by Earth. Clouds decrease the loss of terrestrial infrared radiation. The ERBE program quantified the impact of clouds on the Earth radiative energy budget by inferring the cloud radiative effect (CRE). Defined as the difference between the measured reflected solar and/or emitted thermal radiation under all-sky and cloud-free conditions, CRE depends on the macrophysical and microphysical properties of the clouds. An important achievement of the ERBE was the determination that, globally, the shortwave CRE exceeds the instantaneous longwave CRE. A negative (positive) net CRE is often referred to as a cooling (warming). Other ERBE achievements included

- establishing an accurate, long-term dataset for studying climate (Loeb et al. 2009, 2016a);
- estimating CRE on a regional scale, enabling the measurement of cloud type, such as oceanic stratocumulus region and intertropical convergence zone (ITCZ);
- providing a radiation standard for validating and improving GCMs for climate sensitivity studies (Cess and Potter 1988; Ramanathan et al. 1989);
- deriving the first accurate diurnal variations of regional radiative parameters over the globe for climate studies (Harrison et al. 1988);
- measuring the longwave and shortwave radiative anomalies during the 1987 El Niño (Soden 1997); and
- measuring the shortwave and longwave anomalies due to the eruption of Mt. Pinatubo. The ERBE measured the increase in reflected sunlight and the decrease in emitted thermal energy to space, which lead to slight global cooling (Minnis et al. 1993).

In the decades that followed the ERBE program, improvements in calibration, increased spatial and temporal resolution, better modeling of surface and atmospheric properties, and the development of space-based active sensors have led to regular refinement of Earth's energy budget. For example, the incident solar flux density at the TOA, often termed the solar constant, is now known (Kopp and Lean 2011) to be 1360.8 ± 0.5 W m^{-2}, owing to very precise measurements from the Total Irradiance Monitor (TIM) that currently flies on the Solar Radiation and Climate Experiment (SORCE).

Defining the global energy budget requires a proper sampling of the ERB diurnal cycle. ERBE addressed this with three satellites that provide global sampling, but still have limited temporal sampling for nonpolar regions. Minnis and Harrison (1984a,b) addressed the diurnal sampling issue using narrow-broadband conversions applied to geostationary measurements. The Geostationary Earth Radiation Budget (GERB) instrument, which has flown on the European Meteosat Second Generation (MSG) geostationary satellites since 2003, addresses this issue more directly, but covers only part of the globe (Harries et al. 2005; Schmetz et al. 2002).

b. Clouds and the Earth's Radiant Energy System

During the past 17 years, the Clouds and the Earth's Radiant Energy System (CERES) experiment has routinely collected global ERB observations. The CERES calibration is a factor of 2 better than the ERBE scanners, with a field of view that is approximately a factor of 2 smaller. CERES instruments fly aboard the *Terra*, *Aqua*, *Suomi National Polar-Orbiting Partnership* (*SNPP*), and *Joint Polar Satellite System-1* (*JPSS-1*) sun-synchronous satellites (Wielicki et al. 1996; Loeb et al. 2018). Each CERES instrument is a three-channel scanning radiometer that uses precision thermistor bolometer detectors to observe radiation between 0.3 and 200 μm (total channel), 0.3 and 5 μm (shortwave channel), and 8 and 12 μm (window channel; Wielicki et al. 1996). The spatial resolution of the CERES instruments is 20 km (field of view at nadir) on *Terra* and *Aqua* and 24 km on *SNPP* and *JPSS-1*.

Comparisons of CERES measurements from *Terra* and *Aqua* suggest that the CERES record falls within the stability requirements outlined in Ohring et al. (2005), which recommends a long-term stability in TOA flux of 0.3 W m^{-2} $decade^{-1}$ for shortwave (SW) and 0.2 W m^{-2} $decade^{-1}$ for longwave (LW), at the 95% confidence level (Loeb et al. 2016b).

A unique feature of CERES is that it can be commanded from the ground to scan in different modes. In cross-track mode the scan is perpendicular to the ground track so that spatial sampling is optimized, providing global coverage daily. The CERES rotating azimuth plane (RAP) scan mode relies on the instrument's azimuthal axis drive system; when in RAP mode, the instrument scans in elevation as it rotates in azimuth, thereby acquiring radiances over a range of viewing zenith and relative azimuth angle combinations. The instrument can scan in the along-track mode to acquire multiangle measurements along the ground track and can also be placed in a programmable azimuth plane mode to acquire measurements for intercalibration with other instruments or to support field experiments.

A central objective of the CERES project is to continue a long-term global climate data record of Earth's radiation budget from the TOA down to the surface, along with the associated atmospheric and surface properties that influence it. A number of data sources are needed to accomplish this goal. In addition to the CERES instruments, there are broadband radiometers measuring the sun's output; high-resolution spectral imagers in both sun-synchronous and geostationary orbits; meteorological, aerosol, and ozone assimilation data; and snow/sea ice maps based on microwave radiometer data. While the TOA radiation budget is largely determined directly from accurate broadband CERES radiometer measurements, the surface radiation budget is derived indirectly through radiative transfer model calculations initialized using imager-based cloud and aerosol retrievals and meteorological assimilation data. To accurately capture changes in ERB from interannual to decadal time scales, the satellite instruments used to produce these data records must be radiometrically stable and the input data stream must be free of artificial discontinuities. Otherwise, distinguishing real climate system changes from artifacts in the data record is exceedingly difficult.

The CERES project has produced a unique suite of data products for studying ERB over a range of time–space scales. The CERES RAP data and imager-based retrievals have been used to develop new empirical ADMs for converting measured radiances to radiative fluxes (Loeb et al. 2003a, 2005; Su et al. 2015), leading to instantaneous footprint fluxes that are twice as accurate as ERBE (Loeb et al. 2003b). The new CERES ADMs were possible because of the availability of multiple years of coincident CERES RAP radiance data and imager retrievals, which provided information about the atmospheric properties within CERES footprints. The CERES science team developed cloud retrievals tailored for the ERB applications (Minnis et al. 2008, 2011a; Trepte et al. 2019) from collocated Moderate Resolution Imaging Spectroradiometer (MODIS; Salomonson et al. 1989) and Visible Infrared Imaging Radiometer Suite (VIIRS; Wolfe et al. 2013; Xiong et al. 2014) imagers.

To account for changes in the diurnal cycle between CERES observation times, imager data are supplemented with data from geostationary satellites (Doelling et al. 2013, 2016). At any given time, five geostationary imagers are measuring radiances over the visible and infrared spectrum between 60°S and 60°N. The CERES team cross calibrates all of these instruments together to provide accurate radiative fluxes and cloud properties averaged over $1° \times 1°$ latitude–longitude regions at hourly time steps. As a demonstration of the data volume used in today's scientific analysis, to date, the CERES team has processed data from 5 CERES instruments, 2 MODIS, 1 VIIRS, and 16 geostationary imagers, all integrated to obtain climate accuracy in radiative fluxes from the top to the bottom of the atmosphere.

The CERES program determines surface radiative fluxes using a radiative transfer model (Fu and Liou 1993; Fu et al. 1998; Kratz and Rose 1999; Kato et al. 1999, 2005). This model was initialized using cloud properties retrieved from additional satellite observations along with other ancillary input data to provide a long record of satellite-based surface radiative fluxes (Rutan et al. 2015; Kato et al. 2013, 2018). When compared with surface radiation measurements over 48 ocean buoy and 37 land sites, annual mean CERES surface radiative fluxes agree with the surface measurements to 6 W m^{-2} (1σ) for downward LW, 3 W m^{-2} for upward LW, 4 W m^{-2} for downward SW, and 3 W m^{-2} for upward SW (Kato et al. 2018).

The CERES data products have been used for a range of scientific studies. A summary of some of the results from these studies is listed below:

- CERES has been used to evaluate the impact of parameterization schemes in climate models (Park et al. 2014; Gettelman et al. 2015). Examples include parameterizations of bulk ice cloud properties for the Met Office Unified Model (Baran et al. 2014), a unified turbulence and cloud parameterization scheme for the atmospheric component of the Geophysical Fluid Dynamics Laboratory Climate Model, version 3 (AM3; Guo et al. 2014), a third-order turbulence closure in the multiscale modeling framework (Xu and Cheng 2013a,b), and new radiation (Herwehe et al. 2014) and cumulus (Lim et al. 2014) parameterization schemes in the Weather Research and Forecasting (WRF) Model.
- CERES-derived variations in global mean net TOA flux variations have been compared with variations in the rate of change in ocean heat content from Argo in situ data. The agreement falls within observational uncertainty (Loeb et al. 2012; Johnson et al. 2016).
- CERES data have been used to explain why the mean position of the ITCZ is in the Northern Hemisphere (Frierson et al. 2013; Marshall et al. 2014; Loeb et al. 2016a).
- CERES data combined with atmospheric reanalyzes were used to estimate ocean heat transports throughout the Atlantic. Results agree well with observational estimates (Trenberth and Fasullo 2017).
- CERES data have been used to study changes in TOA radiation budget in response to Arctic sea ice changes. For every 10^6 km^2 decrease in September sea ice extent, annual-mean absorbed solar radiation averaged over 75°–90°N increased by 2.5 W m^{-2}, or about 6 W m^{-2}, between 2000 and 2012. Changes in cloudiness appear to play a negligible role in observed Arctic darkening; as a result, the possibility of Arctic cloud albedo feedbacks, which mitigate future Arctic warming, is reduced (Hartmann and Ceppi 2014; Pistone et al. 2014).
- CERES data products have enabled new insights into climate feedback and climate sensitivity (Dessler 2010; Zhou et al. 2015; Brient and Schneider 2016).

c. Energy budget components

ERB components are fundamental climate parameters and are demanding measurements in terms of stability and absolute accuracy. Only continuous measurements of ERB from satellites can provide the required temporal and spatial resolution over the globe. Remarkably, however, early estimates of the planetary energy balance have stood the test of time. The CERES flying on the *Terra* and *Aqua* satellites confirm that Earth's albedo is 29.4% (±0.3%) and that the planet emits at an equivalent blackbody temperature of 255 K (±1 K; Wielicki et al. 1996; L'Ecuyer et al. 2015).

While modern satellites may have not dramatically altered estimates of the mean global balance at the TOA, new measurement capabilities have provided far deeper insights into Earth's energy balance and the factors that modulate it (L'Ecuyer 2017). Early satellites lacked coverage in the polar regions, providing insufficient information to constrain cloud properties. The geographic distribution of energy imbalances, the radiative heating and cooling within the atmosphere, and the heat exchanged between the atmosphere and surface drive weather and climate. Furthermore, ocean heat content changes over the last decade from the Argo array reveal that the excess energy trapped by the atmosphere as it adjusts to higher concentrations of greenhouse gases from anthropogenic emissions and associated climate feedbacks is just 0.75 ± 0.3 W m^{-2} (von Schuckmann et al. 2016); this value agrees well with independent estimates from satellite gravity and altimetry measurements (Llovel et al. 2014; Dieng et al. 2015). The early satellite record does not contain sufficient information to resolve the myriad changes in atmospheric composition and surface properties that could exert influences on this order of magnitude.

Attempts to derive regional atmospheric radiative convergence profiles (e.g., Cox and Griffith 1979; Ackerman and Cox 1981, 1987) used satellite observations to define the cloud amount and estimate their vertical distribution. Those observations were combined with the vertical and horizontal distributions of temperature, moisture, carbon dioxide, ozone, and aerosols in radiative transfer calculations to estimate the radiative divergence in the atmosphere. Surface fluxes were also calculated in this manner.

Quantifying the factors that influence Earth's energy balance has been a primary objective of new satellite observations in the twenty-first century. Modern satellites have furnished new estimates of clouds, aerosols, ocean surface temperature, snowpack and sea ice, vegetation, surface winds, and trace gases with sufficient accuracy to better diagnose their influences on Earth's energy budget. For example, the combination of radiative fluxes from CERES and coincident cloud properties from three cloud sensors: MODIS, *CloudSat*'s Cloud Profiling Radar (CPR), and the Cloud–Aerosol Lidar with Orthogonal Polarization (CALIOP) flying on board the *Cloud–Aerosol Lidar and Infrared Pathfinder Satellite Observations* (*CALIPSO*), have improved our understanding of the role clouds play in modulating radiative exchanges between Earth and space (King et al. 2003; Stephens et al. 2002; Winker et al. 2007, 2010). MODIS and microwave observations from the Advanced Microwave Scanning Radiometer for EOS (AMSR-E; Njoku et al. 2003) have furnished a more complete view of surface radiative characteristics (temperature, soil moisture, and ice cover). Temperature and humidity profiles are now retrieved with unprecedented resolution and accuracy from new hyperspectral sounders like the Atmospheric Infrared Sounder (AIRS; Susskind et al. 2011). Observations from active and passive microwave sensors have led to improved estimates of the global distribution of latent heat release in precipitation (e.g., Shige et al. 2007); these measurements have also enabled the development of algorithms designed to infer near-surface temperature and humidity required to infer evaporative and sensible heat fluxes from the surface through bulk formulas (e.g., Clayson and Bogdanoff 2013).

In the last 25 years, engineering advances have allowed observations at the same time from a coordinated constellation of multiple satellites flying in formation (Stephens et al. 2002; L'Ecuyer and Jiang 2010; Stephens et al. 2018). This breakthrough fostered the development of new integrated multisensor radiative flux datasets like *CloudSat*'s 2B-FLXHR-LIDAR product (L'Ecuyer et al. 2008) and the CERES–*CALIPSO*–*CloudSat*–MODIS (C3M) product (Kato et al. 2012). The explicit vertical structure and cloud base estimates from *CloudSat* and *CALIPSO* used in these datasets have brought about revisions to Earth's surface energy budget. For instance, Earth's surface is warmed by 165 ± 6 W m^{-2} of solar energy and an additional 345 ± 5 W m^{-2} of thermal energy emitted by the atmosphere to the surface (Stephens et al. 2012a,b). Collocated AMSR-E data reveal that these sources of surface heating are offset by 81 ± 4 W m^{-2} of latent heat transfer from the evaporation of water (primarily from the oceans), 25 ± 4 W m^{-2} of sensible heat transfer, and 399 ± 5 W m^{-2} of cooling by thermal emission from the surface (L'Ecuyer et al. 2015).

Simultaneous measurements of clouds, aerosols, precipitation, and their environment have also spurred new research into the specific factors that modulate Earth's energy budget. Chand et al. (2012) revealed that absorbing aerosols exert a warming influence on the climate when they reside above clouds, prompting others to revisit earlier estimates of aerosol direct radiative forcing of climate. Building on these regional findings, Matus et al. (2015) utilized global aerosol and cloud cover information from *CALIPSO* and *CloudSat* and radiative transfer models to estimate the net global aerosol direct radiative effect under all sky conditions to be 2 W m^{-2}, filling in the important warming contributions of cloudy scenes that were often omitted from prior estimates. Building on pioneering work in the 1980s and 1990s, multisensor A-Train observations have also revealed that clouds approximately double the fraction of sunlight reflected to space from about 15% in clear skies to the observed 29.4% (L'Ecuyer et al. 2015; Matus and L'Ecuyer 2017). This measurement represents a reduction of 49 W m^{-2} in incoming solar energy. Similarly, clouds reduce the amount of energy emitted by Earth to space by about 28 W m^{-2} (equivalent to an 8°C change in Earth's emitting temperature relative to a cloudless planet). Thus, on aggregate, clouds cool Earth by approximately 21 ± 4 W m^{-2} relative to the cloud-free atmosphere (Matus and L'Ecuyer 2017).

Figure 4-2 presents a current composite view of annually averaged cloud fraction and its influence on several components of ERB from today's satellites. These maps capture several of the advances enabled by combining the modern passive instruments and new active sensors alluded to above. The estimates of CRE at the surface require cloud boundary information, observations that *CloudSat* and *CALIPSO* provide. The A-Train's multisensor perspectives have allowed the effects of mixed-phase and multilayered cloud systems to be explicitly represented in radiation budget estimates. Multilayered clouds have been found to account for nearly 42% of global cloud cover and 44% and 49% of shortwave and longwave cloud forcing, respectively (Hang et al. 2018, manuscript submitted to *J. Climate*). Oreopoulos et al. (2017) quantified CRE for cloud height and vertical/multilayer extent classifications; they found that all but two classifications—the high single layer and contiguous high/midtroposphere layer categories—had a negative (cooling) net TOA CRE. Mixed-phase clouds have been shown to significantly enhance downwelling longwave radiation on the Greenland Ice Sheet, dramatically increasing melt rates by suppressing nighttime refreezing processes (Van Tricht et al. 2016). These new estimates of TOA and surface cloud forcing have, in turn, furnished accurate estimates of cloud impacts on atmospheric heating to date. The net influence of clouds on atmospheric heating (lower-right panel of Fig. 4-2) demonstrates that clouds enhance large-scale atmospheric meridional circulations by heating the equatorial regions and cooling the poles.

Current satellite missions measured the coupling between components of the planet's hydrological and

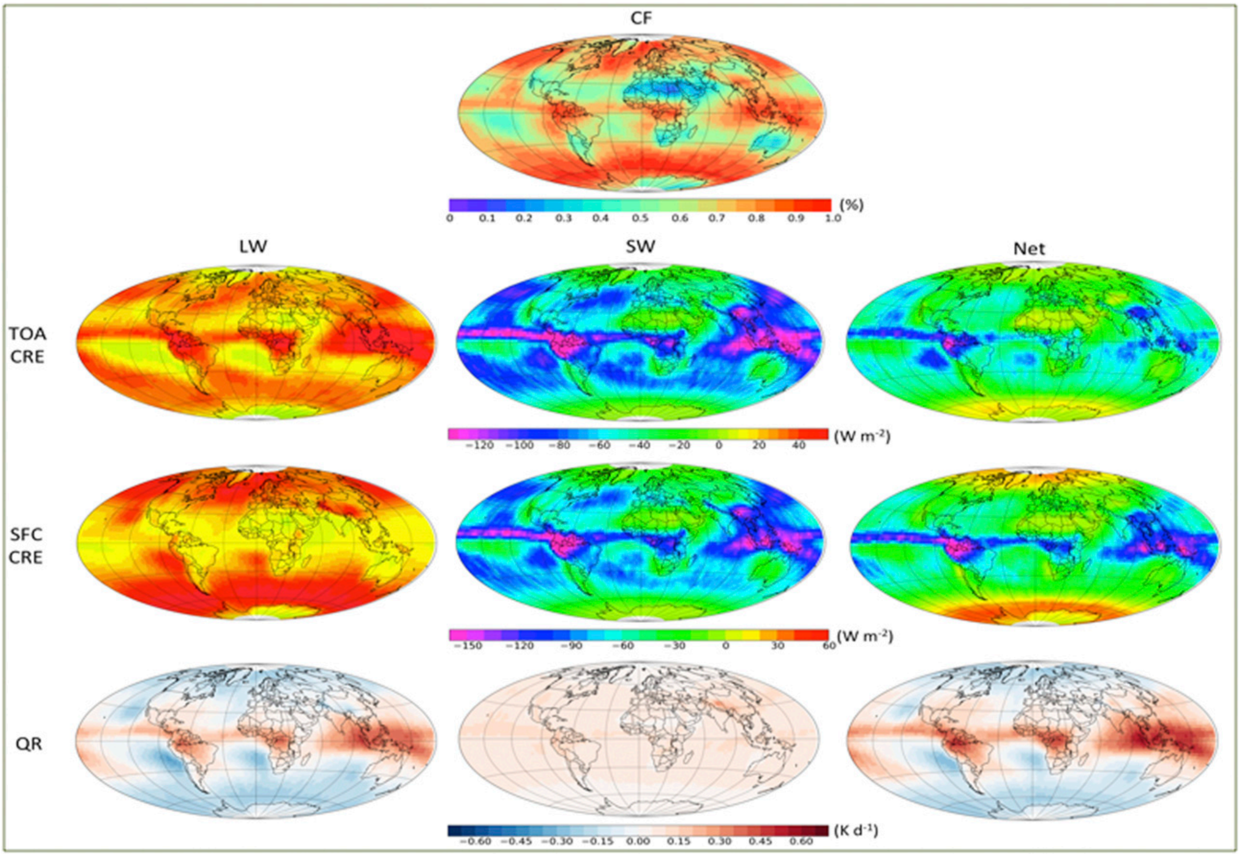

FIG. 4-2. Annual mean cloud occurrence (cloud fraction) from (top) a combination of *CloudSat*, *CALIPSO*, and MODIS observations and (first row) cloud influence on top of atmosphere, (second row) surface, and (bottom row) atmospheric radiative balance. The cloud influence on atmospheric radiation has been cast in terms of radiative heating in K day^{-1}.

energy cycles. Specific satellite missions have been critical in characterizing the hydrological cycle, with each new mission advancing our knowledge of how water circulates through and affects the atmosphere.

3. Hydrological cycle

a. Clouds

From the earliest days of forecasting, clouds were viewed as defining the current state of the atmosphere. Folk sayings such as "ring around the moon" were common forecast rules of thumb long before the instrument era. Later, in the early days of the space race, scientists recognized that satellite observations could provide a bird's eye view of cloud patterns across the globe, providing data and clarity for what was being observed from the ground. The first Television Infrared Observation Satellite (*TIROS-1*) launched on 1 April 1960 made the first satellite observations of clouds. Ten experimental TIROS satellites were launched between 1960 and 1965, mostly to support weather forecasting by identifying cloud systems. To understand the hydrologic cycle, measurements of the following cloud properties are needed: cloud amount, cloud top and base height, water phase, and microphysical properties and their precipitation state.

b. Cloud amount

In addition to applications in satellite meteorology and climatology, cloud detection is needed for surface and clear-sky atmospheric studies to avoid processing pixels that might be cloud contaminated. Because clouds are generally characterized by higher reflectance and lower temperature than the underlying Earth surface, simple visible and infrared window threshold approaches offer considerable skill in cloud detection (Arking 1964; Saunders and Kriebel 1988; Derrien et al. 1993; Chen et al. 2002). Early methods used constant thresholds, later replaced with thresholds by scene type or ones that varied temporally (e.g., Ackerman et al. 1998; Minnis and Harrison 1984a,b). An alternate technique locates clusters of pixels on a two-dimensional histogram (Desbois et al. 1982; Phulpin et al. 1983). Cluster centers are identified in the histogram, and then classified as clear or a particular type of cloud. A spatial coherence test (e.g., Coakley and Bretherton 1986) attempted to account for pixels that had partial cloud cover within the field of view.

The International Satellite Cloud Climatology Project (ISCCP) began in 1983, with a focus on using satellite observations to derive a global climatology of cloud properties that characterize the distribution and variation of clouds and their effects on the radiation budget. The ISCCP data products have also been used to assess climate model simulations of global cloud patterns. Cloud detection schemes for ISCCP were developed using visible and infrared window radiances. The cloud-masking algorithm described by Rossow (1989), Rossow et al. (1989), and Rossow and Garder (1993) utilizes the narrowband visible (0.6 μm) and the infrared window (11 μm) channels on geostationary platforms. This algorithm is based on the premise that 1) only two types of conditions, cloudy and clear, explain the observed visible and infrared radiances and 2) the ranges of radiances and their variability associated with these two conditions do not overlap (Rossow and Garder 1993). As a result, the algorithm is based upon thresholds; a pixel is classified as cloudy only if at least one radiance value is distinct from the inferred clear value by an amount larger than the uncertainty in that clear threshold value.

The Advanced Very High Resolution Radiometer (AVHRR) on the NOAA Polar Operational Environmental Satellites (POES) began making observations in 1978 and has provided a data record with consistent spectral and spatial characteristics ever since. The AVHRR Processing Scheme Over Clouds, Land and Ocean (APOLLO) cloud detection algorithm used the five visible and infrared channels of the AVHRR (Saunders and Kriebel 1988; Kriebel et al. 1989). The scheme uses threshold tests applied to the AVHRR channels at full spatial resolution, nominally 1.1 km at nadir. One of the first regional AVHRR cloud climatologies was the Swedish Meteorological and Hydrological Institute (SMHI) Cloud Analysis Model Using Digital AVHRR Data (SCANDIA) dataset, implemented in 1988 (Karlsson 1989). SCANDIA covered the Scandinavian region with a spatial resolution of 4 km. The Pathfinder Atmospheres (PATMOS) project (Stowe et al. 2002; Jacobowitz et al. 2003) data provided ascending and descending global views with a spatial resolution of 1° (110 km) and included only the AVHRR sensors launched into the afternoon orbits (*NOAA-7*, *-9*, *-11*, *-14*). A pioneering project with long-lasting impacts, PATMOS offered total cloud amount as its sole product. The PATMOS Clouds from AVHRR (CLAVR) uses a series of spectral and spatial variability tests to detect clouds. The phase I CLAVR algorithm used all five channels of AVHRR to derive a global cloud mask (Stowe et al. 1991). It examines multispectral information, channel differences, and spatial differences and then employs a series of sequential decision-tree tests. Cloud-free, mixed (subpixel cloud), and cloudy regions are identified for 2° × 2° global area coverage (GAC) pixel (4-km resolution) arrays. Subsequent versions of CLAVR use dynamic thresholds predicted from the angular pattern observed from the clear-sky radiance statistics of the previous 9-day repeat cycle of the NOAA satellite for a mapped 1° equal-area grid cell (Stowe et al. 1991). Developed in the 1990s, these cloud algorithms remained in use for climatology studies for a decade.

The Pathfinder Atmospheres Extended (PATMOS-x) project was launched in 2004 (Heidinger et al. 2014) as an extension of PATMOS. It included all AVHRR sensors, including those launched into morning and midmorning orbits by NOAA and the European Organisation for the Exploitation of Meteorological Satellites (EUMETSAT). In addition, it expanded its list of products to include cloud type, height, optical thickness, water path, particle size, albedo, and transmission, and included the calibrated AVHRR observations. PATMOS-x also generated its global fields at a spatial resolution of 0.1°, accomplished via sampling rather than averaging. As a result, PATMOS-x could be used as a basis for other derived cloud records (e.g., Zhao et al. 2016). For example, the PATMOS-x dataset has been applied to research in aerosol–cloud interactions (Rausch et al. 2010; Bennartz et al. 2011), climatic impacts of dust transport (Evan et al. 2009), global cloud studies (Norris and Evan 2015; Marvel et al. 2015), and regional cloud studies (Ackerman et al. 2013; Rausch et al. 2010). Several other AVHRR cloud datasets have appeared in recent years, including those from the EUMETSAT Climate Monitoring Satellite Application Facility (CM-SAF) and the European Space Agency's (ESA) Cloud Climate Initiative (CCI). These activities ensure that the AVHRR data record will remain relevant for many years to come.

Challenges remain in creating climate data records (CDRs) from instruments flown on different satellites. For an AVHRR cloud climate dataset, the main challenge is the systematic change in the observation times due to orbital drift for all of the NOAA satellites. The PATMOS-x team and other groups have actively explored techniques to account for this drift (Foster and Heidinger 2013). PATMOS-x is also expanding its scope to include the NASA EOS MODIS imagers and the NOAA geostationary imagers from 1995 to the present.

Developing a consistent PATMOS-x product database using these other sensors with constant or diurnally resolved observation times will assist scientists in more fully accounting for these orbital drift issues in the AVHRR record.

MODIS, a keystone instrument of the EOS program, provides global observations of Earth's land, oceans, and atmosphere in 36 spectral channels from 0.4 to 14.5 μm, and at nadir spatial resolutions from 250 to 1000 m. A variety of cloud properties have been retrieved from MODIS through continuous observations from the *Terra* and *Aqua* satellite platforms since 2000 and 2002, respectively. Globally, the cloud fraction derived by the MODIS cloud mask (Ackerman et al. 1998; Frey et al. 2008; Ackerman et al. 2008) is approximately 67%, with somewhat more clouds over land during the afternoon (MODIS *Aqua* relative to *Terra*) and fewer clouds over ocean in the afternoon, with very little difference in global cloud cover between the two satellites (King et al. 2013). Overall, the cloud fraction over land is approximately 55%, with a distinctive seasonal cycle, whereas ocean cloudiness is around 72%, with a small seasonal variation.

The launch of *CALIPSO* and *CloudSat* in 2006 led to a new global capability to observe the vertical distribution of clouds, aerosols, and precipitation. The *CALIPSO* mission carried three instruments (Winker et al. 2007): the two-wavelength polarization-sensitive CALIOP, the three-wavelength Imaging Infrared Radiometer (IIR), and the visible Wide Field Camera (WFC). CALIOP is an elastic backscatter lidar that transmits linearly polarized laser light at 532 and 1064 nm and measures range-resolved backscatter intensities at both wavelengths. The *CloudSat* mission includes the CPR and a 94-GHz nadir-looking radar. These active measurement instruments provide information on vertical cloud structure, allowing insights into the processes that control clouds, aerosols, and precipitation.

CALIOP has proved fundamental in evaluating cloud amount products, especially for MODIS *Aqua*, where both instruments are part of the A-Train constellation (e.g., Holz et al. 2008). Mace and Zhang (2014) found that merged *CloudSat*–CALIOP cloud occurrence statistics at 5-km resolution matched well with MODIS *Aqua* cloud mask for daytime global oceans, though MODIS is biased low over the poles due to a lack of visible and thermal contrast with the surface.

The Global Energy and Water Cycle Experiment (GEWEX) Cloud Assessment was initiated by the GEWEX Radiation Panel in 2005 to compare available, global, long-term cloud data products with the ISCCP. That assessment was reported in Stubenrauch et al. (2013) and includes a summary of average satellite cloud properties and their variability. The global total cloud amount from the different satellite measurements ranged from 0.56 to 0.74 as a result of different instrument sensitivity and retrieval methodologies. Most of the 12 comparison datasets found that the ocean's fractional coverage is about 0.10–0.15 more than land. Similarly, the State of the Climate report published yearly in the *Bulletin of the American Meteorological Society* routinely compares the global annual anomaly of cloud amount from different cloud datasets (e.g., Foster et al. 2017). The cloud anomalies are smaller than the observed seasonal and diurnal variability within each cloud data record. For example, CALIOP has the highest global cloud fraction, as a lidar is more sensitive to optical thickness than passive methods. The near-nadir viewing of CALIOP limits the global sampling, which can be overcome through spatial and temporal averaging.

Cloud amount by itself is not sufficient for understanding water or energy processes. Beyond detection, it is important to infer macroproperties (cloud-top altitude, pressure, temperature) and microphysical (thermodynamic phase, particle size, water content) and radiative properties (optical thickness, effective particle size, ice particle shape). These are discussed in the following subsections.

c. Cloud altitude

Scientists use multispectral observations from satellites to infer cloud-top heights. For example, the CO_2 slicing technique developed in the 1970s uses narrowband radiances measured at wavelengths between 13.3 and 14.2 μm to retrieve cloud-top pressure and effective cloud amount, which is the product of cloud emissivity and cloud fraction (Chahine 1974; Smith et al. 1974). The CO_2 slicing method has been used to distinguish transmissive clouds from opaque clouds and clear-sky using High-Resolution Infrared Radiation Sounder (HIRS) multispectral observations (Wylie et al. 1994). The technique has also been applied operationally to 15-μm data from the Geostationary Operational Environmental Satellite (GOES) Visible Infrared Spin-Scan Radiometer (VISSR) Atmospheric Sounder (VAS; Wylie and Menzel 1989) and the GOES Sounder, as well as applied to the height assignment of atmospheric motion vectors (Menzel et al. 1983). Using this method, scientists could investigate diurnal signatures of cloud-top altitudes. Frey et al. (1996) developed a real-time, global algorithm for detecting clouds using collocated AVHRR and HIRS/2 observations. Taking advantage of hyperspectral measurements, Holz et al. (2006) developed a CO_2 sorting–slicing method that uses hyperspectral IR observations to select the optimal channel pairs for CO_2 slicing. In addition, scientists have developed window infrared methods, applicable to a wider variety of sensors, for multi-instrument/platform CERES processing (Minnis et al. 2011a,b).

As MODIS has the key CO_2 slicing channels used in the HIRS studies, it can provide a higher-spatial-resolution (1 km) product relative to HIRS (20 km) as well as a tightly constrained mean local time sun-synchronous orbit (~1 min typically) of the *Terra* and *Aqua* missions. Cloud-top pressures of ice clouds from MODIS *Aqua* show somewhat higher clouds than corresponding MODIS *Terra* (cloud-top pressures lower by 100 hPa) over land due to afternoon deep convection (King et al. 2013). Comparisons with CALIOP indicate that radiative heights from MODIS are typically 1.5 km lower in altitude, though varying widely depending on cloud type (Holz et al. 2008; Minnis et al. 2011b).

Cloud heights can be derived from absorbing gases other than CO_2. Satellite products based on the O_2 A-band absorption complex at about 763 nm include algorithms applied to the Global Ozone Monitoring Experiment (GOME; Koelemeijer et al. 2001), Scanning Imaging Absorption Spectrometer for Atmospheric Cartography (SCIAMACHY; Kokhanovsky et al. 2005), Medium Resolution Imaging Spectrometer (MERIS; Fischer et al. 1997), and the two Polarization and Directionality of the Earth Reflectances (POLDER; Deschamps et al. 1994) instruments (Vanbauce et al. 1998; Ferlay et al. 2010). POLDER also includes a cloud height algorithm using pressure height inferred from Rayleigh polarization (Buriez et al. 1997).

Stereoscopic, or stereo, methods have also been used to determine cloud-top altitude. In this case, cloud height determination depends only on geometry, assuming the cloud is not moving. Minzner et al. (1976) and Hasler (1981) describe how observations from two different geostationary satellites can be used to estimate cloud height. To obtain global measurements, the Multiangle Imaging Spectroradiometer (MISR) was used to gather cloud-top data using stereo methods. This instrument employs nine discrete cameras pointed at fixed angles, one viewing the nadir (vertically downward) direction and four each viewing the forward and aftward directions along the spacecraft ground track—specifically imaging Earth at 26.1°, 45.6°, 60.0°, and 70.5°. Its data are carefully calibrated to provide accurate measures of the brightness, contrast, and color of reflected sunlight. By looking at the change in reflection at different view angles, different types of atmospheric particles (aerosols), cloud forms, and land surface covers can be distinguished. Combined with stereoscopic techniques, scientists use this information to construct 3D models and estimate the total amount of sunlight reflected by Earth's diverse environments. An analysis of 15 years of MISR clouds worldwide showed no definitive trend in cloud height (Davies et al. 2017). However, cloud heights do vary from year to year in connection with various weather and climate phenomena. During the 2008 La Niña, MISR showed a lowering of global clouds on average by 40 m while El Niño events increased their altitudes.

Beyond cloud-top retrievals, *CloudSat* and *CALIPSO* have revolutionized our knowledge of the vertical distribution of clouds (Mace et al. 2009; Deng et al. 2010; Mace and Zhang 2014). The CALIOP–CPR combination can identify multilayered cloud systems, an important capability as 60% of the time clouds are categorized as multilayered (Stephens et al. 2008). Using CALIOP and *CloudSat* data in a study of zonal cloud phase, Bodas-Salcedo et al. (2016) demonstrated that liquid clouds poleward of 48°S are composed of primarily supercooled water droplets. This observation pointed to model biases that do not correctly simulate supercooled water in the cold sector of baroclinic weather systems. The CALIOP *CloudSat* combination along with modeling efforts demonstrated that clouds over Greenland enhanced the meltwater runoff relative to clear skies (Van Tricht et al. 2016). *CloudSat* CPR measurements also revealed that oceanic clouds had a higher fraction of drizzle-size rain particles than their land-based counterparts, the opposite of what was expected. The larger concentrations of aerosols over land produce clouds composed of smaller drops, which was expected to lead to more drizzle over land.

The relative agreement of these various passive height products depends on the effective weighting function in the cloud, which in turn is highly dependent on the measurement approach and geometry. The GEWEX Radiation Panel compared cloud-top height datasets from the algorithms of ISCCP, PATMOSx, HIRS, MODIS (standard products and those developed for CERES processing), MISR, POLDER, and *CALIPSO* (Stubenrauch et al. 2013). While high-level cloud statistics varied the most between the datasets due to each instrument's inherent sensitivity to thin cirrus, relative geographical and seasonal variations in the cloud properties agreed well. Instrument simulators designed for climate model evaluation (e.g., Bodas-Salcedo et al. 2011; Pincus et al. 2012), which are increasingly available for the satellite datasets, allow scientists to use the products more directly to evaluate model performance.

d. Cloud optical and microphysical properties

Passive retrievals of cloud optical and microphysical properties begin by determining thermodynamic phase.

Passive approaches include spectral signatures harking back to Pilewskie and Twomey (1987), along with window infrared techniques (Strabala et al. 1994; Baum et al. 2012), multiangle polarimetric discrimination based on enhanced polarization in the liquid droplet cloud bow (Goloub et al. 2000; Riedi et al. 2010), and/or angular information resolving other portions of the particle scattering phase function (e.g., Labonnote et al. 2001; van Diedenhoven et al. 2012). Using CALIOP-observed depolarized backscatter, scientists can directly retrieve the phase of water in clouds near the cloud top (Hu et al. 2009), which has been used as a reference standard for passive imager algorithms (e.g., Marchant et al. 2016). During the first year the *CALIPSO* transmitter was pointed near-nadir, generating more specular reflections from horizontally oriented ice crystals than expected. Ross et al. (2017) found that the oriented signature is strongly correlated with surface precipitation from collocated *CloudSat* measurements, with 64% of CALIOP-oriented ice crystal cases precipitating compared to 40% for nonoriented cases. To mitigate this specular return, the viewing angle of CALIOP was changed from 0.3° to 3° in November 2007.

Optical property retrievals (optical thickness, effective particle size) began with airborne studies using various combinations of visible, near-infrared, shortwave/midwave-infrared solar reflectance measurements (Twomey and Cocks 1989; Nakajima and King 1990; Rawlins and Foot 1990). The first quantitative satellite retrievals were applied to AVHRR data (Arking and Childs 1985; Han et al. 1994; Platnick and Twomey 1994). With the availability of imagers such as MODIS, and its improved radiometric stability and orbital mean local time crossing control, passive optical retrievals entered a new era [i.e., MODIS standard products (King et al. 2003; Platnick et al. 2003, 2017) and products developed for CERES processing (Minnis et al. 2011a,b)].

Cloud droplet effective radius r_{eff} is an important parameter for climate as it represents the relationship between the cloud liquid water content and its albedo. For given liquid water content, smaller droplets lead to larger cloud albedo. MODIS Collection 6 standard products (Platnick et al. 2017) give liquid water clouds effective particle radii that are significantly larger over ocean than land (>5 μm or more), depending on location/season and the spectral band combination used in the retrieval (also see King et al. 2013), with the largest variability occurring over the ocean. Aggregating over ±60° latitude gives ocean effective sizes about 2 μm larger than land for most band combinations. The largest marine water cloud particle sizes are associated with broken clouds scenes; this may indicate retrieval artifacts associated with the breakdown of the 1D radiative transfer used in the retrieval algorithm and/or covariance of broken clouds with the existence of drizzle and other meteorological changes (Zhang and Platnick 2011; Cho et al. 2015). Somewhat larger ice cloud effective particle sizes are also found over the ocean relative to land, about 2–3 μm larger when aggregated over ±60° (Wood et al. 2018; Minnis et al. 2011b).

The directional signature of the polarized reflectance by a liquid water cloud is also employed to retrieve cloud droplet effective radius from space. The POLDER measurements showed that, on average, droplets are 2–3 μm smaller over land than over the oceans (Bréon and Colzy 2000). Smaller droplets are also found over highly polluted regions and in areas affected by smoke from biomass burning activity (Painemal et al. 2014).

Establishing a reference cloud optical property dataset with well-understood uncertainties for satellite intercomparisons remains challenging. The MODIS standard products contain uncertainty datasets based on a limited number of quantifiable error sources. CALIOP lidar cirrus retrievals have been used to help guide MODIS ice particle radiative models (Holz et al. 2016). Ground-based retrieval intercomparisons with MODIS products include those of Dong et al. (2008) and Mace et al. (2005) for liquid and ice clouds, respectively, as well as Dong et al. (2016) for the Arctic and Xi et al. (2014) and Z. Zhang et al. (2017) for ocean. Empirical (e.g., Werner et al. 2016; Painemal et al. 2013) and theoretical studies (e.g., Zhang and Platnick 2011; Fauchez et al. 2015; Miller et al. 2016) of cloud heterogeneity impacts are helping the community better understand the uncertainties in passive optical cloud property retrievals.

e. Cloud water path

Cloud water path is a measure of the total water mass (liquid and/or ice) contained per unit area in all cloud layers in a vertical column of atmosphere. Cloud water path and content (mass per volume) is highly variable and depends on cloud type. The longest record of cloud liquid water path (LWP) over the ocean comes from passive microwave estimates using measurements around 19 and 37 GHz. The absorption at these frequencies is related to the total amount of liquid water along the path, accounting for absorption by oxygen and water vapor, and ocean surface temperature and roughness (Wentz 1997; Greenwald et al. 1993; Liu and Curry 1993). These approaches are best over oceans because of the relatively uniform surface emissivity. LWP in precipitating and nonprecipitating clouds over oceans have been estimated with the Special Sensor Microwave Imager (SSM/I), a passive microwave radiometer with dual-polarized channels at 19.35, 37, and 85.5, GHz and a vertically polarized channel at 22.235

GHz. The SSM/I has been carried on board Defense Meteorological Satellite Program (DMSP) satellites since 1987.

Satellite observations have demonstrated that cloud liquid water exhibits a strong diurnal variation over many ocean regions. The largest variations are over the tropical western Pacific and northwestern Pacific and are attributed to the diurnal variation in raining clouds. The variation over the west coasts of major continents is also large and is associated with nonraining stratus clouds (Painemal et al. 2012). O'Dell et al. (2008) derived an 18-yr time series (1988–2005) of cloud LWP over oceans by combining observations from the SSM/I, the Tropical Rainfall Measuring Mission (TRMM) Microwave Imager (TMI), and the AMSR-E. Elsaesser et al. (2017) updated the time period to include 1988–2016. Potential systematic errors in the LWP climatology are on the order of 15%–30% or higher, which hampers the usefulness of microwave-based climatologies of both cloud liquid water and especially rain rate.

Cloud ice water path (IWP) spans several orders of magnitude (Dowling and Radke 1990), and the variable densities of the constituent ice particles have been major obstacles to improved measurements of IWP. Current operational microwave sensors are sensitive only to relatively thick ice clouds (e.g., Hong et al. 2005) because of the weak interaction between millimeter-wave radiation and cloud ice particles. The interaction is significantly stronger for submillimeter wave radiation (frequencies ranging from 183 to 916 GHz). Submillimeter-wavelength radiometry (Evans et al. 1999) complements traditional infrared measurements by providing sensitivity to a range of IWP spanning three orders of magnitude. The potential of millimeter and submillimeter satellite observations for cloud ice retrieval has been demonstrated with data from the limb-sounding Microwave Limb Sounder (MLS) on NASA's Upper Atmosphere Research Satellite (UARS) and NASA's EOS *Aura* (Li et al. 2005). Radar observations at 95 GHz, such as from *CloudSat*, cover a larger dynamic range in IWP from approximately five to several thousand grams per square meter. However, 95-GHz radar data alone do not give very accurate estimates of ice water content and IWP, since the radar reflectivity depends on the particle size distribution, which varies from cloud to cloud. The first non-limb-viewing spaceborne submillimeter measurement came from the NASA IceCube CubeSat (single channel at 883 GHz) launched in 2017; the Ice Cloud Imager (ICI), a multichannel conical scanner up to 664 GHz, is planned to launch on the EUMETSAT MetOp-SG-B satellites.

Passive imagers have also been used to infer cloud water path. For solar reflectance methods, cloud water path is proportional to the product of optical thickness and effective particle radius (with a factor of about 2/3 for either liquid or ice clouds assuming effective radius is constant in the vertical column). The effect of vertical heterogeneity in a liquid water cloud is sometimes approximated by a factor 5/6 assuming an adiabatic increase in particle size with height, a constant droplet concentration with height, and that the satellite-retrieved effective size is exactly at cloud top (e.g., Wood and Hartmann 2006). LWP from MODIS *Aqua* (Platnick et al. 2003) and the AMSR-E microwave imager compare well for marine stratocumulus regimes using the adiabatic assumption (Bennartz 2007; Greenwald 2009; Horváth and Davies 2007). The agreement is best for overcast scenes on the microwave imager scale. When comparing MODIS operational cloud water path retrievals with TMI (~25-km effective retrieval area; Wentz 1997), lower cloud fraction scenes show a systematic LWP bias with TMI retrievals higher than those from MODIS (Horváth and Gentemann 2007). Painemal et al. (2016) showed that space-based microwave LWP retrievals tend to overestimate LWP in low cloud fraction and moist conditions.

As was the case for microwave methods, IWP retrievals are challenging for passive imager applications due to larger inherent uncertainties in cloud optical thickness and effective particle radius retrievals related to ice particle habit sensitivities, where sensitivities are more problematic for reflectance-based retrievals (e.g., Yang et al. 2007; Holz et al. 2016) than infrared retrievals (Heidinger et al. 2015; Wang et al. 2016). Both reflectance and infrared retrievals can further be affected by complicated ice cloud vertical size and habit heterogeneities (e.g., Zhang and Platnick 2011; Fauchez et al. 2015). However, retrievals of IWP for thin ice clouds is promising from lidar (e.g., CALIOP). Establishing a reference IWP global dataset with well-understood uncertainties for global intercomparisons remains challenging.

f. Precipitation

Precipitation is a crucial component of the hydrological cycle. With its large temporal and spatial variations, the amount of rainfall is important in weather forecasting, predicting flash flooding, and energetics in terms of latent heat release. Traditionally, rainfall measurements are made with rain gauges and observed at a particular location. Radar observations provide better areal averages, but both approaches suffer from the lack of global coverage.

Early applications of satellite observations attempted to determine precipitation, in particular 24-h rainfall, by using cloud amount and cloud type derived from polar-orbiting imagery. A variety of visible/infrared rain retrieval algorithms (Scofield and Oliver 1977; Griffith et al. 1978; Adler and Negri 1988) offer different skills depending on rainfall type. Geostationary platforms offer temporal measurements that can be used to determine the storm life cycle, but their solar and infrared measurements do not directly observe precipitation, which limits their application. In addition, these methods have random and bias errors associated with the indirect nature of the relationship between the infrared radiances, which primarily originate near the cloud top, and the precipitation that emerges from the bottom of the cloud system. Generally speaking, the methodologies produced relatively good results for tropical oceanic precipitation and poorer results for cold season extratropical precipitation over land (Xie and Arkin 1995; Janowiak et al. 1995).

Scientists have developed algorithms to derive precipitation information from satellite observations in the IR and microwave and applied them globally (e.g., Barrett and Martin 1981; Arkin and Ardanuy 1989). The Global Precipitation Climatology Project (GPCP) was established in 1986 in part to better understand precipitation patterns as they vary regionally, seasonally, and interannually (Xie and Arkin 1997). The GPCP used rain gauge data and satellite imagery (infrared and microwave) to fill the gaps over the oceans and sparsely populated areas. These early precipitation datasets were critical in describing and studying the annual and interannual variability in large-scale precipitation over the globe.

In the microwave region, absorption by cloud drops is small and the transmittance of the typical nonprecipitation cloud is greater than 0.9. Scattering by cloud droplets is negligibly small while raindrop size particles interact strongly with microwave radiation. As a result, clouds are nearly transparent in the microwave unless they are raining, forming the basis for microwave detection of precipitation. Rainfall estimates have been made with microwave measurements from the SSM/I on the DMSP, first launched in 1978. At sufficiently low frequencies ($<$20 GHz), ice particle scattering is negligible and the variations in the observed brightness temperature result from variations in the optical depth of raindrops, which is approximately proportional to the integrated total rainwater amount. As the total rainwater is closely related to the surface rain, the low-frequency microwave brightness temperature provides a relatively direct representation of rainfall rate. This approach works over ocean, where surface temperature and emissivity generally do not vary dramatically. The relation between brightness temperature and rainfall rate is retrieved by matching the satellite observations with radiative transfer model calculations that specify the atmospheric temperature and humidity profiles, cloud liquid water content, rain layer thickness, and size distribution of raindrops. However, this methodology cannot be applied over land because of the variable and high surface emissivity.

Frequencies higher than 80 GHz are primarily used for scattering-based precipitation algorithms. For high-frequency microwaves ($>$80 GHz), scattering by ice particles aloft is the dominant signature in rain cloud observations. The scattering signature is physically less directly related to precipitation than the emission signature because it indicates the ice amount above the freezing level.

g. *Tropical Rainfall Measuring Mission*

Global precipitation measurements were enhanced with the TRMM (Kummerow et al. 2000) launched in late 1997 and ending in 2015. A joint mission between NASA and the Japan Aerospace Exploration Agency (JAXA), it was the first-time use of both active and passive microwave instruments to estimate precipitation. The instrumentation and precessing, low-inclination orbit (35°) made TRMM the world's foremost mission for the study of precipitation and associated storms and climate processes in the tropics. The TRMM Precipitation Radar (PR) provided the most direct method of observing precipitation and its vertical distribution, thus enabling a 3D view of precipitation. The TRMM PR is a 128-element active phased array operating at 13.8 GHz. It has a swath width of 215 km with a cross-range spatial resolution of about 4.3 km with a range resolution of 250 m. The PR was designed to achieve a minimum detectable rain rate of 0.7 mm h^{-1}.

Designed as an experimental mission focusing on tropical rainfall climatology, TRMM evolved into the primary satellite in a system of research and operational satellites used for analyzing precipitation characteristics on time scales from 3 h to interannual. TRMM represented a substantial advancement in precipitation measurement from space with its unique sensor suite, including the PR, a microwave imager (TMI), a Visible and Infrared Scanner (VIRS), a lightning imaging sensor (LIS), and a CERES scanning radiometer (Kummerow et al. 1998). This combination of sensors enabled the TRMM observations to produce the best instantaneous rain estimates at the time; those estimates were then used to calibrate or adjust rain estimates from other satellites to provide analyses at a higher temporal resolution than would be available from a single satellite. The TRMM Multisatellite Precipitation Analysis (TMPA; Huffman et al. 2007) provided calibrated precipitation estimates from multiple satellites, as well as

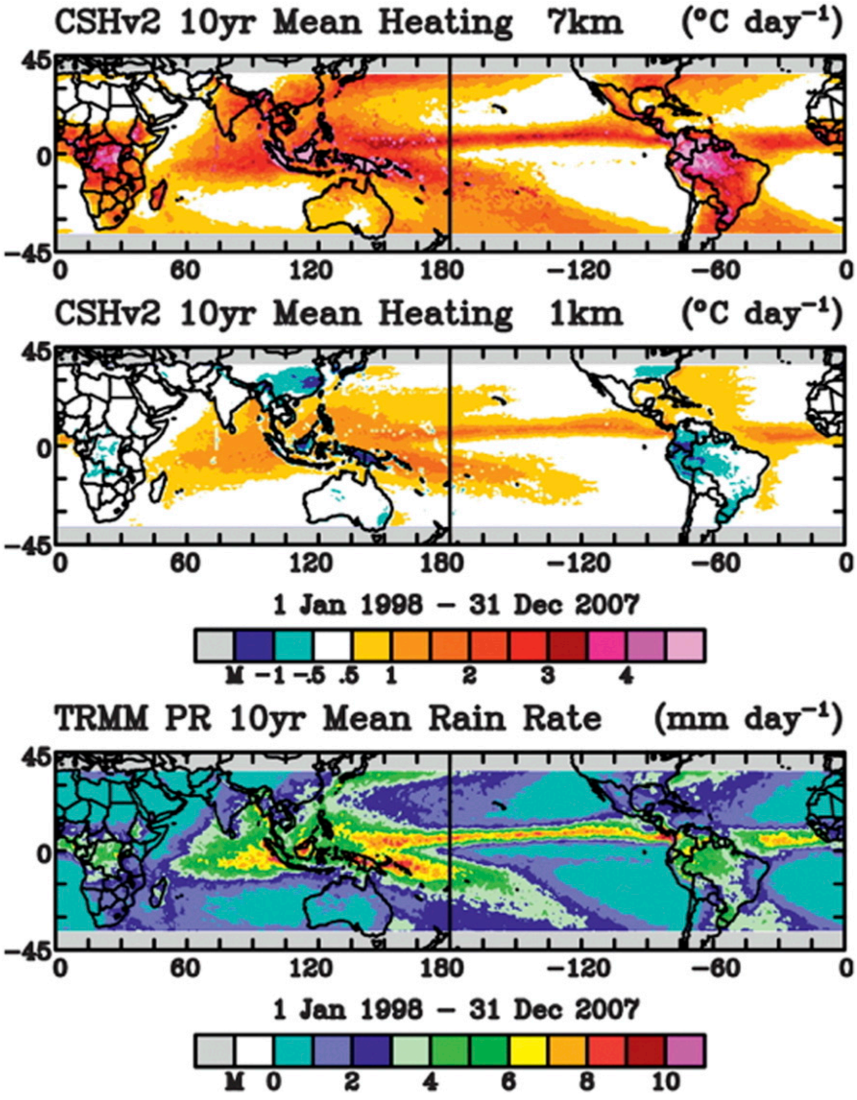

FIG. 4-3. Ten-year (1998–2007) mean latent heating rates from TRMM at (top) 7 and (middle) 1 km above ground level. (bottom) TRMM precipitation radar mean surface rainfall rate [after Tao et al. (2010)].

gauge analyses where feasible, at fine scales (0.25° × 0.25° and 3 hourly). The rainfall products were used for a variety of studies, including validating meteorological reanalyses, hydrologic modeling, analyzing oceanic precipitation systems, characterizing monsoon convection, and closing water budgets, as well as for other hydrometeorological applications. The TMPA was widely used in NASA activities for applications related to floods, landslides, agriculture, reinsurance, and disease.

For more than 17 years, the TRMM science team conducted innovative precipitation science and developed widely used applications that have benefitted society. The following provide a detailed summary of the TRMM's most significant achievements:

- *Accurate precipitation climatology*. TRMM data provide a baseline climatology of rainfall in the tropics, with a dramatic reduction in the range of uncertainty from previous space-based rainfall estimates (Adler et al. 2009). TRMM observations of the temporal variations in rainfall, from diurnal to interannual time scales, have revealed important variability associated with the Madden–Julian oscillation (MJO) and with the El Niño–Southern Oscillation (ENSO; e.g., L'Ecuyer et al. 2006; Arndt et al. 2010; Lau and Wu 2010; Waliser et al. 2009). TRMM has also provided estimated vertical profiles of latent heating in the tropics (Fig. 4-3), a key driver for global atmospheric circulation (Olson et al. 2006; Tao et al. 2010). In addition, potential human impacts on rainfall are related to processes associated with urban heat islands, deforestation, and aerosols (Hand and Shepherd 2009). This TRMM climatology has provided an important benchmark for global climate models including accurate annual, monthly, and diurnal tropical rainfall averages to which models can be compared.

- *Precipitation diurnal cycle.* TRMM allowed scientists to quantify the tropics-wide diurnal cycle of precipitation and convective intensity over land and ocean on fine spatial scales (0.25°; e.g., Nesbitt and Zipser 2003; Bowman et al. 2005; Hirose et al. 2008). In addition to studies characterizing the diurnal cycle on global scales, the accumulation of 17 years of data paved the way for studies of the diurnal cycle at regional scales (e.g., Chen et al. 2009; Takahashi et al. 2010; Sahany et al. 2010; Jackson et al. 2009).
- *Tropical convective system properties.* The TRMM PR, TMI, VIRS, and LIS supplied information for a Cloud and Precipitation Feature (CPF) database that provided a satellite climatology of the distribution of convective system characteristics (e.g., horizontal size, depth, and intensity); such a database is very useful for searching and sorting historical rainfall events (Liu and Zipser 2005; Liu 2011). The CPF database was used to document the global distribution of tropical deep convection, and to examine regional, seasonal, and diurnal variations of the rainfall contributions from various precipitation features (Liu et al. 2007). PR data were frequently used to characterize the vertical structure of convective systems in many climatologically important regions (e.g., Romatschke and Houze 2010; Jackson et al. 2009; Romatschke and Houze 2011).
- *Lightning.* LIS has led to a detailed global mapping of lightning distribution and its seasonal variations (Cecil et al. 2014). TRMM's lightning and rain information together have allowed scientists to quantify the lightning–convection relations for land and ocean (Petersen et al. 2005, 2006; Takayabu 2006). Knowing the lightning flash size/energy and flash type (ground or cloud flash) has led to better estimates/measurements of lightning nitrogen oxides emissions.

h. Global Precipitation Measurement

In February 2014, NASA and JAXA launched the Global Precipitation Measurement (GPM) *Core Observatory* (GPM-*CO*) spacecraft (Hou et al. 2014). The Dual-Frequency Precipitation Radar (DPR), built by JAXA, provides three-dimensional vertical profiles of precipitation rate and hydrometeor-size distributions within storm systems (Masaki et al. 2015; Seto and Iguchi 2015). The DPR consists of a Ku-band precipitation radar (KuPR) and a Ka-band precipitation radar (KaPR). The KuPR is an updated version of the TRMM 13.6 GHz PR while the KaPR operates at 35.55 GHz. The KuPR and the KaPR are coaligned with a 5-km footprint location on Earth. Differential attenuation between the Ku- and Ka-band frequencies provides rain/snow discrimination.

The GPM Microwave Imager (GMI), provided by NASA, estimates wide-swath precipitation rates and was considered the best-calibrated conically scanning radiometer in space (Wentz and Draper 2016). Figure 4-4 shows DPR's vertical structure and GMI's wide-swath data for Hurricane Nate in 2017. The measurement capabilities of the DPR and the GMI have made the GPM-*CO* an important dataset for studying precipitation at bulk microphysical (250-m vertical resolution), local (convective, <10 km), regional (mesoscale, tens to hundreds of kilometers), and global scales (hundreds to thousands of kilometers; Skofronick-Jackson et al. 2017).

The GPM-*CO* was designed to measure precipitation rates from 0.2 to 110 mm h^{-1} and detect falling snow from the tropics to the midlatitudes (±65° latitude; Hou et al. 2014; Skofronick-Jackson et al. 2017). As a critical component of the GPM mission, the GPM-*CO* functions as the reference calibrator; it unifies data (Berg et al. 2016) from a constellation of 10 (in 2017) domestic and international partner sensors to generate NASA's next-generation global Integrated Multisatellite Retrievals for GPM (IMERG; Huffman et al. 2017) with high temporal (30 min) and spatial (0.1° × 0.1°) resolutions. Through improved measurements of rain and snow, precipitation data from GPM provide new information such as details of precipitation structure and intensity; observations of hurricanes and typhoons as they transition from the tropics to midlatitudes; data to advance near-real-time (NRT) hazard assessment for floods, landslides, and droughts; inputs to improve weather and climate models; and insights into agricultural productivity, famine, and public health (e.g., Kirschbaum et al. 2017).

One of GPM's goals is to advance precipitation measurements from space. The additional high-frequency channels (KaPR on DPR and 166 and 183 GHz on GMI) are especially sensitive to light rain and falling snow (Munchak and Skofronick-Jackson 2013). Assessments of GPM-*CO* products show that rainfall retrievals (Petersen et al. 2016) have sensitivity down to 0.2 mm h^{-1}. GPM-*CO* also detects falling snow (e.g., You et al. 2017), an important capability as 50% of global rainfall starts as snow above the melting layer (Field and Heymsfield 2015). In addition, reducing the errors associated with the median mass diameter

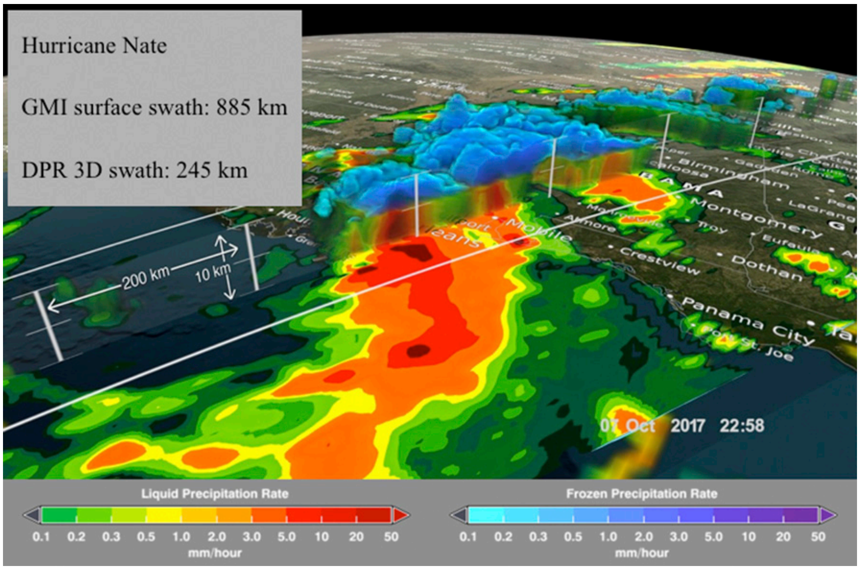

FIG. 4-4. GPM-*CO* observations of Hurricane Nate at 2258 UTC 7 Oct 2017 as it makes landfall.

improves knowledge of the microphysical properties (Petersen et al. 2016). Battaglia et al. (2016a) have shown that multiple scattering affects the Ka and Ku radar measurements for deep convective systems; a multiple-scattering forward-operator-based retrieval algorithm has been developed to minimize the effects. Hamada and Takayabu (2016) indicate that DPR observations will increase the occurrence and volume of observed precipitation by 20% and 2%, respectively, between 40°S and 40°N in comparison to the TRMM observations. As the microphysical understanding of falling snow and frozen precipitation above the freezing layer has evolved, the results show that nonspherical particles are essential for radiative transfer modeling simulations in order to match DPR and GMI (across all frequencies) and aircraft data taken during field campaigns (e.g., Kuo et al. 2016; Olson et al. 2016).

The GPM-*CO* measurements and the IMERG high spatial and temporal resolution merged-constellation products have contributed to improved knowledge of precipitation systems, water cycle variability, and freshwater availability. Liu and Liu (2016), Battaglia et al. (2016b), and Hamada and Takayabu (2016) reported on the improved characterization of storm structures while Liu and Zipser (2015) used the first year of GPM KuPR data to classify the largest, deepest, and strongest precipitation systems on Earth. Meanwhile, GPM continues to uncover the diversity of phenomena that are both important scientifically and crucial to our understanding the water cycle. These include results found by Battaglia et al. (2016b) of the first evidence of ghost echoes in the DPR dataset; these echoes correspond to a weak-echo region typically observed by ground-based S-band radar near the tilted convective core of a tornadic supercell. In addition, using GMI microwave polarimetric signals from the vertical and horizontal channels, Gong and Wu (2017) found that the scattering of frozen particles is highly polarized in the upper troposphere throughout the tropics and midlatitude jet regions, indicating that these particles are horizontally oriented.

GPM and TRMM data have been used to further improve quantitative precipitation estimates over land within the United States (e.g., Wen et al. 2016; Kirstetter et al. 2015) and internationally (e.g., Libertino et al. 2016). For example, Petkovic and Kummerow (2015) identified bias sources for the GMI algorithm for a flood event. Tan et al. (2016) compared error sources in IMERG attributable to individual instruments and found that the most reliable IMERG estimates come from passive radiometers, which is important for applying these estimates in hydrological studies. Maggioni et al. (2014) and Wright et al. (2017) provide error models in fine-resolution precipitation products for satellite hydrology applications. In other advances, Lin et al. (2015) developed a framework for dynamical precipitation downscaling through assimilating 6-h National Centers for Environmental Prediction (NCEP) Stage IV data using the WRF four-dimensional variational data assimilation (4D-Var) system.

i. Efforts toward advancing precipitation in climate models

GPM's estimates of cloud/precipitation microphysics, convective/stratiform separation, and latent heat release

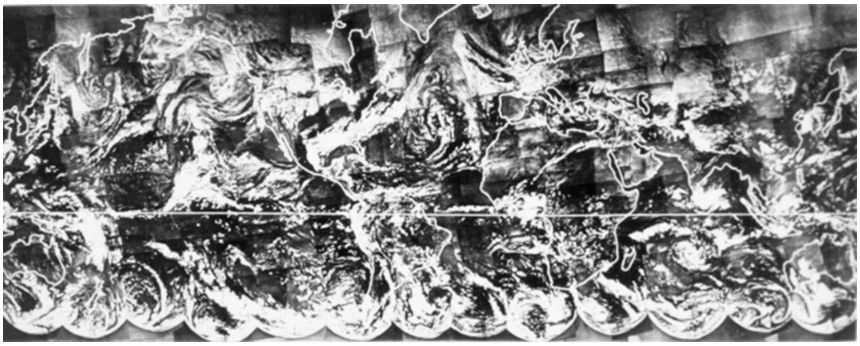

FIG. 4-5. The first complete global montage of the world's cloud patterns. Compiled from *TIROS-9* observations on 13 Feb 1965 (image source: NOAA Central Library).

in the atmosphere may improve the parameterization and initialization of climate models (Hagos et al. 2014; Tapiador et al. 2017). For example, using GPM field campaign data, Adirosi et al. (2016) compared raindrop size distributions to modeled size distributions and Tao et al. (2013) investigated the diurnal structure of precipitation, while Iguchi et al. (2014) used cloud resolving models to study melting-layer structure in mixed-phase precipitation and Colle et al. (2017) viewed the structure and evolution of warm frontal precipitation. In conjunction with other satellite datasets, Hill et al. (2016) used GPM data to confirm that the most modern global atmospheric reanalysis (ERA-Interim, produced by the European Centre for Medium-Range Weather Forecasts [ECMWF]), and global models tend to generate convection too early in the day affecting latent heat estimates.

The GPM mission is currently in extended operations after successfully completing its 3-yr prime mission lifetime on orbit. The GPM-*CO* has fuel on board that could last for more than a decade, which provides significant opportunities for additional measurements to maximize the scientific and societal benefits of the mission (contingent on instrument health). GPM will generate a consistent, uniform, and long-term next-generation precipitation record that covers the TRMM and GPM eras, potentially stretching to a 30-yr or more record depending on GPM-*CO* operations.

4. Weather monitoring and prediction

The first weather satellites simply took static pictures of Earth from space. Throughout the 1960s, NASA launched its first series of Earth-observing, polar-orbiting satellites: the TIROS missions. Ten experimental TIROS satellites were launched between 1960 and 1965, with nine operational TIROS satellites following between 1966 and 1969. *TIROS-1* provided a glimpse of Earth's synoptic cloud patterns. The first complete view of the world's cloud patterns was compiled from 450 individual images from *TIROS-9* on 13 February 1965 (Fig. 4-5). While crude by today's standard, it provided the long-sought-after global image of Earth's weather. The TIROS satellites were designed to be experimental—to prove whether scientists could effectively study Earth's weather from space; their success led to the launch of the TIROS-N series of satellites in 1978. The early TIROS-N satellites carried the AVHRR, providing day-and-night observations of clouds, oceans, and ice and snow, as well as the TIROS Operational Vertical Sounder (TOVS), which provided temperature and water vapor information from Earth's surface to the uppermost layer of the atmosphere.

The vertically integrated water vapor content of the atmosphere over the ocean is measured through clouds in the microwave portion of the spectrum (Alishouse et al. 1990). The SSM/I radiometer measurements were used to retrieve total precipitable water (TPW) operationally in support of weather forecasting. Other microwave instruments have been designed for a similar purpose, such as the Advanced Microwave Sounding Unit (AMSU) and the AMSR-E. Weather forecasters use animations of TPW to support prediction of heavy precipitation. From these animations, scientists developed the Morphed Integrated Microwave Imagery (MIMIC), which blends microwave retrievals to provide forecasters with a visualization of meteorological phenomena such as atmospheric rivers and tropical storms (Wimmers and Velden 2011). Using these images, forecasters monitored tongues of moisture from the tropical oceans that can cause heavy rain and flooding when they encounter land.

a. Nimbus satellites

The seven satellites of the Nimbus program were launched into a sun-synchronous polar orbit between

1964 and 1978. The nation's first research program based on satellite remote sensing, Nimbus made many contributions to our understanding of Earth and meteorology, including global images of clouds and large weather systems from *Nimbus-1*. *Nimbus-2* (1966–69) carried a medium-resolution infrared radiometer that mapped the distribution of atmospheric water vapor and carbon dioxide. Launched in 1969, *Nimbus-3* carried the Satellite Infrared Spectrometer (SIRS) and the Infrared Interferometer Spectrometer (IRIS) for measuring the emission spectra of the Earth–atmosphere system. IRIS provided the first high-spectral-resolution (5 cm^{-1}) infrared observations of Earth and became a reference for fingerprinting chlorofluorocarbons (CFCs) from observations three decades later. *Nimbus-4* (1970–80) flew infrared sounders and collected global observations of the ozone layer while *Nimbus-5* (1972–83) made initial estimates of rainfall over the oceans with the Infrared Temperature Profile Radiometer (ITPR) and the first microwave sounding device [the Nimbus E Microwave Spectrometer (NEMS)]. Improved atmospheric sounding was made possible with *Nimbus-6* (1975–83) and its HIRS. *Nimbus-7* carried eight experiments collecting data between 1978 and 1994. The seven Nimbus missions made unique observations that advanced the study of Earth sciences, in both science and technology.

Measurements from the *Nimbus-3* SIRS and the IRIS were used to demonstrate the capability of deriving atmospheric temperature profiles. Measurements at several wavelengths near an absorption band of a well-mixed gas, such as the 15-μm band of carbon dioxide or the 5-μm band of oxygen, combined with the radiative transfer equation can be used to retrieve vertical temperature profiles consistent with the measured radiances (Chahine 1968; Smith 1968). This research laid the groundwork for instruments flown on many follow-on satellite missions.

Water vapor profiles have been retrieved from satellite measurements by some of the same methods used to retrieve atmospheric temperature. Satellite measurements of water vapor from space go back to the Nimbus-7 satellite's Limb Infrared Monitor of the Stratosphere (LIMS) and the Stratospheric and Mesospheric Sounder (SAMS). Both instruments made observations at the 6-μm spectral region in the infrared to detect thermal emissions from the atmosphere. These water vapor measurements were continued with the TOVS package, which included the HIRS. Since that time, satellite instruments measuring infrared energy have been used to observe water vapor in the troposphere and stratosphere.

b. Geostationary satellites

Fueled by earlier successes with experimental sensors, scientists quickly realized the importance of cloud observations from a geostationary platform for weather forecasting. This orbit made it possible to monitor weather at the same approximate locations continuously. Great strides were made as routine imaging from the geostationary perspective quickly moved from the concept to the experimental and then operational stages; the experimental phase began in the mid-1960s, while the operational phase began in the mid-1970s and continues to this day. Satellites in geostationary orbit routinely monitor phenomena such as clouds, convection, hurricanes, fires, smoke, surface temperatures, atmospheric motions, snow cover, fog, and volcanic ash plumes.

Professor Verner E. Suomi defined the concept for a "cloud camera" on a geostationary satellite in 1964 (Lewis et al. 2018). This "storm patrol" would monitor the full disk every 10 min as storms and other weather phenomena develop. The era of imaging weather patterns from the geostationary perspective began on 6 December 1966 with the launch of an experimental sensor [Spin-Scan Cloudcover Camera (SSCC)] on board the *Applications Technology Satellite-1* (*ATS-1*; Suomi and Parent 1968). Although the full disk (or hemispheric view) imagery from the SSCC was "only" every 20 min, the time series animations of the Earth were still revolutionary. Because images were in the visible part of the electromagnetic spectrum, the SSCC only provided imagery during the day. This shortcoming was addressed when IR sensors were added to the VISSR on the Synchronous Meteorological Satellite (SMS) launched in 1974.

The first operational follow-on satellite was *GOES-1*, launched in October 1975 (Davis 2007). Launched as GOES-A, it was then designated *GOES-1* after attaining its geostationary orbit. Similar to *SMS-1*, the *GOES-1* imager carried a visible and IR sensor, supplying operational imagery for the first time. The real-time monitoring of clouds was a major advance in weather monitoring that transformed short-term weather forecasting (Benjamin et al. 2018). Animations of satellite images from geostationary satellites would also dramatically change how forecasters delivered weather information to the public (Henson 2010). As *GOES-2* and *-3* were clones of *GOES-1*, the next step forward in geostationary weather satellites came in 1980 on the *GOES-4* series, with the VAS (Menzel and Purdom 1994). While VAS was an experimental sensor on an operational spacecraft, it provided vertical profiling of atmospheric temperature and moisture in clear skies. From these measurements atmospheric stability parameters could be estimated. The VAS also provided more accurate cloud properties, over those from the imager alone.

The next advances in weather monitoring with geostationary satellites arrived with the GOES I-M series, starting with the launch of GOES-I (which became *GOES-8*) on 13 April 1994. The latest enhancements to better monitor Earth (Menzel and Purdom 1994) included one additional spectral band and finer spatial resolutions (e.g., from 7–14 km to 4–8 km, depending on the spectral band). The calibration performance was also improved. The *GOES-8* spacecraft was three-axis stabilized, as opposed to the spin-scan design of the earlier instruments. With a three-axis design, the instrument spends less time looking into space as the spacecraft spins, allowing for a longer dwell time collecting imagery of Earth. In addition, the *GOES-8* Imager exhibited less striping and a higher number of bits per pixel. The transition to *GOES-12* and beyond showed even finer spatial resolution for the water vapor band, going from nominally 8 to 4 km. Spacecraft improvements on *GOES-13*, *-14*, and *-15* allowed for more routine imaging during satellite eclipse times previously associated with periods of data outages. This era of geostationary platforms brought numerous science advances in the area of convection, turbulence, convective indices, total precipitable water, and fire detection and monitoring. Data assimilation from atmospheric sounding IR and microwave measurements improved weather forecasting and set the stage for advanced high-spectral-resolution IR observations.

The GOES-R series has led to significant scientific and technological advances over previous generations with the launch of *GOES-16* on 19 November 2016 (the first in a series of four satellites); GOES-S (*GOES-17*) was launched on 1 March 2018. The Advanced Baseline Imager (ABI) on board the GOES-R series is a state-of-the-art 16-band radiometer, with spectral bands covering the visible, near-infrared, and infrared portions of the electromagnetic spectrum (Fig. 4-6). Compared to the legacy series of GOES imagers, the ABI boasts improved spectral, spatial, and temporal resolution; radiometrics; and image navigation/registration (Schmit et al. 2017, 2018; Goodman et al. 2018).

Other countries are looking to achieve similar imager improvements with their own upgraded sensor designs. For example, Japan launched the Advanced Himawari Imager (AHI) in 2014; similar in design to the ABI, the AHI has a green channel (0.51 μm) in place of the ABI's 1.38-μm channel. Other advanced satellite imagers are planned on geostationary weather satellite programs for Meteosat Third Generation (MTG), South Korea, and China, among others. These geostationary imagers, along with those from the United States, form a global constellation of similar satellite instrumentation and usher in the modern era of advanced Earth monitoring from the geostationary perspective. These modern observations are orders of magnitude improved compared to legacy systems.

Compared to GOES legacy imager systems, the ABI and AHI have more spectral bands, higher spatial resolution, and a better coverage rate. Other areas of improvements include the signal-to-noise ratio (SNR), noise equivalent delta temperature (NEdT), the number of bits per pixel, image navigation and registration, and on-orbit visible calibration. None of the previous GOES imagers included a "blue" visible band, or a band sensitive to aerosols, which is key for building a natural color image, aerosol detection, and characterization. The last available true color image over the United States from the geostationary perspective was attained with *ATS-3* launched in 1967; ATS-3 had three visible bands, centered at the red, green, and blue wavelengths whereas the generation of GOES prior to *GOES-16* had just one visible band, rendering true color imagery impossible. With 16 spectral bands the ABI/AHI allows for a host of new or improved derived quantitative products. These include, but are not limited to: radiances, imagery, aerosol detection and optical depth and particle size, clear sky mask, cloud properties, atmospheric motion vectors, stability indices, shortwave radiation, fire characterization, hurricane intensity, land surface temperature, sea surface temperature, snow cover, ice properties, total precipitable water, and volcanic ash and sulfuric acid detection.

c. Convection

With the advent of satellite imagery, scientists were quick to begin assessing and analyzing atmospheric conditions and storm life cycle information (Houze 2018). The axis of the jet stream was estimated from cloud patterns observed from polar-orbiting satellites. All types of thunderstorms are recognizable by temporal imagery from satellites. Purdom (1976) demonstrated how to use satellite imagery to detect organization and cumulus cloud development as well as squall line formation. In addition, analysis of outflow boundaries on satellite imagery demonstrated that they could interact with an adjacent storm, thereby increasing the intensity of both storms.

It was satellite observations that led to the discovery of mesoscale convective complexes (MCCs), a complex of individual storms that covers a large area (100 000 km^2; Maddox 1980). Like squall lines, MCCs are long lived, lasting for more than 6 h. MCCs often begin forming in the late afternoon and evening and reach mature stages during the night and toward dawn.

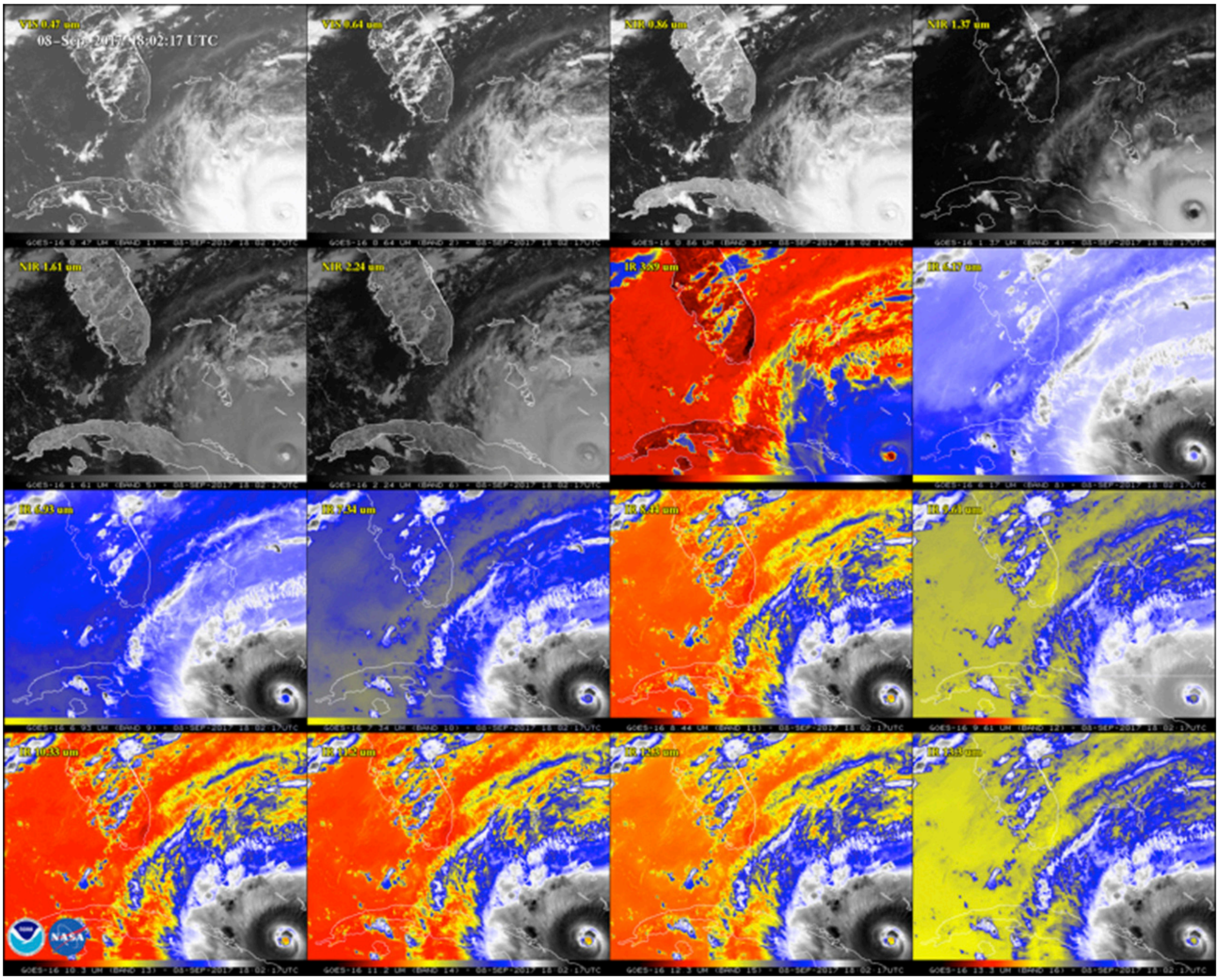

FIG. 4-6. *GOES-16* 16-band ABI on 8 Sep 2017 showing the 2 visible, 4 NIR, and 10 IR spectral bands.

In satellite images, MCCs appear as a cluster of thunderstorms that gives the appearance of a large circular storm with cold cloud-top temperatures below −40°C. MCCs are responsible for much of the summer rainfall in the midwestern United States, with their size, duration, and high degree of organization recognizable using infrared satellite imagery (Maddox 1980). Early satellite data aided in assigning the location of severe weather watches. Today we see satellite soundings being used operationally by forecasters to gain a 3D situational awareness of the mesoscale preconvective environment (Wheeler et al. 2018; Smith et al. 2018).

Overshooting tops on thunderstorms often indicate a high likelihood of severe weather associated with that storm. Satellite infrared images of severe thunderstorm anvils often exhibit an "enhanced-V," a V-shaped region of colder cloud tops extending downwind from the thunderstorm updraft. The V-shaped results from advection by the strong winds near the tropopause. A warmer "wake" is seen downstream (McCann 1983; Negri 1982; Heymsfield et al. 1983; Heymsfield and Blackmer 1988; Adler et al. 1983). The enhanced-V indicates a very strong updraft, and therefore a higher potential for severe weather. Forecasters use the enhanced-V and overshooting top features to support severe thunderstorm nowcasting and issue appropriate warnings (Bedka and Khlopenkov 2016). Satellite images of above-anvil cirrus plumes (AACPs) exhibit unique temperature and reflectance patterns and are easily identified in 1-min "super rapid scan" geostationary observations. Bedka et al. (2018) demonstrated that 73% of significant severe weather reports were produced by AACP storms and that the presence of an AACP can increase confidence in a forecast of large hail.

d. Tropical storms

Satellite imagery offered a critical opportunity to monitor hurricanes and tropical storms, particularly in areas where conventional measurements are unavailable (Emanuel 2019). The Dvorak technique (Dvorak 1975, 1984) was developed to determine hurricane and tropical storm intensity and was based on infrared imagery from geostationary observations. The technique matches satellite IR and VIS images to a number of possible pattern types from which a tropical (T) number and a current intensity (CI) number are derived. These indices were correlated with aircraft observations of storm intensity to derive the intensity of the storm under observation. The Dvorak technique continues to be the standard method for estimating tropical cyclone (TC) intensity where aircraft reconnaissance is not available. An update to this method, the advanced Dvorak technique (ADT) alleviates limitations found within the original Dvorak technique while remaining an easy-to-use TC intensity estimation guidance tool (Velden et al. 1998; Olander and Velden 2007). These measurements remain at the heart of today's operational satellite hurricane intensity estimates. Observations at microwave wavelengths were also developed to estimate hurricane intensity (Kidder et al. 1978; Velden and Smith 1983; Velden et al. 1984). The microwave observations measure the radial gradient of the warm core from which wind speeds can be derived (Kidder et al. 1980; Demuth et al. 2004). With *GOES-16* and *GOES-17*, the increased frequency of imagery will help with analyzing center location and identification. In particular, *GOES-16*/*-17* will make it easier to identify and track the low-level center of developing systems in the low cloud lines.

In addition to geostationary satellite data, passive microwave imagery from low-Earth-orbiting satellites (GPM, AMSR-2, SSM/I) assists in locating TC centers and monitoring TC structural evolution, such as eyewall replacement cycles. Satellite ocean surface vector winds from scatterometers (ASCAT) are also important in monitoring TC development, center location, intensity, and wind field structure. While hurricane track forecast accuracy has improved since 1990, there has been little improvement in intensity forecast accuracy. A new NASA mission, the Cyclone Global Navigation Satellite System (CYGNSS) uses eight microsatellites that will make accurate measurements of the winds at the ocean surface (Ruf et al. 2013), leading to better estimates of storm intensity.

e. Atmospheric motion vectors

Tracking clouds in a sequence of satellite imagery provides a means of estimating winds. Scientists observe the location of the same cloud in successive satellite images with a known time difference and measure the change in distance and direction (Hubert and Whitney 1971). Tracking cloud movements quickly became a methodology for defining flow patterns in the atmosphere (Hubert and Whitney 1971) with the beginning of the geostationary satellite era. The temporal resolution of the GOES imagery made tracking cloud movements and cloud motion vectors (CMVs) routine. The observed CMVs were used in initializing flow patterns in numerical weather prediction (NWP) models, especially over the oceans. A challenge to using cloud motion vectors in NWP is an accurate assignment of the cloud height. Analysis methods such as the CO_2 slicing approach improved cloud height assignment while the GOES water vapor channel (6.7 μm) was used to develop water vapor winds and track atmospheric motion vectors (AMVs) in the upper troposphere (Velden 1987; Weldon and Holmes 1991). AMVs derived from cloud-drift motions are assimilated into NWP models and led to improved forecasts (e.g., Gelaro et al. 2010). The International Winds Working Group was established in 1991 and holds biennial meetings to discuss and coordinate research and developments in data production, verification/validation procedures, and assimilation techniques.

f. Turbulence

Aviation turbulence can be grouped into two distinct categories: in cloud and clear air. Transverse band (or radial cirrus) signatures in satellite imagery are a common feature in the life cycle of a thunderstorm (Lenz et al. 2009). Areas of strong atmospheric turbulence over large regions are often characterized by extensive cloud cover, which sometimes contains well-defined transverse cirrus bands as observed in visible or infrared satellite imagery (Ellrod 1985). Transverse bands are also found near jet streams, the outflow of tropical cyclones, and the warm conveyor belt of midlatitude cyclones. Knox et al. (2010) provide a literature review and present detailed examples of the transverse band signature in satellite imagery.

Mountain, or lee, waves are caused when air flows over mountain ridges within a stably stratified atmosphere (Durran 1986). Strong vertical motions generated by the oscillating air currents of mountain waves can lead to turbulence. Clouds that form in the lee of mountain ranges are in rows almost parallel to the terrain disturbing the flow; these cloud signatures have been observed in satellite imagery (e.g., Fritz 1965; Ernst 1976; Ellrod 1985). In the absence of sufficient moisture in the atmosphere, wave clouds will not form, despite the fact that a well-developed lee wave and associated turbulence may exist. The 6.7-μm water vapor channel on satellite instruments has been used to study clear-air turbulence. Building on these early results, Uhlenbrock et al. (2007) analyzed MODIS 6.7-μm images with a 1-km nadir spatial resolution to study mountain wave patterns in conjunction with the turbulence severity noted by pilot reports (PIREPs). That study found that waves exhibiting interference-type patterns were concurrent with reports of high amounts of turbulence.

g. Lightning

In addition to the ABI, each of the GOES-R series spacecraft hosts a Geostationary Lightning Mapper (GLM), which is new to the geostationary orbit (Goodman et al. 2013). This instrument monitors total lightning, detecting the majority of lightning flashes, with a nearly uniform storm-scale spatial resolution of 8 km across most of the hemisphere with a product refresh rate of less than 20 s (Christian et al. 1989; Goodman et al. 2013). The GLM complements the ABI information for nowcasting and short-term forecasting of rapidly developing and severe convective weather (Goodman et al. 2013; Stano et al. 2014; Gravelle et al. 2016). The GLM will extend the lightning and thunderstorm climatology of the Western Hemisphere initially established by TRMM (Cecil et al. 2014; Albrecht et al. 2016).

h. Precipitation

TRMM data were heavily used by operational forecast centers (e.g., Rappaport et al. 2009) and the tropical cyclone science community, and played an important role in the monitoring and analysis of tropical cyclones (e.g., Blake and Pasch 2010; Kimberlain and Brennan 2011). The data helped establish key characteristics of the distribution and variation of rainfall in tropical cyclones as a function of intensity, stage of development, and environmental conditions (e.g., Lonfat et al. 2004; Chen et al. 2006). Both sea surface temperature (SST) and rainfall data from TRMM were often utilized to investigate the mechanisms responsible for storm genesis and rapid intensification (e.g., Braun 2010; Vianna et al. 2010). With its higher spatial resolution and frequent sampling in the 10°–37° latitude bands important for cyclone formation, TRMM data were frequently used for detecting the location and intensity of tropical cyclones, allowing for ~500 tropical cyclone center fixes per year by operational centers.

In combination with quantitative error characterization, GPM's precipitation-affected radiances and instantaneous precipitation rates have been assimilated into weather forecasting and data assimilation systems to improve 4D reanalysis. In fact, the GPM-*CO* data are being used operationally by the ECMWF (Geer et al. 2017). Assimilating satellite observations from microwave imagers such as GMI in cloudy and precipitating regions provides critical constraints on atmospheric parameters in dynamically sensitive regions and makes significant impacts on weather forecast accuracy. M.-J. Kim et al. (2017, unpublished manuscript) describe a framework to assimilate GMI all-sky (including cloud and precipitation affected) radiance data into the Goddard Earth Observing System Model, version 5 (GEOS-5), that will become part of the NASA Global Modeling and Assimilation Office's (GMAO) operational forecast system in 2018. Similarly, S. Q. Zhang et al. (2017) have developed an ensemble data assimilation system for the NASA Unified Weather Research and Forecasting (NU-WRF) Model, which can optimally integrate the information from high-resolution numerical model predictions and from GPM satellite data.

i. Atmospheric sounding

Atmospheric soundings are profiles of temperature and moisture that provide forecasters critical information on the structure and state of the atmosphere, such as instability, surface inversion, dry air layers, or cold air aloft. Nearly a century ago the first profile measurements were made with instruments attached to balloons, known as radiosondes, that measure the vertical atmosphere as a series of point-source measurements along the balloon path. Radiosondes have since become indispensable in achieving and maintaining high-quality forecasts. However, despite hundreds of daily launches, their sparse sampling and concentration over land in the Northern Hemisphere leaves large parts of the atmosphere unobserved. Satellites provide the only platform capable of consistently observing the entire planet on a routine basis.

In the 1950s scientists began to propose using remote sensing measurements of atmospheric gas concentrations to infer temperature structure. For example, King (1958) proposed that measurements at several tangential viewing angles could provide information on temperature structure with altitude. Kaplan (1959) suggested atmospheric profiling could be accomplished with measurements in several carefully selected spectral intervals by inverting the process of radiative transfer. Temperature profiles are derived using the emission from CO_2 bands, assuming a known CO_2 profile, and then concentrations of moisture are inferred from the water vapor in thermal emission bands. The different transmission characteristics of each band are used to derive information on temperature from different optical depths into the atmosphere. This method remains the basis for most operational temperature sounders used today.

Routine atmospheric temperature sounding measurements began with the Vertical Temperature Profile

Radiometer (VTPR) instruments on board the *NOAA-2* through *NOAA-5* satellites that operated from 1972 to 1979. These infrared radiometers had six temperature-sounding channels from 13 to 15 μm, plus a water vapor channel at 18 μm, and another channel in the 11-μm atmospheric window. The TOVS consisted of three instruments: HIRS/2, Stratospheric Sounding Unit (SSU), and Microwave Sounding Unit (MSU). Based on the HIRS instrument originally flown on *Nimbus-6*, the HIRS/2 is a 20-channel infrared radiometer with 12 temperature sounding channels covering both the 15- and 4.3-μm CO_2 bands, in addition to water vapor, ozone, and atmospheric windows. SSU, a development of the Pressure Modulated Radiometer (PMR) instrument, also flew on *Nimbus-6*. This sensor measured CO_2 emission at 669 cm^{-1} using three different pressure modulator cells (at 1.5, 5, and 15 hPa) for stratospheric temperature sounding.

The presence of clouds is the primary source of error in satellite sounding observations as an opaque cloud in the instrument field of view blocks transmittance from below the cloud. Removing the effects of clouds entirely from passive infrared observations is difficult, but methods exist to ameliorate them. For example, cloud clearing (e.g., Smith 1968) clusters coincident infrared and microwave radiance measurements to allow sounding observations of the clear-sky atmosphere around broken cloud fields. Microwave radiances are far less sensitive to nonprecipitation clouds than infrared observations.

The MSU was a four-channel microwave radiometer sounding the O_2 band across the 57-GHz oxygen band; at these frequencies clouds have a high transparency that reduces the effect of cloud on the temperature sounding. Consisting of two instruments that improved on the HIRS/2 and MSU, the Advanced TOVS (ATOVS) first flew on *NOAA-15* in 1998. With spectral channels similar to HIRS/2, the HIRS/3 is a 20-channel infrared radiometer, while HIRS/4 had improved spatial resolution and was flown on *NOAA-18* and *NOAA-19*. The MSU and SSU were eventually replaced with the AMSU, a 20-channel microwave radiometer designed for temperature and water vapor sounding.

Accurate observations of temperature and humidity are critically important to NWP. Sophisticated methods that accurately account for errors allow NWP systems to customize and optimize to produce the best forecasts possible. In the 1990s, NCEP and ECMWF introduced the direct assimilation of satellite radiances instead of rawinsonde-like retrieved (Benjamin et al. 2018; Derber and Wu 1998). Global forecast models assimilate radiance channels in the longwave infrared band because these are well characterized and stable (Eyre and Lorenc 1989; Benjamin et al. 2018). This approach has been shown to produce a positive impact on NWP (e.g., McNally and Vesperini 1996). Direct assimilating of more spectral channels, such as those sensitive to water vapor and ozone absorption, as well as retrieved profiles of temperature, mixing ratio, and trace gases remain important research topics, especially as computational capability and error accounting continue to improve (e.g., Jones and Stensrud 2012). There are efforts to assimilate retrieved parameters from satellite observations. Cloud properties from near-real-time retrievals of Minnis et al. (2008) are being assimilated in various models in both operational and experimental WRF models. For example, assimilation of hourly cloud-top pressure and temperature in the NOAA operational Rapid Refresh model (Benjamin et al. 2016) improved forecasts. Chen et al. (2015, 2016) assimilated cloud water path and found improved WRF analyses and forecasts of temperature and winds, as well as improved threat scores for precipitation. Jones et al. (2016) also assimilate cloud water path into a high-resolution WRF for severe storm prediction. Much remains to be done to maximize the value of satellite observations in NWP models because only a fraction of the available information is being used operationally.

Under the original POES program, NOAA aimed to maintain operational satellites in two different sun-synchronous polar orbits: one with a southward equator crossing at around 0730 local time (morning orbit) and one with a northward equator crossing at around 1430 local time (afternoon orbit) so that coverage of any point is repeated every 6 h. With the launch of *MetOp-A* in 2006, EUMETSAT took over responsibility for the morning orbit. This satellite, the first of three, contains both HIRS/4 and AMSU instruments (for continuity) as well as new instruments for temperature sounding: an infrared Fourier-transform spectrometer and a global positioning system (GPS) receiver.

After *NOAA-19* (launched in 2009), the United States planned to merge the NOAA and military polar-orbiting weather satellite programs into the National Polar-Orbiting Operational Environmental Satellite System (NPOESS). The NPP (NPOESS Preparatory Project) satellite was launched in October 2011 and later renamed *Suomi NPP*. While the NPOESS project has been abandoned, the NOAA component continued as the Joint Polar Satellite System (JPSS) in the afternoon orbits; the military program continued with the Defense Weather Satellite System (DWSS) in the morning orbits. The *SNPP* and *JPSS-1* and *-2* satellites contain two new instruments for temperature sounding: the Cross-Track Infrared Sounder (CrIS), an infrared Fourier-transform spectrometer; and the Advanced Technology

Microwave Sounder (ATMS), which is an improved version of AMSU.

j. Hyperspectral infrared sounders

The observing capability of early sounders was limited to measuring only one or two broad layers of the vertical atmosphere, but as NWP systems improved, the impact of these satellite observations on the forecast decreased. It took the development of new satellite sounding technology to address this shortcoming. Hyperspectral sounders now scan the infrared portion of the electromagnetic spectrum with thousands of channels spectrally narrow enough to resolve the thermodynamic structure and chemical composition in fine enough detail to continue to improve forecasts (Smith et al. 2009).

The launch of NASA's *Aqua* platform in 2002 with a pair of microwave and hyperspectral infrared sounders enabled a true 3D observational capability for the first time. These instruments observe Earth's atmosphere with uniform sampling at multiple pressure layers from the surface to the top of the atmosphere. This 3D observing capability has become an invaluable component of NWP, real-time weather forecasting, and storm analysis, so much so that 15 years later, high-spectral-resolution infrared sounders in LEO include the Atmospheric Infrared Sounder (AIRS; Aumann et al. 2003) on *Aqua*, the Infrared Atmospheric Sounder Interferometer (IASI; Cayla and Pascale 1995) on the EUMETSAT MetOp satellites, and the CrIS (Glumb et al. 2002), which is scheduled to be in LEO well into 2040.

Microwave observations enable soundings in both clear and nonprecipitating cloudy-sky conditions, while hyperspectral infrared observations enable soundings in clear-sky regions but at much higher vertical resolution. Ferraro et al. (2005) showed the importance of microwave sounders to weather forecasting and analysis, in particular with regard to low-level moisture plume transport and the relation to precipitation, while a number of studies demonstrated how high-spectral-resolution infrared sounder data improve global NWP forecasts out to 7 days (Chahine et al. 2006; Le Marshall et al. 2006; Jones and Stensrud 2012). These instruments help capture the full picture of the atmospheric state in clear and cloudy scenes.

Apart from improvements to NWP, these well calibrated high-spectral-resolution radiance measurements from satellites ushered in a new era of weather applications that use the retrieved sounding products, not the raw radiances (e.g., Smith 1991; Hilton et al. 2012; Weisz et al. 2015; Berndt et al. 2016, 2017; Berndt and Folmer 2018; Iturbide-Sanchez et al. 2018; Smith et al. 2018; Wheeler et al. 2018). National Weather Service (NWS) forecasters need independent observations to verify NWP models in real time. An improvement in one NWP model may cause disagreement with another, and satellite sounding observations help forecasters determine which NWP model best reflects conditions on the ground as the storm system evolves.

Because of the thousands of spectral channels, computationally fast methods for retrieving atmospheric profiles from radiance measurements are required for operational use. Two of the most common methods to retrieve soundings from radiance measurements are linear regression (Weisz et al. 2007; Smith et al. 2012; Weisz et al. 2013) and optimal estimation (Rodgers 2000). In 2008, NOAA adopted the NOAA Unique Combined Atmospheric Processing System (NUCAPS; Sun et al. 2017; Gambacorta and Barnet 2018; Nalli et al. 2018a,b) to generate sounding products operationally. A NUCAPS sounding is a compound product and includes temperature and water vapor profiles, column amounts of trace gases (O_3, CO, CH_4, SO_2, HNO_3, CO_2, and N_2O), and cloud and surface properties.

NUCAPS achieves high accuracy by running a regression retrieval that uses all infrared and microwave spectral channels (Goldberg et al. 2003) to generate a first guess for the optimal estimation retrieval step. This final retrieval step improves upon the regression first guess by using a radial transfer model (RTM) with carefully selected subsets of channels (Gambacorta and Barnet 2013) to sequentially retrieve thermodynamic and composition parameters. With this approach, NUCAPS is computationally fast enough to meet the operational needs but benefits from the accuracy and error accounting enabled by RTM calculations for each sounding. NUCAPS is the AIRS heritage algorithm (Susskind et al. 2003) and the NOAA operational system for all LEO platforms—*MetOp-A*/*-B*, *SNPP*, and the JPSS series—and retrieves soundings in clear and partly cloudy atmospheres with high vertical resolution (an order of magnitude higher than coincident microwave sounders alone or broadband infrared sounders on GEO platforms) and associated error estimates. Operational forecasters depend on error estimates to understand and use these products correctly.

After more than a decade of concerted efforts in product validation with dedicated field campaigns and in situ measurements (Nalli et al. 2013, 2016, 2018a,b; Sun et al. 2017), NUCAPS recently became available within the NWS Advanced Weather Interactive Processing System II (AWIPS-II). This allows forecasters to test and evaluate NUCAPS products interactively against heritage products. As a result, new applications are emerging that draw not only on the vertical information of each sounding but also on the spatial information from the full swath of soundings (Smith et al. 2018). NUCAPS soundings describe the variation in atmospheric features (e.g., instability, stratospheric O_3 intrusions, biomass burning plumes, or cold air aloft) as well as the atmospheric state around these features (e.g., gradients of temperature and moisture content). Field campaigns such as the 2016 NOAA El Niño Rapid Response (Dole et al. 2018) and 2019 Fire Influence on Regional and Global Environments Experiment (FIREX) continue to help assess product accuracy as well as product suitability in various applications.

In December 2016, China launched its next-generation geostationary meteorological satellite *Fengyun-4-01* (*FY-4-01*) carrying the Geosynchronous Interferometric Infrared Sounder (GIIRS). An infrared hyperspectral vertical sounder with 1650 spectral channels, the GIIRS is the first spaceborne interferometer to fly in geostationary orbit. EUMETSAT plans to have a hyperspectral sounder in geostationary orbit by 2023 and as part of their Meteosat Third Generation program.

k. GPS-RO

The GPS network provides high-precision navigation. The system consists of satellite signals and a network of support stations that receive data. These GPS satellite signals are slowed by the atmosphere, which results in a delay in the signal's arrival as compared to the signal's propagation in space. Radio signals from GPS satellites are refracted as they travel through the atmosphere, and the amount of refraction can be measured from other satellites. As one satellite sets or rises with respect to the other, sequences of refraction angles are measured. These measurements can be converted into a vertical profile of the index of refraction of the atmosphere and thus into a vertical temperature sounding with high vertical resolution (Ware et al. 1996; Kursinski et al. 1997, 2000; Kuo et al. 2004). Radio occultation sounding is often referred to as Global Positioning System Radio Occultation (GPS-RO).

The joint Taiwan–U.S. Constellation Observing System for Meteorology, Ionosphere, and Climate (COSMIC)/Formosa Satellite Mission 3 (COSMIC/FORMOSAT-3, hereafter COSMIC) mission was launched in April 2006 and consisted of a constellation of six microsatellites. The data include electron counts in the ionosphere and, key for weather, atmospheric profiles of temperature, moisture, and pressure in the troposphere and stratosphere. GPS-RO soundings have had a positive impact on numerical weather forecasting (Luntama et al. 2008; Cucurull 2010; Healy et al. 2005; Anthes 2011).

Feltz et al. (2014) demonstrated that the COSMIC GPS-RO network has the spatial coverage, time continuity, and stability to provide a common reference for comparison of the microwave and infrared sounder profile products. The GPS-RO dry temperature was useful for evaluating microwave and infrared sounder temperature profiles in the 300–10-hPa region.

5. Atmospheric composition (trace gases and aerosols)

a. Nadir backscatter UV instruments

Nadir UV instruments measure the solar radiation backscattered by the Earth in the Hartley–Huggins ozone absorption band (250–340 nm). This measurement series started in April 1970 with the launch of the Backscatter Ultraviolet Spectrometer (BUV) on the *Nimbus-4* satellite. Since that time, more than a dozen such instruments have flown on various NASA, NOAA, and international satellite platforms. Recent instruments have a hyperspectral capability and extended wavelength range to measure boundary layer trace gases, such as SO_2, HCHO, BrO, and NO_2.

Dave and Mateer (1967) first determined that estimating ozone columns from nadir UV measurements is theoretically possible. Mateer et al. (1971) then applied the method to produce the first retrieved column and profile data from the *Nimbus-4* BUV. An improved version of the BUV instrument, the Solar Backscatter Ultraviolet radiometer (SBUV), was launched on the *Nimbus-7* satellite along with the Total Ozone Mapping Spectrometer (TOMS). Based on the same measurement principle, the TOMS was designed to provide daily global total ozone maps of the sunlit Earth while the BUV/SBUV instruments only produce measurements at the subsatellite locations along the orbit. The TOMS mapping capability is now standard among recent nadir UV instruments.

This TOMS instrument and its follow-ons have played a key role in monitoring the polar ozone depletion. The ozone hole, the unexpected precipitous decline in the ozone column above Antarctica, was first discovered in 1985 in ozone column data from a ground instrument, a Dobson Spectrophotometer, at Halley Bay, Antarctica (Farman et al. 1985). It exemplifies the global and detrimental impact of human activity on Earth's atmosphere. The first satellite image (Fig. 4-7) of the Antarctic ozone hole was produced from data from the *Nimbus-7* TOMS launched in 1978 and was presented at a symposium in 1985 (Bhartia et al. 1985). It demonstrated that the ozone hole is a continental-scale phenomenon. *Nimbus-7* SBUV data further indicated that the depletion was occurring in the lower stratosphere and had a strong seasonal cycle (Bhartia et al.

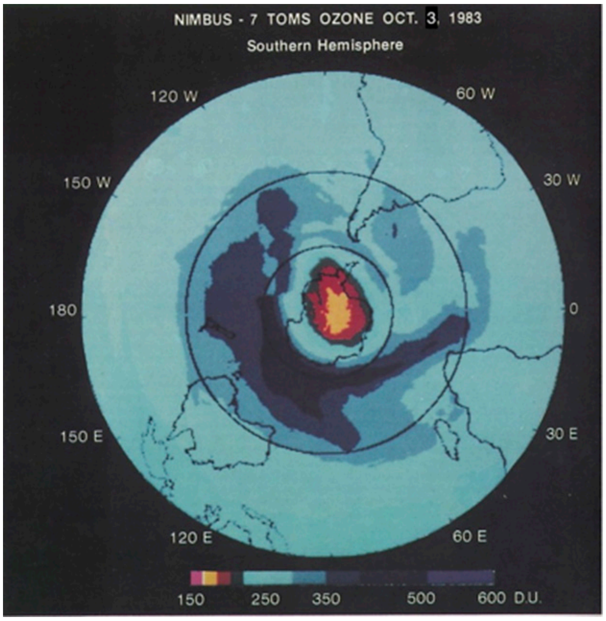

FIG. 4-7. First image of the ozone hole over Antarctica from TOMS data, which was first presented by Bhartia et al. (1985) and first published by Callis and Natarajan (1986).

1985). Published in popular print, this first TOMS image of the ozone hole (e.g., Sullivan 1985) resonated with the public, sounding an alarm on the human impact on our atmosphere. TOMS and SBUV data documented the beginnings of the ozone hole, while the earlier *Nimbus-4* BUV had established a baseline.

Successor instruments, such as the Ozone Monitoring Instrument (OMI), continue the nearly four-decade-long ozone column record. These continuous observations do not conclusively indicate that the ozone hole is yet recovering, though they do show that its depth and spatial extent have recently stabilized.

The TOMS and its follow-on instruments have also been used to derive a long-term record of aerosol optical depth over oceans and continents (Herman et al. 1997; Torres et al. 1998). The methodology uses radiances in the 330–380-nm range to retrieve optical depth and single scattering albedo of tropospheric aerosols. The TOMS aerosol index (AI) measures the change in spectral contrast in the near ultraviolet due to radiative transfer effects of aerosols in a Rayleigh scattering atmosphere. The approach detects aerosols over land and ocean surfaces (Hsu et al. 1999). AI is positive for absorbing aerosols, near zero (±0.2) in the presence of clouds or large size (0.2 μm or larger) nonabsorbing aerosols and negative for small-size nonabsorbing particles.

The retrieved aerosol properties have been applied to the *Nimbus-7* (January 1979–April 1993) and Earth Probe (July 1996–December 2000) TOMS record. The resulting time series shows the seasonal cycle of mineral dust aerosols in the Northern Hemisphere and carbonaceous aerosols in the Southern Hemisphere. The effects of two major volcanic eruptions of the last 40 years, El Chichón in 1982 and Mt. Pinatubo in 1991, are distinguished in the TOMS AI record. The derived climatology would illustrate the sources and spatial distribution patterns of the most predominant aerosol types.

- From November to March, large aerosol amounts are generated by biomass burning activities in the sub-Sahelian region. Dense smoke plumes spread over the Atlantic Ocean within 10° of the equator. The Northern Hemisphere component of this aerosol plume in February is enhanced by the outset of the Saharan dust flow.
- Saharan dust outbreaks characterize aerosols in the spring months. Saharan dust outbreaks transport large amounts of dust over the Mediterranean and the Middle East.
- During April–June aerosols are intensively generated in the Northern Hemisphere while the Southern Hemisphere is relatively free of anthropogenic aerosols with an average value of about 0.3 over the oceans and even smaller (less than 0.2) over the remote continental regions of South America, South Africa, and Australia.
- March–April in Central America, Southeast Asia, and China marks the beginning of the Northern Hemisphere biomass-burning season. The Central American smoke plume spreads both west over the Pacific Ocean and northwest covering a vast area of the western United States.
- June–August mark the easterly flow of dust from northern Africa across the Atlantic Ocean. Intense dust flow activity is also observed over other well-known arid areas such as the Arabian Peninsula and northern India.
- The intense Southern Hemisphere biomass-burning season starts in July in central Africa. The smoke plume from these fires is a persistent feature from July to December. The peak of the biomass-burning season in South America takes place in August and September.

b. Stratospheric Aerosol and Gas Experiment

The Stratospheric Aerosol Measurement (SAM) and Stratospheric Aerosol and Gas Experiment (SAGE) advanced our knowledge of stratospheric aerosol characteristics. Astronauts conducted the first SAM measurements by pointing instruments at the sun to measure path extinction. SAM II was a single wavelength (1 μm) sun photometer carried on board the *Nimbus-7* satellite. SAGE I (launched 18 February 1979) used solar attenuation in four spectral regions to yield altitude profiles of aerosol extinction at wavelengths of 1000 and 450 nm, as well as profiles of ozone and nitrogen dioxide concentration. These two satellite systems began a global record of particulates in the upper atmosphere, providing latitudinal, longitudinal, and temporal variations of aerosols in 1-km layers of the upper atmosphere.

Launched in October 1984 as part of the ERBS program (McCormick 1987; Poole and McCormick 1990), SAGE II vertically scans the limb of the atmosphere during the spacecraft's 15 sunrises and sunsets each day. SAGE I and SAGE II observations showed that ozone decreased in the upper stratosphere over the high latitudes of both hemispheres (McCormick et al. 1992). In addition, SAGE II measurements monitored the transport of volcanic aerosols across the entire tropical stratosphere and into the middle and high latitudes in the months following the eruption of Mt. Pinatubo (McCormick and Veiga 1992). The increased concentration of aerosols resulted in a 2.5°–3°C warming of the stratosphere near Mt. Pinatubo. SAGE II measurements also contributed to the finding that volcanic aerosols destroy nitrogen dioxide. Overall, the 10 years of high-resolution water vapor measurements by SAGE II led to better understanding of the chemistry and motion of the stratosphere.

The SAGE III instrument, a grating spectrometer, measures ultraviolet and visible energy with a spectral coverage from 280 to 1040 nm and a spectral resolution of about 1.2 nm. It also includes a channel at 1550 nm for distinguishing between aerosols and clouds, and for measuring larger aerosols. The SAGE III flew on *Meteor-3M*, a Russian satellite launched in 2001, and lasted 5 years. A second SAGE III instrument has been on the International Space Station (ISS) since early 2017 and continues the SAGE data record.

c. Limb-viewing thermal emission instruments

Limb-viewing thermal emission instruments can measure ozone and many other traces gases at higher vertical resolution than nadir UV instruments. The LIMS launched on the *Nimbus-7* satellite was the first such instrument; unfortunately, it lasted only 6 months as its detector was cooled using a solid cryogen.

A significant advancement in limb thermal emission measurements occurred with the 1991 launch of the UARS mission from the Space Shuttle. It was designed to study the physical and chemical processes in the upper atmosphere with a goal of better understanding atmospheric photochemistry and transport (Reber 1993; Dessler et al. 1998). This mission was the first satellite to collect long-term data records of key chemical species in the atmosphere and demonstrated the chlorofluorocarbons in the stratosphere were human-made. Further, it established the direct correlation between 3D distributions of observed ozone depletion and reactive chlorine. The UARS MLS observations were critical to demonstrating that the water vapor transport into the stratosphere is tied to tropospheric tropical convection and the upper-tropospheric tropical temperature.

Mt. Pinatubo erupted in the Philippines just before the launch of UARS, ejecting a significant amount of sulfuric acid aerosols into the tropical stratosphere. UARS observations were used to track the aerosol cloud and monitor the transport of these aerosols around the global stratosphere over the next year.

Most of the key measurements of stratospheric traces gases started by UARS continued with the launch of an improved MLS instrument on the *Aura* satellite in July 2004. MLS measures microwave thermal emission from the limb of Earth's atmosphere to estimate vertical profiles of atmospheric gases, temperature, pressure, and cloud ice. MLS measures the vertical profiles of ozone and many chemical species that affect it. In particular, MLS

- provided the first global measurements of stratospheric and mesospheric OH and HO_2, the key chemicals in hydrogen chemistry that destroy ozone;
- measures chlorine monoxide (ClO), the primary form of chlorine that destroys ozone, and hydrogen chloride (HCl), the primary relatively inactive "reservoir" form of stratospheric chlorine;
- measures bromine monoxide (BrO), which is both the primary form of bromine that destroys ozone and the primary form of bromine in the stratosphere; and
- measures water vapor (H_2O), nitric acid (HNO_3), and temperature that provide key information on polar processes that can lead to large ozone losses in the Antarctic.

MLS observations provide information for global air quality research; in particular, they play a significant role in monitoring global transport of polluted air in the upper troposphere. MLS measurements of the N_2O and CO—so-called "tracers" of pollution transport—and geopotential height, provide information on atmospheric transport that helps separate the effects of atmospheric motion from chemical destruction while measurements of volcanic SO_2 help diagnose the effects of volcanoes on the ozone layer. Cloud ice measurements, along with H_2O at lower altitudes, provide information on the processes by which air from below enters the stratosphere.

d. Tropospheric trace gases

The first satellite instrument to measure tropospheric ozone from space, the TOMS instrument, employed a

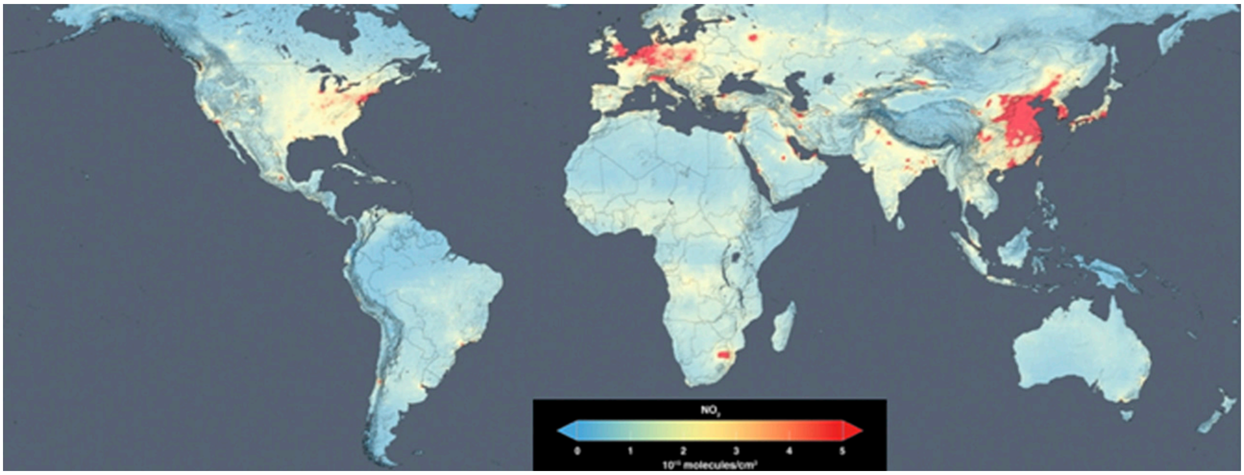

FIG. 4-8. The global distribution of NO_2 in 2005 as determined from data from the Dutch–Finnish OMI on board NASA's *Aura* satellite. (Image courtesy of NASA's Goddard Space Flight Center.)

cloud slicing technique (Ziemke et al. 1998). However, the technique works best in the tropics and provides only the tropospheric column ozone (TCO). Global estimates of TCO have become possible since 2005 by combining *Aura* MLS stratospheric ozone and *Aura* OMI total column ozone (Ziemke et al. 2006). These measurements show small but significant increases in TCO lower in the troposphere. The ESA's second European Remote Sensing Satellite (*ERS-2*) Global Ozone Monitoring Experiment (GOME) was launched in 1995 and measured ultraviolet and visible wavelengths over a large spectral range (240–790 nm) and with high enough spectral resolution (0.2–0.4 nm) to retrieve trace gases such as NO_2, formaldehyde (HCHO), ozone, and bromine monoxide (BrO) in both the stratosphere and troposphere (Burrows et al. 1999). Despite GOME's coarse spatial resolution (40 × 320 km^2), the first global maps captured elevated levels of NO_2 over the industrial regions of Asia, North America, and Europe, as well as distinct "hot spots" near large cities, such as Los Angeles. Though GOME data are atmospheric columns, the tropospheric portions of the columns for some species can be separated from the stratospheric portion, allowing for estimates of emissions and surface concentrations. It is not currently feasible to infer near-surface ozone levels from an atmospheric column; however, GOME retrievals of NO_2 and HCHO serve as proxies for two important ingredients, NO_x and volatile organic compounds (VOCs), for surface ozone formation (e.g., Martin et al. 2004).

Since GOME's launch, complex changes in worldwide biomass burning and anthropogenic pollution levels have been documented by GOME and its similar, but improved, successor instruments, including ESA's Environmental Satellite (ENVISAT) SCIAMACHY, GOME-2, and OMI. Figure 4-8 shows the global distribution of NO_2 concentration from OMI on board NASA's *Aura* satellite. Combining data from these sensors makes it possible to estimate trends of concentrations and emissions of NO_2, sulfur dioxide (SO_2), HCHO, and other tropospheric species from 1996 to present.

Together, emission estimates of this suite of tropospheric trace gases have been and remain critical input to atmospheric models that simulate the historical evolution of tropospheric composition, including important trace gases like ozone and hydroxyl radical, the atmosphere's primary cleansing agent. In addition, estimates of global pollutant trends are being used to estimate the impacts of pollution on human health and develop pollution mitigation strategies.

Launched 15 July 2004, the *Aura* satellite platform is devoted to atmospheric chemistry. *Aura*'s four instruments [OMI, Tropospheric Emission Spectrometer (TES), High Resolution Dynamics Limb Sounder (HIRDLS), and MLS] study the atmosphere's chemistry and dynamics, addressing questions about ozone trends, air quality (e.g., carbon monoxide) changes, and their linkage to climate change. Developed by the Netherlands's Agency for Aerospace Programs (NIVR) in collaboration with the Finnish Meteorological Institute (FMI), OMI, with its hyperspectral capabilities, continues global monitoring of total ozone trends from satellite measurements; it also measures air quality indicators such as NO_2, SO_2, BrO, OClO, and aerosol characteristics. OMI can distinguish between aerosol types, such as smoke, dust, and sulfates. The TES, a Fourier transform spectrometer whose heritage traces back to the IRIS aboard the *Nimbus-4* spacecraft (Hanel and Conrath 1969), provided simultaneous observations of CO and tropospheric O_3 vertical profiles (Beer et al. 2001). These simultaneous observations were valuable for distinguishing between natural and anthropogenic sources of ozone (Fishman and Seiler 1983). Similarly, the IASI observations on *MetOp-A* provide concurrent retrievals of CO, tropospheric O_3, and CH_4 along with the GOME-2, which is also on board *MetOp-A*, which retrieved NO_2. These combined measurements are critical for understanding the complex interplay between atmospheric dynamics and chemistry that determines tropospheric ozone. The value of concurrent measurements is enhanced through data assimilation in air quality modeling (Pierce et al. 2003, 2007).

The NASA *Terra* Measurement of Pollution in the Troposphere (MOPITT; launched in 1999) is a Canadian instrument that measures infrared wavelengths and provides CO column concentration, a species important in tropospheric chemistry and which serves as an excellent tracer of pollution transport (Drummond and Mand 1996). MOPITT measures CO in the troposphere, with relatively coarse vertical resolution, but with good horizontal sampling. MOPITT's measurements led to the discovery that wildfires in North America and Siberia were surprisingly strong sources of CO and altered the carbon uptake by ecosystems (Lamarque et al. 2003; Edwards et al. 2004). High concentrations of CO coincided with the location of fires and aerosol plumes from *Terra* MODIS. Combined with model analysis, the fires in summer 2004 generated ~30 Tg of CO, roughly equivalent to the total U.S. anthropogenic CO emissions during that time.

e. Aerosols

In the 1960s and 1970s, early weather satellites produced visible images with "anomalous gray shades" that were sometimes associated with dust and anthropogenic smoke (e.g., Fett and Isaacs 1979). This was confirmed with observations from the AVHRR at 0.63 μm that demonstrated the transport of dust outbreaks over the ocean (Prospero et al. 1970). However, poor radiometric calibration and the few spectral bands limited quantitative applications of the data to aerosol research. Analysis of aerosol retrievals from AVHRR reflectance measurements revealed seasonal patterns of major dust, smoke, and pollution aerosol plumes on a global scale. Analyzing AVHRR data between July 1989 and June 1991, Husar et al. (1997) demonstrated that the winter peak in grassland burning produces a smoke plume over the Atlantic Ocean west of the sub-Saharan region. In summer, dust from North Africa and smoke from central Africa produce plumes over the adjacent water, while dust from the Middle East engulfs the Arabian Sea. In addition, pollution sources off the East Coast of the United States are more prominent in summer than other times of the year. MODIS observations made it possible to improve on these aerosol optical depth (AOD) retrievals from imagers with its high radiometric calibration accuracy and stability (Hsu et al. 2012).

The MODIS aerosol products consist of dark target (Kaufman et al. 1997; Remer et al. 2008; Levy et al. 2013) and deep blue (Hsu et al. 2013; Sayer et al. 2014) algorithms. Collectively, these products monitor aerosol optical thickness over the oceans and continents. MODIS aerosol data have been compared with measurements made at Earth's surface and have been shown to be suitable for monitoring air quality events over local, regional, and global scales (Chu et al. 2003; Wang and Christopher 2003; Engel-Cox et al. 2004). Zhao et al. (2017) used observations from MODIS and MISR to investigate decadal-scale trends in aerosol loading and properties during 2001–15 over three populous regions: the eastern United States, western Europe, and eastern and central China. In all of these regions, the magnitude of AOD trends is much larger in summer than that in winter. The study explored the relationship of AOD trends to air pollutant emission changes. Annual mean AOD values decreased along with emission reductions in all major pollutants, except for mineral dust and NH_3. In the eastern and central China region, AOD increases before 2006 coincided with emission increases induced by rapid economic development, and decreases after 2011 were in association with the effective emission reduction in primary aerosols, SO_2, and NO_x.

Satellite observations of column aerosol burdens are commonly used in air quality forecasting (Al-Saadi et al. 2005), despite the fact that air quality forecasts are concerned with concentrations at "nose level." Aerosol profiles from *CALIPSO* better characterize their transport paths with height, which aids the evaluation of model simulations (e.g., Eguchi et al. 2009). The aerosol vertical profiling from CALIOP has advanced our understanding of the global 3D distribution of aerosols (Winker et al. 2013). Vertical distributions of aerosol vary with season in conjunction with seasonal variations in source strengths and transport mechanisms. With its profiling capability and ability to distinguish between depolarizing dust and nondepolarizing smoke and marine aerosols, CALIOP also provides insights into the intercontinental transport of dust and smoke. Recent aerosol emission and transport studies with CALIOP include convective transport (Chakraborty et al. 2015), trans-Atlantic dust transport from North Africa (Yu et al. 2015), Asian dust transport (Huang et al. 2008;

Yumimoto and Takemura 2015), and anthropogenic dust discrimination (Huang et al. 2015). CALIOP provides an accurate measurement of volcanic aerosol vertical distribution over the globe (e.g., Vernier et al. 2011).

Detection and impact studies of aerosols that lie above clouds have similarly relied on *CALIPSO*'s strengths. Chand et al. (2009) have used CALIOP observations to estimate the radiative effects of smoke located above low clouds; their research indicated that the warming effect of the smoke is coupled to the underlying cloud properties, complementing A-Train passive-only approaches (Waquet et al. 2013; Jethva et al. 2013; Meyer et al. 2015). More recently, the ISS Cloud-Aerosol Transport System (CATS) backscatter lidar, with its sensitivity, was able to better resolve the aerosol structure overlying stratocumulus clouds in the southeast Atlantic (Rajapakshe et al. 2017).

6. Societal benefits

Satellite measurements are essential to weather research and establishing skill in operational environmental forecasts. The skill of numerical weather prediction models is sensitive to the accuracy and distribution of the observations used to initialize them. Filling the large gaps in conventional weather observation systems, satellite observations improve weather forecasts to the benefit of society. Satellite observations have been demonstrating their value ever since the launch of the world's first satellite sounding instrument SIRS-A in April 1969. Since then, significant improvements in forecast accuracy have been realized, in part because of this bird's eye view of our planet. Multispectral imagery, especially in time sequence, is critical for the world's national weather services to improve their situational awareness, particularly when faced with impending severe weather.

For example, GPM data provide critical information to end-users that helps to improve their understanding of Earth's water cycle and facilitates decision-making (Kirschbaum et al. 2017). Listed below are just a few examples of the application of GPM:

- GPM data are being integrated into the multiagency, multinational Famine Early Warning System Network (FEWS NET; https://www.fews.net/).
- GPM has been important in contributing to food–water–energy dialogues (Shepherd et al. 2016).
- The Naval Research Laboratory (NRL) Automated Tropical Cyclone Forecasting System (https://www.nrlmry.navy.mil/TC.html) integrates GMI data at time scales of less than 1 h into their system to improve tropical cyclone location fixes.
- The Air Force Weather Agency (557th Weather Wing) incorporates GMI data into their WRF Model, delivering operational worldwide weather products to the Army and Air Force, unified commands, national programs, and the National Command Authorities.
- Extreme precipitation leading to flood or landslide events, and the characterization of potential hazards, are a source of several GPM investigations: an NRT Global Flood Monitoring System (Wu et al. 2014), a regional and global Landslide Hazard Assessment model to provide estimates of potential landslide activity around the world in NRT (Stanley and Kirschbaum 2017), and the Global Fire Weather Database (GFWED), which integrates different weather factors influencing the likelihood of the initiation and spreading of vegetation fires (Field et al. 2015). Short-term forecasts of soil moisture are available from the NASA Land Information System to better understand the land–atmosphere interactions on scales of days to years (Kumar et al. 2006).
- The IMERG NRT data have also been used to track environmental conditions on the ground in order to predict and validate the risk of cholera infection (Khan et al. 2017) and to characterize mosquito-breeding habitats in an effort to identify areas with higher disease risk (Pan et al. 2014).

Aviation is another major area in which satellites provide benefits to society, whether in terms of efficiencies or, more importantly, safety (Mecikalski et al. 2007). Wind forecasts help with saving fuel while identifying fog and turbulence helps to protect lives and aircraft. Smith et al. (2012) and Yost et al. (2018) detail the use of near-real-time cloud property analyses to provide nowcasts of airframe and engine icing, respectively. During the day visible images can be used to identify fog. The "fog" image is generated from the temperature difference between the 3.7-μm images and the 11-μm infrared images. The temperature difference depends primarily on emissivity differences caused by different physical characteristics of the radiating surfaces.

Volcanic ash advisories are another example where satellite observations support the needs of airlines and society. Volcanic eruptions can eject ash to altitudes where commercial aircraft fly. Spectral differences between different IR channels are used to identify the plume (e.g., Pavolonis et al. 2013). Such an algorithm was applied to the EUMETSAT Spinning Enhanced Visible and Infrared Imager (SEVIRI) in geostationary orbit to detect and track the volcanic ash plume from the Eyjafjallajökull eruption in 2010. In formation on the location of the ash cloud was used by, among others, the London Volcanic Ash Advisory Center (VAAC).

Rerouting, delays, and canceled flights can be frustrating but necessary for passenger safety.

Then there are timely forecasts of cold air aloft ($<-65°C$) that can help pilots redirect flight paths to save aircraft fuel from freezing. Ice crystals that form when upper-air temperature falls below −65°C are known to have caused aircraft accidents in the past. Forecasters in Alaska use NUCAPS temperature retrievals operationally to issue Meteorological Impact Statements (MISs), which equip the aviation community with the information they need to maintain safety and efficiency.

7. Paradigm changes

a. Constellations coincident in space and time

Coordinating diverse observations on temporal and spatial scales has increasingly become a priority. As the science evolves from specialized disciplines to broader interdisciplinary questions, linking physical, chemical, and dynamic processes across a range of scales becomes critical. Practically speaking, such scientific requirements mean that a single satellite will be unable to provide the required suite of instrumentation necessary to observe all the relevant geophysical variables. Unfortunately, large multi-instrumented and multipurpose satellites can lead to cost and schedule difficulties. A popular alternative is to fly a set of smaller satellites, each with its own suite of observations, as part of a synergistic orbital constellation.

NASA, along with several international partners, pioneered modern Earth science constellation flying with the International Afternoon Constellation (or A-Train), so named because the constellation of satellites was placed into a sun-synchronous polar orbit, crossing the equator in an ascending (northbound) orbit at about 1330 local time (Stephens et al. 2002; L'Ecuyer and Jiang 2010).

The first two A-Train satellites were the flagship-class NASA EOS *Aqua* (2002) and *Aura* (2004) platforms, both consisting of multiple instruments primarily to study the water–energy cycle and atmospheric chemistry, respectively, in addition to other Earth system science. *Aqua* flew international instrument contributions from Japan (JAXA) and Brazil [Instituto Nacional de Pesquisas Espaciais (INPE)] while *Aura* flew a contributed instrument from the Netherlands. The French Centre National d'Etudes Spatiales (CNES) *Polarization and Anisotropy of Reflectances for Atmospheric Sciences Coupled with Observations from a Lidar* (*PARASOL*) mission joined the A-Train in 2004, flying an imaging polarimeter to study aerosols and clouds. The constellation reached a mature capability with the 2006 co-manifest launch of the NASA Earth System Science Pathfinder (ESSP) program's *CloudSat* (cloud radar) and NASA–CNES *CALIPSO* (aerosol–cloud lidar and infrared imager) missions. Later additions were JAXA's *Global Change Observation Mission–Water* (*GCOM-W1*; 2012), flying an improved version of the AMSR-E microwave imager on *Aqua*, and NASA's Orbiting Carbon Observatory 2 (OCO-2), with spectrometers for column CO_2 retrievals. To date, all satellites remain in the A-Train with the exception of PARASOL, which lowered its orbit out of the constellation in 2009. The main focus of A-Train synergy was to better understand global 3D cloud and aerosol distributions and other process-related properties, and their influence on the water/energy and budget (e.g., L'Ecuyer et al. 2008). Further details on A-Train sensors and example science are found in the previous sections.

The A-Train satellites fly within minutes, or less, of each other (Fig. 4-9), which minimizes significant changes in the instruments' observing conditions. However, precise flight coordination is not required. NASA-managed A-Train coordination is implemented by assigning spatial "control boxes" for each satellite's operations, with bounds that typically represent less than a minute of flight time. Within the control box, satellites are free to maneuver as needed. Only *CloudSat* and *CALIPSO* maneuvers are closely coordinated to ensure coincident active sensor ground tracks. We note the distinction between constellation flying and formation flying, where the latter requires precise interspacecraft spacing and coordinated maneuvers [e.g., NASA's two Gravity Recovery and Climate Experiment (GRACE) spacecraft].

A recent development is the use of low-cost SmallSat solutions for Earth observations (see section 7b). The NASA CYGNSS mission, launched in 2016 as the first Earth Venture Mission, is an example of a SmallSat constellation. CYGNSS consists of eight microsatellites (~60-cm maximum dimension) flying in close proximity to one another, using ocean-reflected GPS signals to infer ocean surface wind speed in all precipitating conditions, including tropical cyclones. CYGNSS leverages a long heritage of ocean scatterometry, including QuikSCAT (1999) and ISS-RapidScat (2014). Collectively, the eight-satellite constellation provides 32 simultaneous wind measurements per second.

b. Noncoincident constellations

In a broader context, constellation flying also can be used to describe the nontemporal synergy of observations. A distributed satellite system can be particularly useful for precipitation research due to the sampling challenges inherent in capturing useful precipitation

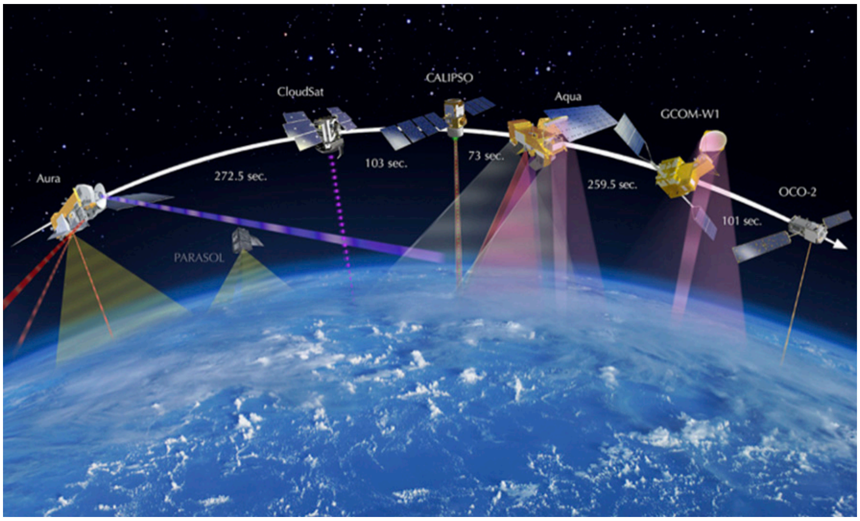

FIG. 4-9. Nominal mean temporal spacing between international afternoon constellation satellites as of 2017. Individual sensor observation geometries are shown by semitransparent colors assigned to different parts of the electromagnetic spectrum. While the PARASOL satellite is shown for historical completeness, the platform exited the constellation in 2009 (image courtesy of https://atrain.nasa.gov/images.php).

statistics on a global scale. As detailed elsewhere in the chapter, the international GPM mission consists of data provided by the NASA *Core Observatory* (JAXA Ka- and Ku-band precipitation radar, NASA microwave conical scanning radiometer) along with a constellation of 10 (as of 2017) domestic and international partner sensors (Huffman et al. 2017). Together these partners achieve global passive microwave coverage (conical or cross-track scanning) with high sampling frequency.

Another example of a distributed constellation is the long-standing international coordination effort for meteorological and space weather satellite observations. This includes operational sun-synchronous polar satellites (including *SNPP* as well as the new JPSS series, DMSP, MetOp, Meteor, and FY providing coordinated morning or afternoon coverage) and geosynchronous satellites [currently GOES; Meteosat; Himawari; Communications, Ocean, and Meteorological Satellite (COMS); Indian National Satellite System (INSAT); and FY), as well as other spaceborne assets. Technical progress is often coordinated using common sensors. For example, the latest generation of geosynchronous satellites now fly the ABI on *GOES-16*, *GOES-17*, and future GOES-R series satellites, the similar AHI on *Himawari-8*, and the Advanced Meteorological Imager (AMI) on the *Geostationary–Korea Multi-Purpose Satellite-2A* (*GEO-KOMPSAT-2A*; launched on 4 December 2018).

The atmospheric chemistry and air quality communities also benefit from coordinated geosynchronous observations. The NASA Tropospheric Emissions: Monitoring Pollution (TEMPO) instrument, Korea Aerospace Research Institute (KARI) Geostationary Environment Monitoring Spectrometer (GEMS) instrument on GEO-KOMPSAT-2B, and the ESA's Sentinel-4 mission will inaugurate a global geosynchronous constellation for studying aerosols and trace gas emissions and processes. The three international contributions will uniquely support studies of air quality and large-scale transport between Asia, North America, and Europe. TEMPO, NASA's inaugural Earth Venture Instrument, carries an imaging UV–visible spectrometer providing hourly North American coverage that will fly on a commercial satellite (2020/21 timeframe); the TEMPO instrument is being developed in tandem with GEMS. The European Copernicus Programme's Sentinel-4 flies a similarly capable imager on the Meteosat Third Generation Sounder (MTG-S) platforms (starting in 2023) providing coverage over Europe and North Africa. All of the constellation imagers have a nominal spatial resolution of ~8 km and temporal resolution of 1 h.

Distributed constellations of SmallSats are also being developed. Funded through the NASA Earth Science Division Earth Venture Instrument element, the Time-Resolved Observations of Precipitation Structure and Storm Intensity with a Constellation of SmallSats (TROPICS) mission comprises twelve 3U CubeSats (discussed below) flying scanning microwave radiometers in three low-Earth orbital planes. TROPICS is planned for launch by 2021.

As we look ahead to new Earth science missions, constellation flying needs to be an inherent part of future research programs, and should necessarily include the broader domestic and international partner community. The value of constellation flying not only is in reducing cost and schedule pressures in increasingly budget-constrained environments, but also to allow for the technology and science to evolve dynamically as new sensors are launched into the constellation.

c. Platform innovations

Technological advances are enabling meaningful Earth science to be accomplished on SmallSats, platforms usually considered having a mass less than several hundred kilograms. Subcategories include microsatellites (10–100 kg) and nanosatellites (1–10 kg). With rapidly improving capabilities and reliability, these small platforms are low-cost alternatives to existing measurement needs, and they offer novel observing techniques not possible with traditional satellite buses and their associated costs (e.g., the CYGNSS 8-microsatellite and TROPICS 12-CubeSat constellations discussed above).

CubeSats began as academic and technology demonstration platforms, starting with the CubeSat Project (1999) standardization effort led by Robert Twiggs (Stanford University) with refinement from Jordi Puig-Suari (California Polytechnic State University), leveraging a deployment method first developed by Aerospace Corporation (NASEM 2016). This nanosatellite single unit (1U) standard is defined as a volume 10 cm × 10 cm × 10 cm, with a mass less than 1.33 kg, that can be stacked in multiple combinations (2U, 3U, 6U, 12U). The satellites are typically placed into orbit as secondary payloads or, more recently, carried to the ISS and launched with dedicated CubeSat deployment devices.

CubeSats have received attention in recent years for their science and operational potential. The science value of CubeSats was reviewed in the U.S. National Academy of Sciences 2016 report on CubeSats (NASEM 2016), where it was recommended that federal agencies and foundations [NASA and the National Science Foundation (NSF), in particular] should ''consider conducting a review and developing a plan to address CubeSat-related policies to maximize the potential of CubeSats as a science tool.'' In particular, the NASEM report noted that Earth-observing LEO CubeSat constellations could provide global diurnal observations that are not possible with sun-synchronous observations.

According to the NASEM report, 425 CubeSats had been launched through 2015; between 2013 and 2015, about 55%, 21%, and 24% of CubeSats were from commercial, university, and government providers, respectively, though commercial providers (e.g., for Earth imaging) were growing substantially faster than the others. NASA and NSF had launched 19 CubeSats with science objectives as of the report's publication [see Table 1.3 in NASEM (2016) for a summary of recent NASA- and NSF-funded CubeSat projects].

Several CubeSat technology demonstration programs are active at NASA. The Science Mission Directorate's (SMD) Advanced Technology Initiatives Program (ATIP) and Earth Science Technology Office (ESTO) In-Space Validation of Earth Science Technologies (InVEST) program have funded a number of CubeSat missions. Between 2016 and 2017, this included the launch of Radiometer Assessment Using Vertically Aligned Nanotubes (RAVAN), IceCube (carrying an 883-GHz radiometer for ice cloud studies), and Microwave Radiometer Technology Acceleration (MiRaTA) mission. RainCube, an InVEST program launched in May 2018, will measure precipitation, will be the first active-remote sensing radar on a CubeSat platform (Ka band). The Temporal Experiment for Storms and Tropical Systems Technology Demonstration (TEMPEST-D) technology demonstration of a millimeter-wave radiometer (90–183 GHz) is part of the Earth Venture Technology initiative. Nominally scheduled for launch in 2018, the Hyper-Angular Rainbow Polarimeter (HARP) is a hyperangular imaging polarimeter viewing at multiple angles, four wavelengths, and three polarization angles designed for aerosol and cloud studies.

Other related NASA efforts include the Goddard Space Flight Center Dellingr technology demonstration project. Dellingr is a 6U CubeSat that was deployed from ISS on 20 November 2017, carrying three heliophysics-related instruments as well as new technology components and subsystems. More broadly, the NASA CubeSat Launch Initiative (CSLI) was begun by the NASA Launch Services Program to provide launch access for CubeSats built (and funded) by education and nonprofit organizations, as well as NASA centers. Through CSLI, the Educational Launch of Nanosatellites (ELaNa) project has, to date, provided access to space to 58 CubeSats competitively selected and flown on 16 ELaNa Missions since 2011; 50 more are manifest for flight as of this writing.

This increased activity in CubeSat missions goes against the historic trend of increasing instrument data rate, mass, and power requirements (Table 4-1). The data rate, mass, and power have generally increased by an order of magnitude between early generation imagers/sounders and recent versions. Active sensors are in the high end of the mass/power range. Data volumes are growing rapidly as research programs combine data

TABLE 4-1. Examples of the data rate, mass, and power of early era and recent satellite instruments (from www.wmo-sat.info/oscar/instruments) along with two small satellites (Ruf et al. 2018).

Instrument	Data rate (Mbps)	Mass (kg)	Power (W)
Imagers			
AVHRR (original)	0.621	33	27
MODIS	10.6 (peak daytime)	228	162
Sounders			
HIRS (original)	0.011	14	10
HIRS/4	0.003	35	24
AIRS	1.27	156	220
CrIS	1.5	165	123
Active sensors			
CALIOP (*CALIPSO*)	0.332	156	124
CPR (*CloudSat*)	0.015	230	270
Small satellites			
CYGNSS (single microsatellite)	4	25	38
IceCube (1.3 U CubeSat)	0.001	1.0	5.6

from different instruments with ancillary data and output from numerical models. The amount of data involved in research is growing at an unprecedented rate. This requires improved research computing and cyberinfrastructure. Large satellite datasets increase the need for good metadata and large data repositories. The ability to execute complex algorithms will pose challenges. Scientific analysis applied across these large quantities of data in reasonable amounts of time will lead to new applications of data analytic tools.

At the other extreme from SmallSats, the International Space Station provides several external facilities for mounting remote sensing instruments. With a 52° inclination (~400-km altitude, 90-min orbit), the ISS does not provide global coverage but does allow for diurnal observations, a sampling capability not otherwise available from sun-synchronous platforms. With its precessing orbit, the ISS flies over locations on the Earth between approximately 52°N and 52°S latitudes, yielding similar solar illumination for 3–4 days every 90 days. This orbit allows for improved spatial resolution and variable solar conditions compared to the sun-synchronous orbits. The ISS is a unique platform as it carries a human crew, who can collect data while on the spacecraft and can swap out instruments or sensor systems when needed. Earth science instruments deployed on the ISS in 2017 include SAGE III, LIS, Cloud-Aerosol Transport System (CATS), and Total and Spectral Solar Irradiance Sensor (TSIS-1). The ISS is becoming an increasingly popular deployment site, especially for Earth Venture [Global Ecosystem Dynamics Investigation (GEDI), ECOsystem Spaceborne Thermal Radiometer Experiment on Space Station (ECOSTRESS)] and continuity-based (SAGE-III, LIS, TSIS-1, OCO-3) observations.

Decades earlier, the Space Shuttle provided similar flight opportunities. Notable examples include the series of Atmospheric Laboratory for Applications and Science (ATLAS) missions flown 1992, 1993, and 1994 (Kaye and Miller 1996) and Lidar In-Space Technology Experiment (LITE) flown in 1994 (McCormick 1993; Winker et al. 1996). ATLAS included instruments for measuring total and spectral solar irradiance as well as middle- and upper-atmospheric chemistry. Correlative measurement opportunities included the UARS (Reber 1993; Dessler et al. 1998) that launched in 1991 and carried versions of ATLAS's Active Cavity Radiometer Irradiance Monitor (ACRIM; total) and Solar Ultraviolet Spectral Irradiance Monitor (SUSIM; spectral) solar irradiance instruments. LITE was a three-wavelength (355, 532, 1064 nm) cloud and aerosol backscatter lidar that flew in the Space Shuttle. With its 53 h of data collection, LITE was the first such lidar in space, validating lidar technologies and science capabilities that were a pathfinder for the CALIOP lidar on *CALIPSO*.

8. Summary

The view from space uniquely enables the monitoring and study of atmospheric conditions and processes. Satellite remote sensing has undergone such rapid progress since the first Earth observation platform was launched in 1958 that this chapter can only provide a brief overview of the great variety of sensors, platforms, and orbits that have been used to provide atmospheric observations over a wide range of temporal and spatial scales. As mentioned in the introduction, the scope of this overview was necessarily limited primarily to U.S. satellite observational efforts.

Satellite observations are the critical backbone of an increasingly interdependent and international Earth observing system that advances our understanding of Earth system science and thereby improves prediction of weather, climate, and natural hazards. One of the most important means for continuing progress is an ongoing fleet of spacecraft dedicated to the task of watching our skies. However, an ongoing challenge in Earth science is the need to balance sustained multidecadal continuity measurements, required to monitor climate change and evaluate climate models, against the desire for novel measurement approaches that will provide new insight into Earth system science processes (NASEM 2015). In particular, interagency funding and mechanisms to enable sustained measurements have been problematic; NASEM (2018) contains a good discussion of the strategic difficulties in planning and implementing continuity in the United States. As noted with the ISS examples above, new platform capabilities can play a cost-effective role in obtaining some aspects of continuity measurements.

As important as continuity is new programs that leverage new technologies to observe Earth. Passive sensors retrieve winds by feature tracking in time sequences of images and are widely used in weather forecasting. The future will see Doppler wind lidars from spaceborne platforms that will track motions indicated by molecular and aerosol backscatter and measure the vertical profile of the horizontal wind vector. For example, ESA's new Aeolus mission, launched on 22 August 2018, carries a laser Doppler instrument to measure line-of-sight winds (Reitebuch 2012.) Future lidar missions will likely include High Spectral Resolution Lidar (HSRL) techniques (e.g., Grund and Eloranta 1991), which independently retrieve aerosol or cloud extinction and backscatter without a priori assumptions on lidar ratio or aerosol type. Satelliteborne radar systems are producing estimates of precipitation (e.g., TRMM and GPM) and cloud vertical structure (e.g., *CloudSat*) and will continue to be a part of future satellite observations of Earth. Radar technologies relevant to spaceborne cloud and precipitation measurements radars have advanced significantly. Precipitation processes fundamentally couple vertical velocities to hydrometeor production and multifrequency (e.g., Ku/Ka/W band) Doppler radar observations together with passive radiometer measurements and cloud-resolving models will yield process-oriented measurements to study cloud and precipitation processes that should lead to improved weather forecasting and climate prediction. Many of these technologies are part of the Earth Clouds, Aerosol and Radiation Explorer (EarthCARE) satellite. This is a joint mission by the ESA and JAXA scheduled for launch in 2021 (Illingworth et al. 2015). The mission will retrieve global profiles of cloud, aerosol, and precipitation properties using observations from a cloud profiling radar with Doppler capability, high-spectral-resolution lidar, and multispectral imager.

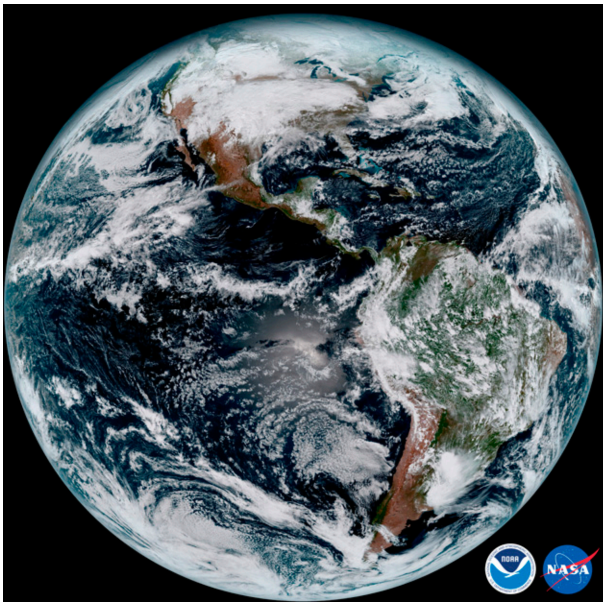

FIG. 4-10. A composite color full-disk visible image at 1307 EDT 15 Jan 2017 created from spectral measurements from the *GOES-16* ABI instrument (data source: https://www.nesdis.noaa.gov/sites/default/files/assets/images/abi_full_disk_jan_15_2017_high_res.jpg).

Observations from today's satellites (Fig. 4-10) achieve Dr. Wexler's vision that satellite observations can inspire and provide observations that advance atmospheric research. Planning for missions that effectively and efficiently provide the measurements needed for future research is critical. Continuing a fleet of spacecraft dedicated to the task of watching our skies remains one of the most important means of studying, and understanding, our planet's atmosphere.

Acknowledgments. The authors are thankful for the comments, resources, and suggestions provided by S. Braun, C. D. Barnet, M. D. King, C. Kummerow, C.D. Barnet, M. Goldberg, and G. Stephens. The authors also appreciate and thank the thoughtful comments by reviewers. The views, opinions, and findings contained in this report are those of the authors and should not be construed as an official National Oceanic and Atmospheric Administration or U.S. government position, policy, or decision.

REFERENCES

Ackerman, S. A., and S. K. Cox, 1981: GATE Phase III mean synoptic-scale radiative convergence profiles. *Mon. Wea. Rev.*, **109**, 371–383, https://doi.org/10.1175/1520-0493(1981)109<0371:GPIMSS>2.0.CO;2.

——, and ——, 1987: Radiative energy budget estimates for the 1979 southwest summer monsoon. *J. Atmos. Sci.*, **44**, 3052–3078, https://doi.org/10.1175/1520-0469(1987)044<3052:REBEFT>2.0.CO;2.

——, K. I. Strabala, W. P. Menzel, R. A. Frey, C. C. Moeller, and L. E. Gumley, 1998: Discriminating clear-sky from clouds with MODIS. *J. Geophys. Res.*, **103**, 32 141–32 157, https://doi.org/10.1029/1998JD200032.

——, R. E. Holz, R. Frey, E. W. Eloranta, B. C. Maddux, and M. McGill, 2008: Cloud detection with MODIS. Part II: Validation. *J. Atmos. Oceanic Technol.*, **25**, 1073–1086, https://doi.org/10.1175/2007JTECHA1053.1.

——, A. Heidinger, M. J. Foster, and B. Maddux, 2013: Satellite regional cloud climatology over the Great Lakes. *Remote Sens.*, **5**, 6223–6240, https://doi.org/10.3390/rs5126223.

Adirosi, E., E. Volpi, F. Lombardo, and L. Baldini, 2016: Raindrop size distribution: Fitting performance of common theoretical models. *Adv. Water Resour.*, **96**, 290–305, https://doi.org/10.1016/j.advwatres.2016.07.010.

Adler, R. F., and A. J. Negri, 1988: A satellite infrared technique to estimate tropical convection and stratiform rainfall. *J. Appl. Meteor.*, **27**, 30–51, https://doi.org/10.1175/1520-0450(1988)027<0030:ASITTE>2.0.CO;2.

——, M. J. Markus, D. D. Fenn, G. Szejwach, and W. E. Shenk, 1983: Thunderstorm top structure observed by aircraft overflights with an infrared radiometer. *J. Appl. Meteor.*, **22**, 579–593, https://doi.org/10.1175/1520-0450(1983)022<0579:TTSOBA>2.0.CO;2.

——, J.-J. Wang, G. Gu, and G. J. Huffman, 2009: A ten-year rainfall climatology based on a composite of TRMM products. *J. Meteor. Soc. Japan*, **87A**, 281–293, https://doi.org/10.2151/jmsj.87A.281.

Albrecht, R. I., S. J. Goodman, D. E. Buechler, R. J. Blakeslee, and H. J. Christian, 2016: Where are the lightning hotspots on Earth? *Bull. Amer. Meteor. Soc.*, **97**, 2051–2068, https://doi.org/10.1175/BAMS-D-14-00193.1.

Alishouse, J., S. Snyder, J. Vongsathorn, and R. Ferraro, 1990: Determination of oceanic total precipitable water from the SSM/I. *IEEE Trans. Geosci. Remote Sens.*, **28**, 811–816, https://doi.org/10.1109/36.58967.

Al-Saadi, J., and Coauthors, 2005: Improving national air quality forecasts with satellite aerosol observations. *Bull. Amer. Meteor. Soc.*, **86**, 1249–1261, https://doi.org/10.1175/BAMS-86-9-1249.

Anthes, R. A., 2011: Exploring Earth's atmosphere with radio occultation: Contributions to weather, climate and space weather. *Atmos. Meas. Tech.*, **4**, 1077–1103, https://doi.org/10.5194/amt-4-1077-2011.

Arkin, P. A., and P. E. Ardanuy, 1989: Estimating climatic-scale precipitation from space: A review. *J. Climate*, **2**, 1229–1238, https://doi.org/10.1175/1520-0442(1989)002<1229:ECSPFS>2.0.CO;2.

Arking, A., 1964: Latitudinal distribution of cloud cover from TIROS III photographs. *Science*, **143**, 569–571, https://doi.org/10.1126/science.143.3606.569.

——, and J. D. Childs, 1985: Retrieval of cloud cover parameters from multispectral satellite images. *J. Climate Appl. Meteor.*, **24**, 322–333, https://doi.org/10.1175/1520-0450(1985)024<0322:ROCCPF>2.0.CO;2.

Arndt, D. S., M. O. Baringer, and M. R. Johnson, Eds., 2010: State of the Climate in 2009. *Bull. Amer. Meteor. Soc.*, **91** (7), S1–S224, https://doi.org/10.1175/BAMS-91-7-StateoftheClimate.

Aumann, H. H., and Coauthors, 2003: AIRS/AMSU/HSB on the Aqua mission: Design, science objectives, data products and processing system. *IEEE Trans. Geosci. Remote Sens.*, **41**, 253–264, https://doi.org/10.1109/TGRS.2002.808356.

Austin, R. T., A. J. Heymsfield, and G. L. Stephens, 2009: Retrieval of ice cloud microphysical parameters using the CloudSat millimeter-wave radar and temperature. *J. Geophys. Res.*, **114**, D00A23, https://doi.org/10.1029/2008JD010049.

Baran, A. J., P. Hill, K. Furtado, P. Field, and J. Manners, 2014: A coupled cloud physics–radiation parameterization of the bulk optical properties of cirrus and its impact on the Met Office Unified Model Global Atmosphere 5.0 configuration. *J. Climate*, **27**, 7725–7752, https://doi.org/10.1175/JCLI-D-13-00700.1.

Barkstrom, B. R., 1984: The Earth Radiation Budget Experiment (ERBE). *Bull. Amer. Meteor. Soc.*, **65**, 1170–1185, https://doi.org/10.1175/1520-0477(1984)065<1170:TERBE>2.0.CO;2.

——, and G. L. Smith, 1986: The Earth Radiation Budget Experiment: Science and implementation. *Rev. Geophys.*, **24**, 379–390, https://doi.org/10.1029/RG024i002p00379.

Barrett, E. C., and D. W. Martin, 1981: *The Use of Satellite Data in Rainfall Monitoring*. Academic Press, 340 pp.

Battaglia, A., K. Mroz, T. Lang, F. Tridon, S. Tanelli, L. Tian, and G. M. Heymsfield, 2016a: Using a multiwavelength suite of microwave instruments to investigate the microphysical structure of deep convective cores. *J. Geophys. Res. Atmos.*, **121**, 9356–9381, https://doi.org/10.1002/2016JD025269.

——, ——, S. Tanelli, F. Tridon, and P.-E. Kirstetter, 2016b: Multiple-scattering-induced "ghost echoes" in GPM DPR observations of a tornadic supercell. *J. Appl. Meteor. Climatol.*, **55**, 1653–1666, https://doi.org/10.1175/JAMC-D-15-0136.1.

Baum, B. A., W. P. Menzel, R. A. Frey, D. C. Tobin, R. E. Holz, and S. A. Ackerman, 2012: MODIS cloud-top property refinements for collection 6. *J. Appl. Meteor. Climatol.*, **51**, https://doi.org/10.1175/JAMC-D-11-0203.1.

Bedka, K. M., and K. Khlopenkov, 2016: A probabilistic multispectral pattern recognition method for detection of overshooting cloud tops using passive satellite imager observations. *J. Appl. Meteor. Climatol.*, **55**, 1983–2005, https://doi.org/10.1175/JAMC-D-15-0249.1.

Bedka, K., E. Murillo, C. R. Homeyer, B. Scarino, and H. Mersiovsky, 2018: The above anvil cirrus plume: An important severe weather indicator in visible and infrared satellite imagery. *Wea. Forecasting*, **33**, 1159–1181, https://doi.org/10.1175/WAF-D-18-0040.1.

Beer, R., T. A. Glavich, and D. M. Rider, 2001: Tropospheric emission spectrometer for the Earth Observing System's Aura satellite. *Appl. Opt.*, **40**, 2356–2367, https://doi.org/10.1364/AO.40.002356.

Benjamin, S. G., and Coauthors, 2016: A North American hourly assimilation and model forecast cycle: The Rapid Refresh. *Mon. Wea. Rev.*, **144**, 1669–1694, https://doi.org/10.1175/MWR-D-15-0242.1.

——, J. M. Brown, G. Brunet, P. Lynch, K. Saito, and T. W. Schlatter, 2019: 100 years of progress in forecasting and NWP applications. *A Century of Progress in Atmospheric and Related Sciences: Celebrating the American Meteorological*

Society Centennial, *Meteor. Monogr.*, No. 59, Amer. Meteor. Soc., https://doi.org/10.1175/AMSMONOGRAPHS-D-18-0020.1.

Bennartz, R., 2007: Global assessment of marine boundary layer cloud droplet number concentration from satellite. *J. Geophys. Res.*, **112**, D02201, https://doi.org/10.1029/2006JD007547.

——, J. Fan, J. Rausch, L. R. Leung, and A. K. Heidinger, 2011: Pollution from China increases cloud droplet number, suppresses rain over the East China Sea. *Geophys. Res. Lett.*, **38**, L09704, https://doi.org/10.1029/2011GL047235.

Berg, W., and Coauthors, 2016: Intercalibration of the GPM microwave radiometer constellation. *J. Atmos. Oceanic Technol.*, **33**, 2639–2654, https://doi.org/10.1175/JTECH-D-16-0100.1.

Berndt, E. B., and M. Folmer, 2018: Utility of CrIS/ATMS profiles to diagnose extratropical transition. *Results Phys.*, **8**, 184–185, https://doi.org/10.1016/j.rinp.2017.12.006.

——, B. T. Zavodsky, and M. J. Folmer, 2016: Development and application of atmospheric infrared sounder ozone retrieval products for operational meteorology. *IEEE Trans. Geosci. Remote Sens.*, **54**, 958–967, https://doi.org/10.1109/TGRS.2015.2471259.

——, A. Molthan, W. W. Vaughan, and K. Fuell, 2017: Transforming satellite data into weather forecasts. *Eos, Trans. Amer. Geophys. Union*, **98**, https://doi.org/10.1029/2017EO064449.

Bhartia, P. K., D. F. Heath, and A. F. Fleig, 1985: Observation of anomalously small ozone densities in south polar stratosphere during October 1983 and 1984. *Symp. on Dynamics and Remote Sensing of the Middle Atmosphere*, Prague, Czechoslovakia, International Association of Geomagnetism and Aeronomy.

Blake, E. S., and R. J. Pasch, 2010: Eastern North Pacific hurricane season of 2008. *Mon. Wea. Rev.*, **138**, 705–721, https://doi.org/10.1175/2009MWR3093.1.

Bodas-Salcedo, A., and Coauthors, 2011: COSP: Satellite simulation software for model assessment. *Bull. Amer. Meteor. Soc.*, **92**, 1023–1043, https://doi.org/10.1175/2011BAMS2856.1.

——, P. G. Hill, K. Furtado, K. D. Williams, P. R. Field, J. C. Manners, P. Hyder, and S. Kato, 2016: Large contribution of supercooled liquid clouds to the solar radiation budget of the Southern Ocean. *J. Climate*, **29**, 4213–4228, https://doi.org/10.1175/JCLI-D-15-0564.1.

Bowman, K. P., J. C. Collier, G. R. North, Q. Wu, E. Ha, and J. Hardin, 2005: Diurnal cycle of tropical precipitation in Tropical Rainfall Measuring Mission (TRMM) satellite and ocean buoy rain gauge data. *J. Geophys. Res.*, **110**, D212204, https://doi.org/10.1029/2005JD005763.

Braun, S. A., 2010: Reevaluating the role of the Saharan air layer in Atlantic tropical cyclogenesis and evolution. *Mon. Wea. Rev.*, **138**, 2007–2037, https://doi.org/10.1175/2009MWR3135.1.

Bréon, F.-M., and S. Colzy, 2000: Global distribution of cloud droplet effective radius from POLDER polarization measurements. *Geophys. Res. Lett.*, **27**, 4065–4068, https://doi.org/10.1029/2000GL011691.

Brient, F., and T. Schneider, 2016: Constraints on climate sensitivity from space-based measurements of low-cloud reflection. *J. Climate*, **29**, 5821–5835, https://doi.org/10.1175/JCLI-D-15-0897.1.

Buriez, J.-C., and Coauthors, 1997: Cloud detection and derivation of cloud properties from POLDER. *Int. J. Remote Sens.*, **18**, 2785–2813, https://doi.org/10.1080/014311697217332.

Burrows, J. P., and Coauthors, 1999: The Global Ozone Monitoring Experiment (GOME): Mission concept and first scientific results. *J. Atmos. Sci.*, **56**, 151–175, https://doi.org/10.1175/1520-0469(1999)056<0151:TGOMEG>2.0.CO;2.

Callis, L. B., and M. Natarajan, 1986: The Antarctic ozone minimum: Relationship to odd nitrogen, odd chlorine, the final warming, and the 11-year solar cycle. *J. Geophys. Res.*, **91**, 10 771–10 796, https://doi.org/10.1029/JD091iD10p10771.

Cayla, F., and J. Pascale, 1995: IASI: Instrument overview. *Proc. SPIE*, **2553**, 316–328, https://doi.org/10.1117/12.221368.

Cecil, D. J., D. E. Buechler, and R. J. Blakeslee, 2014: Gridded lightning climatology from TRMM-LIS and OTD: Dataset description. *Atmos. Res.*, **135–136**, 404–414, https://doi.org/10.1016/j.atmosres.2012.06.028.

Cess, R. D., and G. L. Potter, 1988: A methodology for understanding and intercomparing atmospheric climate feedback processes in general circulation models. *J. Geophys. Res.*, **93**, 8305–8314, https://doi.org/10.1029/JD093iD07p08305.

Chahine, M. T., 1968: Determination of the temperature profile in an atmosphere from its outgoing radiance. *J. Opt. Soc. Amer.*, **58**, 1634–1637, https://doi.org/10.1364/JOSA.58.001634.

——, 1974: Remote sounding of cloudy atmospheres. I: The single cloud layer. *J. Atmos. Sci.*, **31**, 233–243, https://doi.org/10.1175/1520-0469(1974)031<0233:RSOCAI>2.0.CO;2.

——, and Coauthors, 2006: AIRS: Improving weather forecasting and providing new data on greenhouse gases. *Bull. Amer. Meteor. Soc.*, **87**, 911–926, https://doi.org/10.1175/BAMS-87-7-911.

Chakraborty, S., R. Fu, J. S. Wright, and S. T. Massie, 2015: Relationships between convective structure and transport of aerosols to the upper troposphere deduced from satellite observations. *J. Geophys. Res. Atmos.*, **120**, 6515–6536, https://doi.org/10.1002/2015JD023528.

Chand, D., R. Wood, T. L. Anderson, S. K. Satheesh, and R. J. Charlson, 2009: Satellite-derived direct radiative effect of aerosols dependent on cloud cover. *Nat. Geosci.*, **2**, 181–184, https://doi.org/10.1038/ngeo437.

——, and Coauthors, 2012: Aerosol optical depth increase in partly cloudy conditions. *J. Geophys. Res.*, **117**, D17207, https://doi.org/10.1029/2012JD017894.

Chen, G., W. Sha, and T. Iwasaki, 2009: Diurnal variation of precipitation over southeastern China: Spatial distribution and its seasonality. *J. Geophys. Res.*, **114**, D13103, https://doi.org/10.1029/2008JD011103.

Chen, P. Y., R. Srinivasan, G. Fedosejevs, and B. Narasimhan, 2002: An automated cloud detection method for daily NOAA-14 AVHRR data for Texas, USA. *Int. J. Remote Sens.*, **23**, 2939–2950, https://doi.org/10.1080/01431160110075631.

Chen, S. S., J. A. Knaff, and F. D. Marks Jr., 2006: Effects of vertical wind shear and storm motion on tropical cyclone rainfall asymmetries deduced from TRMM. *Mon. Wea. Rev.*, **134**, 3190–3208, https://doi.org/10.1175/MWR3245.1.

Chen, Y., H. Wang, J. Min, X.-Y. Huang, P. Minnis, R. Zhang, J. Haggerty, and R. Palikonda, 2015: Variational assimilation of cloud liquid/ice water path and its impact on NWP. *J. Appl. Meteor. Climatol*, **54**, 1809–1825, https://doi.org/10.1175/JAMC-D-14-0243.1.

——, R. Zhang, D. Meng, J. Min, and L. Zhang, 2016: Variational assimilation of satellite cloud water/ice path and microphysics scheme sensitivity to the assimilation of a rainfall case. *Adv. Atmos. Sci.*, **33**, 1158–1170, https://doi.org/10.1007/s00376-016-6004-3.

Cho, H.-M., and Coauthors, 2015: Frequency and causes of failed MODIS cloud property retrievals for liquid phase clouds over global oceans. *J. Geophys. Res. Atmos.*, 120, 4132–4154, https://doi.org/10.1002/2015JD023161.

Christian, H. J., R. J. Blakeslee, and S. J. Goodman, 1989: The detection of lightning from geostationary orbit. *J. Geophys. Res.*, **94**, 13 329–13 337, https://doi.org/10.1029/JD094iD11p13329.

Chu, D. A., Y. J. Kaufman, G. Zibordi, J. D. Chern, J. Mao, C. Li, and B. N. Holben, 2003: Global monitoring of air pollution over land from the Earth Observing System-Terra Moderate Resolution Imaging Spectroradiometer (MODIS). *J. Geophys. Res.*, **108**, 4661, https://doi.org/10.1029/2002JD003179.

Clarke, A. C., 1945: Extra-terrestrial relays: Can rocket stations give worldwide radio coverage? *Wireless World*, **51** (10), 305–308.

Clayson, C. A., and A. S. Bogdanoff, 2013: The effect of diurnal sea surface temperature warming on climatological air–sea fluxes. *J. Climate*, **26**, 2546–2556, https://doi.org/10.1175/JCLI-D-12-00062.1.

Coakley, J. A., Jr., and F. P. Bretherton, 1986: Cloud cover from high resolution scanner data: Detecting and allowing for partial field fields of view. *J. Atmos. Sci.*, **43**, 1025–1035, https://doi.org/10.1175/1520-0469(1986)043<1025:TEOCSO>2.0.CO;2.

Colle, B. A., A. R. Naeger, and A. Molthan, 2017: Structure and evolution of a warm frontal precipitation band during the GPM Cold Season Precipitation Experiment (GCPEx). *Mon. Wea. Rev.*, **145**, 473–493, https://doi.org/10.1175/MWR-D-16-0072.1.

Cox, S. K., and K. T. Griffith, 1979: Estimates of radiative divergence during Phase III of the GARP Atlantic Tropical Experiment: Part I. Methodology. *J. Atmos. Sci.*, **36**, 576–585, https://doi.org/10.1175/1520-0469(1979)036<0576:EORDDP>2.0.CO;2.

——, D. S. McDougal, D. A. Randall, and R. A. Schiffer, 1987: FIRE–The First ISCCP Regional Experiment. *Bull. Amer. Meteor. Soc.*, **68**, 114–118, https://doi.org/10.1175/1520-0477(1987)068<0114:FFIRE>2.0.CO;2.

Cucurull, L., 2010: Improvement in the use of an operational constellation of GPS radio occultation receivers in weather forecasting. *Wea. Forecasting*, **25**, 749–767, https://doi.org/10.1175/2009WAF2222302.1.

Dave, J. V., and C. L. Mateer, 1967: A preliminary study of the possibility of estimating the atmospheric ozone from satellite measurements. *J. Atmos. Sci.*, **24**, 414–427, https://doi.org/10.1175/1520-0469(1967)024<0414:APSOTP>2.0.CO;2.

Davies, R., V. M. Jovanovic, and C. M. Moroney, 2017: Cloud heights measured by MISR from 2000 to 2015. *J. Geophys. Res. Atmos.*, **122**, 3975–3986, https://doi.org/10.1002/2017JD026456.

Davis, G., 2007: History of the NOAA satellite program. *J. Appl. Remote Sens.*, **1**, 012504, https://doi.org/10.1117/1.2642347.

De Mazière, M., and Coauthors, 2018: The Network for the Detection of Atmospheric Composition Change (NDACC): History, status and perspectives. *Atmos. Chem. Phys.*, **18**, 4935–4964, https://doi.org/10.5194/acp-18-4935-2018.

Demuth, J. L., M. DeMaria, J. A. Knaff, and T. H. Vonder Haar, 2004: Evaluation of Advanced Microwave Sounding Unit tropical-cyclone intensity and size estimation algorithms. *J. Appl. Meteor.*, **43**, 282–296, https://doi.org/10.1175/1520-0450(2004)043<0282:EOAMSU>2.0.CO;2.

Deng, M., G. G. Mace, Z. Wang, and H. Okamoto, 2010: TC4 validation for cirrus cloud profiling retrieval using CloudSat radar and CALIPSO lidar. *J. Geophys. Res.*, **115**, D00J15, https://doi.org/10.1029/2009JD013104.

Derber, J. C., and W.-S. Wu, 1998: The use of TOVS cloud-cleared radiances in the NCEP SSI analysis system. *Mon. Wea. Rev.*, **126**, 2287–2302, https://doi.org/10.1175/1520-0493(1998)126<2287:TUOTCC>2.0.CO;2.

Derrien, M., B. Farki, L. Harang, H. LeGleau, A. Noyalet, D. Pochic, and A. Sairouni, 1993: Automatic cloud detection applied to NOAA-11 AVHRR imagery. *Remote Sens. Environ.*, **46**, 246–267, https://doi.org/10.1016/0034-4257(93)90046-Z.

Desbois, M., G. Séze, and G. Szejwach, 1982: Automatic classification of clouds on METEOSAT imagery: Application to high clouds. *J. Appl. Meteor.*, **21**, 401–412, https://doi.org/10.1175/1520-0450(1982)021<0401:ACOCOM>2.0.CO;2.

Deschamps, P. Y., F. M. Bréon, M. Leroy, A. Podaire, A. Bricaud, J. C. Buriez, and G. Séze, 1994: The POLDER Mission: Instrument characteristics and scientific objectives. *IEEE Trans. Geosci. Remote Sens.*, **32**, 598–615, https://doi.org/10.1109/36.297978.

Dessler, A. E., 2010: A determination of the cloud feedback from climate variations over the past decade. *Science*, **330**, 1523–1527, https://doi.org/10.1126/science.1192546.

——, and Coauthors, 1998: Selected science highlights from the first 5 years of the Upper Atmosphere Research Satellite (UARS) Program. *Rev. Geophys.*, **36**, 183–210, https://doi.org/10.1029/97RG03549.

Dieng, H. B., A. Cazenave, K. V. Schuckmann, M. Ablain, and B. Meyssignac, 2015: Sea level budget over 2005–2013: Missing contributions and data errors. *Ocean Sci.*, **11**, 789–802, https://doi.org/10.5194/os-11-789-2015.

Doelling, D. R., and Coauthors, 2013: Geostationary enhanced temporal interpolation for CERES flux products. *J. Atmos. Oceanic Technol.*, **30**, 1072–1090, https://doi.org/10.1175/JTECH-D-12-00136.1.

——, M. Sun, L. T. Nguyen, M. L. Nordeen, C. O. Haney, D. F. Keyes, and P. E. Mlynczak, 2016: Advances in geostationary-derived longwave fluxes for the CERES Synoptic (SYN1deg) product. *J. Atmos. Oceanic Technol.*, **33**, 503–521, https://doi.org/10.1175/JTECH-D-15-0147.1.

Dole, R. M., and Coauthors, 2018: Advancing science and services during the 2015/16 El Niño: The NOAA El Niño Rapid Response field campaign. *Bull. Amer. Meteor. Soc.*, **97**, 975–1001, https://doi.org/10.1175/BAMS-D-16-0219.1.

Dong, X., P. Minnis, B. Xi, S. Sun-Mack, and Y. Chen, 2008: Comparison of CERES-MODIS stratus cloud properties with ground-based measurements at the DOE ARM Southern Great Plains site. *J. Geophys. Res.*, **113**, D03204, https://doi.org/10.1029/2007JD008438.

——, B. Xi, S. Qiu, P. Minnis, S. Sun-Mack, and F. Rose, 2016: A radiation closure study of Arctic stratus cloud microphysical properties using the collocated satellite-surface data and Fu-Liou radiative transfer model. *J. Geophys. Res. Atmos.*, **121**, 10 175–10 198, https://doi.org/10.1002/2016JD025255.

Dowling, D. R., and L. F. Radke, 1990: A summary of the physical properties of cirrus clouds. *J. Appl. Meteor.*, **29**, 970–978, https://doi.org/10.1175/1520-0450(1990)029<0970:ASOTPP>2.0.CO;2.

Drummond, J. R., and G. S. Mand, 1996: The Measurements of Pollution in the Troposphere (MOPITT) instrument: Overall performance and calibration requirements. *J. Atmos. Oceanic Technol.*, **13**, 314–320, https://doi.org/10.1175/1520-0426(1996)013<0314:TMOPIT>2.0.CO;2.

Durran, D. R., 1986: Mountain waves. *Mesoscale Meteorology and Forecasting*, P. S. Ray, Ed., Amer. Meteor. Soc., 472–492.

Dvorak, V. F., 1975: Tropical cyclone intensity analysis and forecasting from satellite imagery. *Mon. Wea. Rev.*, **103**, 420–430, https://doi.org/10.1175/1520-0493(1975)103<0420:TCIAAF>2.0.CO;2.

——, 1984: Tropical cyclone intensity analysis using satellite data. NOAA Tech. Rep. NESDIS 11, 47 pp., http://satepsanone.nesdis.noaa.gov/pub/Publications/Tropical/Dvorak_1984.pdf.

Edwards, D. P., and Coauthors, 2004: Observations of carbon monoxide and aerosol from the Terra satellite: Northern Hemisphere variability. *J. Geophys. Res.*, **109**, D24202, https://doi.org/10.1029/2004JD004727.

Eguchi, K., I. Uno, K. Yumimoto, T. Takemura, A. Shimizu, N. Sugimoto, and Z. Liu, 2009: Trans-Pacific dust transport: Integrated analysis of NASA/CALIPSO and a global aerosol transport model. *Atmos. Chem. Phys.*, **9**, 3137–3145, https://doi.org/10.5194/acp-9-3137-2009.

Ellrod, G. P., 1985: Detection of high level turbulence using satellite imagery and upper air data. NOAA Tech. Memo. NESDIS 10, 30 pp.

Elsaesser, G. S., C. W. O'Dell, M. D. Lebsock, R. Bennartz, T. J. Greenwald, and F. J. Wentz, 2017: The Multisensor Advanced Climatology of Liquid Water Path (MAC-LWP). *J. Climate*, **30**, 10 193–10 210, https://doi.org/10.1175/JCLI-D-16-0902.1.

Emanuel, K., 2019: 100 years of progress in tropical cyclone research. *A Century of Progress in Atmospheric and Related Sciences: Celebrating the American Meteorological Society Centennial*, *Meteor. Monogr.*, No. 59, Amer. Meteor. Soc., https://doi.org/10.1175/AMSMONOGRAPHS-D-18-0016.1.

Engel-Cox, J. A., C. H. Holloman, B. W. Coutant, and R. M. Hoff, 2004: Qualitative and quantitative evaluation of MODIS satellite sensor data for regional and urban scale air quality. *Atmos. Environ.*, **38**, 2495–2509, https://doi.org/10.1016/j.atmosenv.2004.01.039.

Ernst, J. A., 1976: SMS-1 nighttime infrared imagery of low-level mountain waves. *Mon. Wea. Rev.*, **104**, 207–209, https://doi.org/10.1175/1520-0493(1976)104<0207:SNIIOL>2.0.CO;2.

Evan, A. T., D. J. Vimont, A. K. Heidinger, J. P. Kossin, and R. Bennartz, 2009: The role of aerosols in the evolution of tropical North Atlantic ocean temperature anomalies. *Science*, **324**, 778–781, https://doi.org/10.1126/science.1167404.

Evans, K. F., A. H. Evans, I. G. Nolt, and B. T. Marshall, 1999: The prospect for remote sensing of cirrus clouds with a submillimeter-wave spectrometer. *J. Appl. Meteor.*, **38**, 514–525, https://doi.org/10.1175/1520-0450(1999)038<0514:TPFRSO>2.0.CO;2.

Eyre, J. R., and A. Lorenc, 1989: Direct use of satellite sounding radiances in numerical weather prediction. *Meteor. Mag.*, **118**, 3–16.

Farman, J. C., B. G. Gardiner, and J. D. Shanklin, 1985: Large losses of total ozone in Antarctica reveal seasonal ClO_x/NO_x interaction. *Nature*, **315**, 207–210, https://doi.org/10.1038/315207a0.

Fauchez, T., P. Dubuisson, C. Cornet, F. Szczap, A. Garnier, J. Pelon, and K. Meyer, 2015: Impacts of cloud heterogeneities on cirrus optical properties retrieved from space-based thermal infrared radiometry. *Atmos. Meas. Tech.*, **8**, 633–647, https://doi.org/10.5194/amt-8-633-2015.

Feltz, M., R. Knuteson, S. A. Ackerman, and H. Revercomb, 2014: Application of GPS radio occultation to the assessment of temperature profile retrievals from microwave and infrared sounders. *Atmos. Meas. Tech.*, **7**, 3751–3762, https://doi.org/10.5194/amt-7-3751-2014.

Ferlay, N., and Coauthors, 2010: Toward new inferences about cloud structures from multidirectional measurements in the oxygen A band: Middle-of-cloud pressure and cloud geometrical thickness from POLDER-3/PARASOL. *J. Appl. Meteor. Climatol.*, **49**, 2492–2507, https://doi.org/10.1175/2010JAMC2550.1.

Ferraro, R. R., and Coauthors, 2005: NOAA operational hydrological products derived from the Advanced Microwave Sounding Unit. *IEEE Trans. Geosci. Remote Sens.*, **43**, 1036–1049, https://doi.org/10.1109/TGRS.2004.843249.

Fett, R. W., and R. G. Isaacs, 1979: Concerning causes of "anomalous gray shades" in DMSP visible imagery. *J. Appl. Meteor.*, **18**, 1340–1351, https://doi.org/10.1175/1520-0450(1979)018<1340:CCOGSI>2.0.CO;2.

Field, P. R., and A. J. Heymsfield, 2015: Importance of snow to global precipitation. *Geophys. Res. Lett.*, **42**, 9512–9520, https://doi.org/10.1002/2015GL065497.

Field, R. D., and Coauthors, 2015: Development of a global fire weather database. *Nat. Hazards Earth Syst. Sci.*, **15**, 1407–1423, https://doi.org/10.5194/nhess-15-1407-2015.

Fischer, J., R. Preusker, and L. Schüller, 1997: ATBD cloud top pressure. European Space Agency Algorithm Theoretical Basis Doc. PO-TN-MEL-GS-0006, 28 pp.

Fishman, J., and W. Seiler, 1983: Correlative nature of ozone and carbon monoxide in the troposphere: Implications for the tropospheric ozone budget. *J. Geophys. Res.*, **88**, 3662–3670, https://doi.org/10.1029/JC088iC06p03662.

Foster, M. J., and A. Heidinger, 2013: PATMOS-x: Results from a diurnally corrected 30-yr satellite cloud climatology. *J. Climate*, **26**, 414–425, https://doi.org/10.1175/JCLI-D-11-00666.1.

——, and Coauthors, 2017:Cloudiness [in "State of the Climate in 2016"]. *Bull. Amer. Meteor. Soc.*, **98** (8), S27–S28, https://doi.org/10.1175/2017BAMSStateoftheClimate.1.

Frey, R. A., S. A. Ackerman, and B. J. Soden, 1996: Climate parameters from satellite spectral measurements. Part I: Collocated AVHRR and HIRS/2 observations of spectral greenhouse parameter. *J. Climate*, **9**, 327–344, https://doi.org/10.1175/1520-0442(1996)009<0327:CPFSSM>2.0.CO;2.

——, ——, Y. Liu, K. I. Strabala, H. Zhang, J. R. Key, and X. Wang, 2008: Cloud detection with MODIS. Part I: Improvements in the MODIS cloud mask for collection 5. *J. Atmos. Oceanic Technol.*, **25**, 1057–1072, https://doi.org/10.1175/2008JTECHA1052.1.

Frierson, D. M. W., and Coauthors, 2013: Contribution of ocean overturning circulation to tropical rainfall peak in the Northern Hemisphere. *Nat. Geosci.*, **6**, 940–944, https://doi.org/10.1038/ngeo1987.

Fritz, S., 1965: The significance of mountain lee waves as seen from satellite pictures. *J. Appl. Meteor.*, **4**, 31–37, https://doi.org/10.1175/1520-0450(1965)004<0031:TSOMLW>2.0.CO;2.

Fu, Q., and K. N. Liou, 1993: Parameterization of the radiative properties of cirrus clouds. *J. Atmos. Sci.*, **50**, 2008–2025, https://doi.org/10.1175/1520-0469(1993)050<2008:POTRPO>2.0.CO;2.

——, G. Lesins, J. Higgins, T. Charlock, P. Chylek, and J. Michalsky, 1998: Broadband water vapor absorption of solar radiation tested using ARM data. *Geophys. Res. Lett.*, **25**, 1169–1172, https://doi.org/10.1029/98GL00846.

Gambacorta, A., and C. D. Barnet, 2013: Methodology and information content of the NOAA NESDIS operational channel selection for the Cross-track Infrared Sounder (CrIS). *IEEE Trans. Geosci. Remote Sens.*, **51**, 3207–3216, https://doi.org/10.1109/TGRS.2012.2220369.

——, and ——, 2018: Atmospheric soundings from hyperspectral satellite observations. *Comprehensive Remote Sensing*, Vol. 7, Elsevier, 64–96, https://doi.org/10.1016/B978-0-12-409548-9.10384-7.

Geer, A. J., and Coauthors, 2017: The growing impact of satellite observations sensitive to humidity, cloud and precipitation. *Quart. J. Roy. Meteor. Soc.*, **143**, 3189–3206, https://doi.org/10.1002/qj.3172.

Gelaro, R., R. H. Langland, S. Pellerin, and R. Todling, 2010: The THORPEX Observation Impact Intercomparison Experiment. *Mon. Wea. Rev.*, **138**, 4009–4025, https://doi.org/10.1175/2010MWR3393.1.

Gettelman, A., H. Morrison, S. Santos, P. Bogenschutz, and P. M. Caldwell, 2015: Advanced two-moment bulk microphysics for global models. Part II: Global model solutions and aerosol-cloud interactions. *J. Climate*, **28**, 1288–1307, https://doi.org/10.1175/JCLI-D-14-00103.1.

Glumb, R. J., D. C. Jordan, and P. Mantica, 2002: Development of the Crosstrack Infrared Sounder (CrIS) sensor design. *Proc. SPIE*, **4486**, 411–424, https://doi.org/10.1117/12.455124.

Goldberg, M. D., Y. Qu, L. M. McMillin, W. W. Wolf, L. Zhou, and M. Divakarla, 2003: AIRS near-real-time products and algorithms in support of operational weather prediction. *IEEE Trans. Geosci. Remote Sens.*, **41**, 379–389, https://doi.org/10.1109/TGRS.2002.808307.

Goloub, P., M. Herman, H. Chepfer, J. Riedi, G. Brogniez, P. Couvert, and G. Seze, 2000: Cloud thermodynamical phase classification from the POLDER spaceborne instrument. *J. Geol. Res.*, **105**, 14 747–14 759, https://doi.org/10.1029/1999JD901183.

Gong, J., and D. L. Wu, 2017: Microphysical properties of frozen particles inferred from Global Precipitation Measurement (GPM) Microwave Imager (GMI) polarimetric measurements. *Atmos. Chem. Phys.*, **17**, 2741–2757, https://doi.org/10.5194/acp-17-2741-2017.

Goodman, S. J., and Coauthors, 2013: The GOES-R Geostationary Lightning Mapper (GLM). *Atmos. Res.*, **125–126**, 34–49, https://doi.org/10.1016/j.atmosres.2013.01.006.

——, T. J. Schmit, J. Daniels, W. Denig, and K. Metcalf, 2018: GOES: Past, present and future. *Comprehensive Remote Sensing*, Vol. 1, Elsevier, 119–149, https://doi.org/10.1016/B978-0-12-409548-9.10315-X.

Gravelle, C. M., J. R. Mecikalski, W. E. Line, K. M. Bedka, R. A. Petersen, J. M. Sieglaff, G. T. Stano, and S. J. Goodman, 2016: Demonstration of a GOES-R satellite convective toolkit to "bridge the gap" between severe weather watches and warnings: An example from the 20 May 2013 Moore, Oklahoma, tornado outbreak. *Bull. Amer. Meteor. Soc.*, **97**, 69–84, https://doi.org/10.1175/BAMS-D-14-00054.1.

Greenwald, T. J., 2009: A 2 year comparison of AMSR-E and MODIS cloud liquid water path observations. *Geophys. Res. Lett.*, **36**, L20805, https://doi.org/10.1029/2009GL040394.

——, G. L. Stephens, T. H. Vonder Haar, and D. L. Jackson, 1993: A physical retrieval of cloud liquid water over the global oceans using Special Sensor Microwave/Imager (SSM/I) observations. *J. Geophys. Res.*, **98**, 18 471–18 488, https://doi.org/10.1029/93JD00339.

Griffith, C. G., W. L. Woodley, P. G. Grube, D. W. Martin, J. Stout, and D. N. Sidkar, 1978: Rain estimates from geosynchronous satellite imagery: Visible and infrared studies. *Mon. Wea. Rev.*, **106**, 1153–1171, https://doi.org/10.1175/1520-0493(1978)106<1153:REFGSI>2.0.CO;2.

Grund, C. J., and E. Eloranta, 1991: University of Wisconsin High Spectral Resolution Lidar. *Opt. Eng.*, **30**, 6, https://doi.org/10.1117/12.55766.

Guo, H., J.-C. Golaz, L. J. Donner, P. Ginoux, and R. S. Hemler, 2014: Multivariate probability density functions with dynamics in the GFDL atmospheric general circulation model: Global tests. *J. Climate*, **27**, 2087–2108, https://doi.org/10.1175/JCLI-D-13-00347.1.

Hagos, S., Z. Feng, C. D. Burleyson, K.-S. S. Lim, C. N. Long, D. Wu, and G. Thompson, 2014: Evaluation of convection-permitting model simulations of cloud populations associated with the Madden-Julian Oscillation using data collected during the AMIE/DYNAMO field campaign. *J. Geophys. Res. Atmos.*, **119**, 12 052–12 068, https://doi.org/10.1002/2014JD022143.

Hamada, A., and Y. N. Takayabu, 2016: Improvements in detection of light precipitation with the Global Precipitation Measurement Dual-Frequency Precipitation Radar (GPM DPR). *J. Atmos. Oceanic Technol.*, **33**, 653–667, https://doi.org/10.1175/JTECH-D-15-0097.1.

Han, Q., W. B. Rossow, and A. A. Lacis, 1994: Near-global survey of effective droplet radii in liquid water clouds using ISCCP data. *J. Climate*, **7**, 465–497, https://doi.org/10.1175/1520-0442(1994)007<0465:NGSOED>2.0.CO;2.

Hand, L. M., and J. M. Shepherd, 2009: An investigation of warm season spatial rainfall variability in Oklahoma City: Possible linkage to urbanization and prevailing wind. *J. Appl. Meteor. Climatol.*, **48**, 251–269, https://doi.org/10.1175/2008JAMC2036.1.

Hanel, R., and B. Conrath, 1969: Interferometer experiment on Nimbus 3: Preliminary results. *Science*, **165**, 1258–1260, https://doi.org/10.1126/science.165.3899.1258.

Harries, J. E., and Coauthors, 2005: The Geostationary Earth Radiation Budget project. *Bull. Amer. Meteor. Soc.*, **86**, 945–960, https://doi.org/10.1175/BAMS-86-7-945.

Harrison, E. F., D. R. Brooks, P. Minnis, B. A. Wielicki, W. F. Staylor, G. G. Gibson, D. F. Young, and F. M. Denn, 1988: First estimates of the diurnal variation of longwave radiation from the multiple-satellite Earth Radiation Budget Experiment (ERBE). *Bull. Amer. Meteor. Soc.*, **69**, 1144–1151, https://doi.org/10.1175/1520-0477(1988)069<1144:FEOTDV>2.0.CO;2.

——, P. Minnis, B. R. Barkstrom, V. Ramanathan, R. D. Cess, and G. G. Gibson, 1990: Seasonal variation of cloud radiative forcing derived from the Earth Radiation Budget Experiment. *J. Geophys. Res.*, **95**, 18 687–18 703, https://doi.org/10.1029/JD095iD11p18687.

Hartmann, D. L., and P. Ceppi, 2014: Trends in the CERES dataset, 2000–13: The effects of sea ice and jet shifts and comparison to climate models. *J. Climate*, **27**, 2444–2456, https://doi.org/10.1175/JCLI-D-13-00411.1.

Hasler, A. F., 1981: Stereographic observations from geosynchronous satellites: An important new tool for the atmospheric sciences. *Bull. Amer. Meteor. Soc.*, **62**, 194–212, https://doi.org/10.1175/1520-0477(1981)062<0194:SOFGSA>2.0.CO;2.

Healy, S. B., A. M. Jupp, and C. Marquardt, 2005: Forecast impact experiment with GPS radio occultation measurements. *Geophys. Res. Lett.*, **32**, L03804, https://doi.org/10.1029/2004GL020806.

Heidinger, A. K., M. J. Foster, A. Walther, and X. Zhao, 2014: The Pathfinder Atmospheres–Extended AVHRR climate dataset. *Bull. Amer. Meteor. Soc.*, **95**, 909–922, https://doi.org/10.1175/BAMS-D-12-00246.1.

——, Y. Li, B. A. Baum, R. E. Holz, S. Platnick, and P. Yang, 2015: Retrieval of cirrus cloud optical depth under day and night conditions from MODIS Collection 6 Cloud property data. *Remote Sens.*, **7**, 7257–7271, https://doi.org/10.3390/rs70607257.

Henson, R., 2010: *Weather on the Air: A History of Broadcast Meteorology*. Amer. Meteor. Soc., 241 pp.

Herman, J. R., P. K. Bhartia, O. Torres, C. Hsu, C. Seftor, and E. Celarier, 1997: Global distribution of UV-absorbing aerosols from Nimbus7/TOMS data. *J. Geophys. Res.*, **102**, 16 911–16 922, https://doi.org/10.1029/96JD03680.

Herwehe, J. A., K. Alapaty, T. L. Spero, and C. G. Nolte, 2014: Increasing the credibility of regional climate simulations by introducing subgrid-scale cloud-radiation interactions. *J. Geophys. Res. Atmos.*, **119**, 5317–5330, https://doi.org/10.1002/2014JD021504.

Heymsfield, G. M., and R. H. Blackmer Jr., 1988: Satellite observed characteristics of Midwest severe thunderstorm anvils. *Mon. Wea. Rev.*, **116**, 2200–2224, https://doi.org/10.1175/1520-0493(1988)116<2200:SOCOMS>2.0.CO;2.

——, ——., and S. Schotz, 1983: Upper-level structure of Oklahoma tornadic storms on 2 May 1979. I: Radar and satellite observations. *J. Atmos. Sci.*, **40**, 1740–1755, https://doi.org/10.1175/1520-0469(1983)040<1740:ULSOOT>2.0.CO;2.

Hill, P. G., R. P. Allan, J. C. Chiu, and T. H. M. Stein, 2016: A multisatellite climatology of clouds, radiation, and precipitation in southern West Africa and comparison to climate models. *J. Geophys. Res. Atmos.*, **121**, 10 857–10 879, https://doi.org/10.1002/2016JD025246.

Hilton, F., and Coauthors, 2012: Hyperspectral Earth observation from IASI: Five years of accomplishments. *Bull. Amer. Meteor. Soc.*, **93**, 347–370, https://doi.org/10.1175/BAMS-D-11-00027.1.

Hirose, M., R. Oki, S. Shimizu, M. Kachi, and T. Higashiuwatoko, 2008: Finescale diurnal rainfall statistics refined from eight years of TRMM PR data. *J. Appl. Meteor. Climatol.*, **47**, 544–561, https://doi.org/10.1175/2007JAMC1559.1.

Holben, B. N., and Coauthors, 2001: An emerging ground-based aerosol climatology: Aerosol optical depth from AERONET. *J. Geophys. Res.*, **106**, 12 067–12 097, https://doi.org/10.1029/2001JD900014.

Holz, R., S. Ackerman, P. Antonelli, F. Nagle, R. O. Knuteson, M. McGill, D. L. Hlavka, and W. D. Hart, 2006: An improvement to the high spectral resolution CO_2-slicing cloud-top altitude retrieval. *J. Atmos. Oceanic Technol.*, **23**, 653–670, https://doi.org/10.1175/JTECH1877.1.

Holz, R. E., S. A. Ackerman, F. W. Nagle, R. Frey, S. Dutcher, R. E. Kuehn, M. A. Vaughan, and B. Baum, 2008: Global Moderate Resolution Imaging Spectroradiometer (MODIS) cloud detection and height evaluation using CALIOP. *J. Geophys. Res.*, **113**, D00A19, https://doi.org/10.1029/2008JD009837.

——, and Coauthors, 2016: Resolving cirrus optical depth biases between CALIOP and MODIS using IR retrievals. *Atmos. Chem. Phys.*, **16**, 5075–2016, https://doi.org/10.5194/acp-16-5075-2016.

Hong, G., G. Heygster, J. Miao, and K. Kunzi, 2005: Detection of tropical deep convective clouds from AMSU-B water vapor channels measurements. *J. Geophys. Res.*, **110**, D05205, https://doi.org/10.1029/2004JD004949.

Horváth, Á., and R. Davies, 2007: Comparison of microwave and optical cloud water path estimates from TMI, MODIS, and MISR. *J. Geophys. Res.*, **112**, D01202, https://doi.org/10.1029/2006JD007101.

——, and C. Gentemann, 2007: Cloud-fraction-dependent bias in satellite liquid water path retrievals of shallow, non-precipitating marine clouds. *Geophys. Res. Lett.*, **34**, https://doi.org/10.1029/2007GL030625.

Hou, A. Y., and Coauthors, 2014: The Global Precipitation Measurements Mission. *Bull. Amer. Meteor. Soc.*, **95**, 701–722, https://doi.org/10.1175/BAMS-D-13-00164.1.

House, F. B., A. Gruber, G. E. Hunt, and A. T. Mecherikunnel, 1986: History of satellite missions and measurements of the Earth Radiation Budget (1957–1984). *Rev. Geophys.*, **24**, 357–377, https://doi.org/10.1029/RG024i002p00357.

Houze, R. A., Jr., 2019: 100 years of research on mesoscale convective systems. *A Century of Progress in Atmospheric and Related Sciences: Celebrating the American Meteorological Society Centennial*, *Meteor. Monogr.*, No. 59, Amer. Meteor. Soc., https://doi.org/10.1175/AMSMONOGRAPHS-D-18-0001.1.

Hsu, N. C., J. R. Herman, J. F. Gleason, O. Torres, and C. J. Seftor, 1999: Satellite detection of smoke aerosols over a snow/ice surface by TOMS. *Geophys. Res. Lett.*, **26**, 1165–1168, https://doi.org/10.1029/1999GL900155.

——, R. Gautam, A. M. Sayer, C. Bettenhausen, C. Li, M. J. Jeong, S.-C. Tsay, and B. N. Holben, 2012: Global and regional trends of aerosol optical depth over land and ocean using SeaWiFS measurements from 1997 to 2010. *Atmos. Chem. Phys.*, **12**, 8037–8053, https://doi.org/10.5194/acp-12-8037-2012.

——, M.-J. Jeong, C. Bettenhausen, A. M. Sayer, R. Hansell, C. S. Seftor, J. Huang, and S.-C. Tsay, 2013: Enhanced Deep Blue aerosol retrieval algorithm: The second generation. *J. Geophys. Res. Atmos.*, **118**, 9296–9315, https://doi.org/10.1002/jgrd.50712.

Hu, Y., and Coauthos, 2009: CALIPSO/CALIOP cloud phase discrimination algorithm. *J. Atmos. Oceanic Technol.*, **26**, 2293–2309, https://doi.org/10.1175/2009JTECHA1280.1.

Huang, J., P. Minnis, B. Chen, Z. Huang, Z. Liu, Q. Zhao, Y. Yi, and J. K. Ayers, 2008: Long-range transport and vertical structure of Asian dust from CALIPSO and surface measurements during PACDEX. *J. Geophys. Res.*, **113**, L23212, https://doi.org/10.1029/2008JD010620.

——, J. Liu, B. Chen, and S. L. Nasiri, 2015: Detection of anthropogenic dust using CALIPSO lidar measurements. *Atmos. Chem. Phys.*, **15**, 11 653–11 665, https://doi.org/10.5194/acp-15-11653-2015.

Hubert, L. F., and L. F. Whitney Jr., 1971: Wind estimation from geostationary-satellite pictures. *Mon. Wea. Rev.*, **99**, 665–672, https://doi.org/10.1175/1520-0493(1971)099<0665:WEFGP>2.3.CO;2.

Huffman, G. J., and Coauthors, 2007: The TRMM Multisatellite Precipitation Analysis (TMPA): Quasi-global, multiyear, combined-sensor precipitation estimates at fine scale. *J. Hydrometeor.*, **8**, 38–55, https://doi.org/10.1175/JHM560.1.

——, and Coauthors, 2017: NASA Global Precipitation Measurement (GPM) Integrated Multi-satellitE Retrievals for GPM (IMERG). Algorithm Theoretical Basis Doc., version 4.6, 28 pp., https://pmm.nasa.gov/sites/default/files/document_files/IMERG_ATBD_V4.6.pdf.

Husar, R. B., J. M. Prospero, and L. L. Stowe, 1997: Characterization of tropospheric aerosols over the oceans with the NOAA advanced very high resolution radiometer optical thickness operational product. *J. Geophys. Res.*, **102**, 16 889–16 909, https://doi.org/10.1029/96JD04009.

Iguchi, T., and Coauthors, 2014: WRF–SBM simulations of melting-layer structure in mixed-phase: Precipitation events observed during LPVEx. *J. Appl. Meteor. Climatol.*, **53**, 2710–2731, https://doi.org/10.1175/JAMC-D-13-0334.1.

Illingworth, A. J., and Coauthors, 2015: The EarthCARE satellite: The next step forward in global measurements of clouds, aerosols, precipitation, and radiation. *Bull. Amer. Meteor. Soc.*, **96**, 1311–1332, https://doi.org/10.1175/BAMS-D-12-00227.1.

Iturbide-Sanchez, F., S. R. S. da Silva, Q. Liu, K. L. Pryor, M. E. Pettey, and N. R. Nalli, 2018: Toward the operational weather forecasting application of atmospheric stability products derived from NUCAPS CrIS/ATMS Soundings. *IEEE Trans. Geosci. Remote Sens.*, **56**, 4522–4545, https://doi.org/10.1109/TGRS.2018.2824829.

Jackson, B., S. E. Nicholson, and D. Klotter, 2009: Mesoscale convective systems over western equatorial Africa and their relationship to large-scale circulation. *Mon. Wea. Rev.*, **137**, 1272–1294, https://doi.org/10.1175/2008MWR2525.1.

Jacobowitz, H., L. L. Stowe, G. Ohring, A. Heidinger, K. Knapp, and N. R. Nalli, 2003: The advanced very high resolution radiometer Pathfinder Atmosphere (PATMOS) climate dataset: A resource for climate research. *Bull. Amer. Meteor. Soc.*, **84**, 785–793, https://doi.org/10.1175/BAMS-84-6-785.

Janowiak, J. E., P. A. Arkin, P. Xie, M. L. Morrissey, and D. R. Legates, 1995: An examination of the east Pacific ITCZ rainfall distribution. *J. Climate*, **8**, 2810–2823, https://doi.org/10.1175/1520-0442(1995)008<2810:AEOTEP>2.0.CO;2.

Jethva, H. T., O. Torres, L. Remer, and P. K. Bhartia, 2013: A color ratio method for simultaneous retrieval of aerosol and cloud optical thickness of above-cloud absorbing aerosols from passive sensors: Application to MODIS measurements. *IEEE Trans. Geosci. Remote Sens.*, **51**, 3862–3870, https://doi.org/10.1109/TGRS.2012.2230008.

Johnson, G. C., J. M. Lyman, and N. G. Loeb, 2016: Improving estimates of Earth's energy imbalance. *Nat. Climate Change*, **6**, 639–640, https://doi.org/10.1038/nclimate3043.

Jones, T. A., and D. J. Stensrud, 2012: Assimilating AIRS temperature and mixing ratio profiles using an ensemble Kalman filter approach for convective-scale forecasts. *Wea. Forecasting*, **27**, 541–564, https://doi.org/10.1175/WAF-D-11-00090.1.

——, K. Knopfmeier, D. Wheatley, G. Creager, P. Minnis, and R. Palikonda, 2016: Storm-scale data assimilation and ensemble forecasting with the NSSL experimental Warn- on-Forecast system. Part II: Combined radar and satellite data experiments. *Wea. Forecasting*, **31**, 297–327, https://doi.org/10.1175/WAF-D-15-0107.1.

Kaplan, L. D., 1959: Inferences of atmospheric structures from satellite remote radiation measurements. *J. Opt. Soc. Amer.*, **49**, 1004–1014, https://doi.org/10.1364/JOSA.49.001004.

Karlsson, K.-G., 1989: Development of an operational cloud classification model. *Int. J. Remote Sens.*, **10**, 687–693, https://doi.org/10.1080/01431168908903910.

Kato, S., T. P. Ackerman, J. H. Mather, and E. E. Clothiaux, 1999: The k-distribution method and correlated-k approximation for a shortwave radiative transfer model. *J. Quant. Spectrosc. Radiat. Transfer*, **62**, 109–121, https://doi.org/10.1016/S0022-4073(98)00075-2.

——, F. G. Rose, and T. P. Charlock, 2005: Computation of domain-averaged irradiance using satellite-derived cloud properties. *J. Atmos. Oceanic Technol.*, **22**, 146–164, https://doi.org/10.1175/JTECH-1694.1.

——, N. G. Loeb, D. A. Rutan, F. G. Rose, S. Sun-Mack, W. F. Miller, and Y. Chen, 2012: Uncertainty estimate of surface irradiances computed with MODIS-, CALIPSO-, and CloudSat-derived cloud and aerosol properties. *Surv. Geophys.*, **33**, 395–412, https://doi.org/10.1007/s10712-012-9179-x.

——, ——, F. G. Rose, D. R. Doelling, D. A. Rutan, T. E. Caldwell, L. Yu, and R. A. Weller, 2013: Surface irradiances consistent with CERES-derived top-of-atmosphere shortwave and longwave irradiances. *J. Climate*, **26**, 2719–2740, https://doi.org/10.1175/JCLI-D-12-00436.1.

——, and Coauthors, 2018: Surface irradiances of Edition 4.0 Clouds and the Earth's Radiant Energy System (CERES) Energy Balanced and Filled (EBAF) data product. *J. Climate*, **31**, 4501–4527, https://doi.org/10.1175/JCLI-D-17-0523.1.

Kaufman, Y. J., D. Tanre, L. A. Remer, E. F. Vermote, A. Chu, and B. N. Holben, 1997: Operational remote sensing of tropospheric aerosol over land from EOS moderate resolution imaging spectroradiometer. *J. Geophys. Res.*, **102**, 17 051–17 067, https://doi.org/10.1029/96JD03988.

Kaye, J. A., and T. L. Miller, 1996: The ATLAS series of Shuttle missions. *Geophys. Res. Lett.*, **23**, 2285–2288, https://doi.org/10.1029/96GL02228.

Khan, R., R. Anwar, S. Akanda, M. D. McDonald, A. Huq, A. Jutla, and R. Colwell, 2017: Assessment of risk of cholera in Haiti following Hurricane Matthew. *Amer. J. Trop. Med. Hyg.*, **97**, 896–903, https://doi.org/10.4269/ajtmh.17-0048.

Kidder, S. Q., and T. H. Vonder Haar, 1990: On the use of satellites in Molniya orbits for meteorological observation of middle and high latitudes. *J. Atmos. Oceanic Technol.*, **7**, 517–522, https://doi.org/10.1175/1520-0426(1990)007<0517:OTUOSI>2.0.CO;2.

——, W. M. Gray, and T. H. Vonder Haar, 1978: Estimating tropical cyclone central pressure and outer winds from satellite microwave data. *Mon. Wea. Rev.*, **106**, 1458–1464, https://doi.org/10.1175/1520-0493(1978)106<1458:ETCCPA>2.0.CO;2.

——, ——, and ——, 1980: Tropical cyclone outer surface winds derived from satellite microwave sounder data. *Mon. Wea. Rev.*, **108**, 144–152, https://doi.org/10.1175/1520-0493(1980)108<0144:TCOSWD>2.0.CO;2.

Kimberlain, T. B., and M. J. Brennan, 2011: Eastern North Pacific hurricane season of 2009. *Mon. Wea. Rev.*, **139**, 1657–1672, https://doi.org/10.1175/2010MWR3497.1.

King, J. I. F., 1958: The radiative heat transfer of planet earth. *Scientific Uses of Earth Satellites*, J. A. van Allen, Ed., University of Michigan Press, 133–136.

King, M. D., and S. Platnick, 2018: The Earth Observing System (EOS). *Comprehensive Remote Sensing*, Vol. 1, Elsevier, 7–26, https://doi.org/10.1016/B978-0-12-409548-9.10312-4.

——, and Coauthors, 2003: Cloud and aerosol properties, precipitable water, and profiles of temperature and humidity. *IEEE Trans. Geosci. Remote Sens.*, **41**, 442–458, https://doi.org/10.1109/TGRS.2002.808226.

——, S. Platnick, W. P. Menzel, S. A. Ackerman, and P. A. Hubanks, 2013: Spatial and temporal distribution of clouds observed by MODIS onboard the Terra and Aqua satellites. *IEEE Trans. Geosci. Remote Sens.*, **51**, 3826–3852, https://doi.org/10.1109/TGRS.2012.2227333.

Kirschbaum, D. B., and Coauthors, 2017: NASA's remotely-sensed precipitation: A reservoir for applications users. *Bull. Amer. Meteor. Soc.*, **98**, 1169–1184, https://doi.org/10.1175/BAMS-D-15-00296.1.

Kirstetter, P.-E., Y. Hong, J. J. Gourley, M. Schwaller, W. Petersen, and Q. Cao, 2015: Impact of sub-pixel rainfall variability on spaceborne precipitation estimation: Evaluating the TRMM 2A25 product. *Quart. J. Roy. Meteor. Soc.*, **141**, 953–966, https://doi.org/10.1002/qj.2416.

Knox, J. A., A. S. Bachmeier, W. M. Carter, J. E. Tarantino, L. C. Paulik, E. N. Wilson, G. S. Bechdol, and M. J. Mays, 2010: Transverse cirrus bands in weather systems: A grand tour of an enduring enigma. *Weather*, **65**, 35–41, https://doi.org/10.1002/wea.417.

Koelemeijer, R. B. A., P. Stammes, J. W. Hovenier, and J. F. de Haan, 2001: A fast method for retrieval of cloud parameters using oxygen A band measurements from the Global Ozone Monitoring Experiment. *J. Geophys. Res.*, **106**, 3475–3490, https://doi.org/10.1029/2000JD900657.

Kokhanovsky, A. A., V. V. Rozanov, J. P. Burrows, K.-U. Eichmann, W. Lotz, and M. Vountas, 2005: The SCIAMACHY cloud products: Algorithms and examples from ENVISAT. *Adv. Space Res.*, **36**, 789–799, https://doi.org/10.1016/j.asr.2005.03.026.

Kopia, L. P., 1986: Earth Radiation Budget Experiment scanner instrument. *Rev. Geophys.*, **24**, 400–406, https://doi.org/10.1029/RG024i002p00400.

Kopp, G., and J. L. Lean, 2011: A new, lower value of total solar irradiance: Evidence and climate significance. *Geophys. Res. Lett.*, **38**, L01706, https://doi.org/10.1029/2010GL045777.

Kratz, D. P., and F. G. Rose, 1999: Accounting for molecular absorption within the spectral range of the CERES window channel. *J. Quant. Spectrosc. Radiat. Transfer*, **61**, 83–95, https://doi.org/10.1016/S0022-4073(97)00203-3.

Kriebel, K. T., R. W. Saunders, and G. Gesell, 1989: Optical properties of clouds derived from fully cloudy AVHRR pixels. *Beitr. Phys. Atmos.*, **62**, 165–171.

Kubota, I., and H. Imai, 1986: Land-sea contrast in the earth radiation budget. *J. Meteor. Soc. Japan*, **64**, 871–879, https://doi.org/10.2151/jmsj1965.64.6_871.

Kumar, S. V., and Coauthors, 2006: Land Information System: An interoperable framework for high resolution land surface modelling. *Environ. Modell. Software*, **21**, 1402–1415, https://doi.org/10.1016/j.envsoft.2005.07.004.

Kummerow, C., W. Barnes, T. Kozu, J. Shiue, and J. Simpson, 1998: The Tropical Rainfall Measuring Mission (TRMM) sensor package. *J. Atmos. Oceanic Technol.*, **15**, 809–817, https://doi.org/10.1175/1520-0426(1998)015<0809:TTRMMT>2.0.CO;2.

——, and Coauthors, 2000: The status of the Tropical Rainfall Measuring Mission (TRMM) after two years in orbit. *J. Appl. Meteor.*, **39**, 1965–1982, https://doi.org/10.1175/1520-0450(2001)040<1965:TSOTTR>2.0.CO;2.

Kuo, K.-S., and Coauthors, 2016: The microwave radiative properties of falling snow derived from nonspherical ice particle models. Part I: An extensive database of simulated pristine crystals and aggregate particles, and their scattering properties. *J. Appl. Meteor. Climatol.*, **55**, 691–708, https://doi.org/10.1175/JAMC-D-15-0130.1.

Kuo, Y.-H., T.-K. Wee, S. Sokolovskiy, C. Rocken, W. Schreiner, D. Hunt, and R. A. Anthes, 2004: Inversion and error estimation of GPS radio occultation data. *J. Meteor. Soc. Japan*, **82**, 507–531, https://doi.org/10.2151/jmsj.2004.507.

Kursinski, E. R., G. A. Hajj, J. T. Schofield, R. P. Linfield, and K. R. Hardy, 1997: Observing Earth's atmosphere with radio occultation measurements using the Global Positioning System. *J. Geophys. Res.*, **102**, 23 429–23 465, https://doi.org/10.1029/97JD01569.

——, ——, S. S. Leroy, and B. Herman, 2000: The GPS radio occultation technique. *Terr. Atmos. Ocean. Sci.*, **11**, 53–114, https://doi.org/10.3319/TAO.2000.11.1.53(COSMIC).

L'Ecuyer, T. S., 2017: Earth's energy balance. *International Encyclopedia of Geography: People, the Earth, Environment, and Technology*, D. Richardson et al., Eds., John Wiley and Sons, 1–7, https://doi.org/10.1002/9781118786352.wbieg1132.

——, and J. H. Jiang, 2010: Touring the atmosphere aboard the A-Train. *Phys. Today*, **63**, 36–41, https://doi.org/10.1063/1.3463626.

——, H. Masunaga, and C. D. Kummerow, 2006: Variability in the characteristics of precipitation systems in the tropical pacific. Part II: Implications for atmospheric heating. *J. Climate*, **19**, 1388–1406, https://doi.org/10.1175/JCLI3698.1.

——, N. B. Wood, T. Haladay, G. L. Stephens, and P. W. Stackhouse Jr., 2008: Impact of clouds on atmospheric heating based on the R04 CloudSat fluxes and heating rates data set. *J. Geophys. Res.*, **113**, D00A15, https://doi.org/10.1029/2008JD009951.

——, and Coauthors, 2015: The observed state of the energy budget in the early twenty-first century. *J. Climate*, **28**, 8319–8346, https://doi.org/10.1175/JCLI-D-14-00556.1.

Labonnote, L. C., G. Brogniez, J.-C. Buriez, M. Doutriaux-Boucher, J. Gayet, and A. Macke, 2001: Polarized light scattering by inhomogeneous hexagonal monocrystals: Validation with ADEOS-POLDER measurements. *J. Geophys. Res.*, **106**, 12 139–12 154, https://doi.org/10.1029/2000JD900642.

Lamarque, J.-F., and Coauthors, 2003: Identification of CO plumes from MOPITT data: Application to the August 2000 Idaho-Montana forest fires. *Geophys. Res. Lett.*, **30**, 1688, https://doi.org/10.1029/2003GL017503.

Lau, K., and H. Wu, 2010: Characteristics of precipitation, cloud, and latent heating associated with the Madden–Julian oscillation. *J. Climate*, **23**, 504–518, https://doi.org/10.1175/2009JCLI2920.1.

Le Marshall, J., and Coauthors, 2006: Improving global analysis and forecasting with AIRS. *Bull. Amer. Meteor. Soc.*, **87**, 891–895, https://doi.org/10.1175/BAMS-87-7-891.

Lenz, A., K. M. Bedka, W. F. Feltz, and S. A. Ackerman, 2009: Convectively induced transverse band signatures in satellite images. *Wea. Forecasting*, **24**, 1362–1373, https://doi.org/10.1175/2009WAF2222285.1.

Levy, R. C., S. Mattoo, L. A. Munchak, L. A. Remer, A. M. Sayer, F. Patadia, and N. C. Hsu, 2013: The Collection 6 MODIS aerosol products over land and ocean. *Atmos. Meas. Tech.*, **6**, 2989–3034, https://doi.org/10.5194/amt-6-2989-2013.

Lewis, J. M., J. Phillips, W. P. Menzel, T. H. Vonder Haar, H. Moosmuller, F. B. House, and M. G. Fearon, 2018: *Verner Suomi: The Life and Work of the Founder of Satellite Meteorology*. Amer Meteor. Soc., 168 pp.

Li, J.-L., and Coauthors, 2005: Comparisons of EOS MLS cloud ice measurements with ECMWF analyses and GCM simulations: Initial results. *Geophys. Res. Lett.*, **32**, L18710, https://doi.org/10.1029/2005GL023788.

Libertino, A., A. Sharma, V. Kalshmi, and P. Claps, 2016: A global assessment of the timing of extreme rainfall from TRMM and GPM for improving hydrologic design. *Environ. Res. Lett.*, **11**, 054003, https://doi.org/10.1088/1748-9326/11/5/054003.

Lim, K.-S. S., and Coauthors, 2014: Investigation of aerosol indirect effects using a cumulus microphysics parameterization in a regional climate model. *J. Geophys. Res. Atmos.*, **119**, 906–926, https://doi.org/10.1002/2013JD020958.

Lin, L. F., A. M. Ebtehaj, R. L. Bras, A. N. Flores, and J. Wang, 2015: Dynamical precipitation downscaling for hydrologic applications using WRF 4D-Var data assimilation: Implications for GPM era. *J. Hydrometeor.*, **16**, 811–829, https://doi.org/10.1175/JHM-D-14-0042.1.

Liu, C., 2011: Rainfall contributions from precipitation systems with different sizes, convective intensities and durations over the tropics and subtropics. *J. Hydrometeor.*, **12**, 394–412, https://doi.org/10.1175/2010JHM1320.1.

——, and E. J. Zipser, 2005: Global distribution of convection penetrating the tropical tropopause. *J. Geophys. Res.*, **110**, D23104, https://doi.org/10.1029/2005JD006063.

——, and ——, 2015: The global distribution of largest, deepest, and most intense precipitation systems. *Geophys. Res. Lett.*, **42**, 3591–3595, https://doi.org/10.1002/2015GL063776.

——, ——, and S. W. Nesbitt, 2007: Global distribution of tropical deep convection: Different perspectives from TRMM infrared and radar data. *J. Climate*, **20**, 489–503, https://doi.org/10.1175/JCLI4023.1.

Liu, G., and J. A. Curry, 1993: Determination of characteristic features of cloud liquid water from satellite microwave measurements. *J. Geophys. Res.*, **98**, 5069–5092, https://doi.org/10.1029/92JD02888.

Liu, N., and C. Liu, 2016: Global distribution of deep convection reaching tropopause in 1 year GPM observations. *J. Geophys. Res. Atmos.*, **121**, 3824–3842, https://doi.org/10.1002/2015JD024430.

Llovel, W., J. K. Willis, F. W. Landerer, and I. Fukumori, 2014: Deep-ocean contribution to sea level and energy budget not detectable over the past decade. *Nat. Climate Change*, **4**, 1031–1035, https://doi.org/10.1038/nclimate2387.

Loeb, N. G., N. Manalo-Smith, S. Kato, W. F. Miller, S. K. Gupta, P. Minnis, and B. A. Wielicki, 2003a: Angular distribution models for top-of-atmosphere radiative flux estimation from the Clouds and the Earth's Radiant Energy System instrument on the Tropical Rainfall Measuring Mission Satellite. Part I: Methodology. *J. Appl. Meteor.*, **42**, 240–265, https://doi.org/10.1175/1520-0450(2003)042<0240:ADMFTO>2.0.CO;2.

——, K. Loukachine, N. Manalo-Smith, B. A. Wielicki, and D. F. Young, 2003b: Angular distribution models for top-of-atmosphere radiative flux estimation from the Clouds and the Earth's Radiant Energy System instrument on the Tropical Rainfall Measuring Mission Satellite. Part II: Validation. *J. Appl. Meteor.*, **42**, 1748–1769, https://doi.org/10.1175/1520-0450(2003)042<1748:ADMFTR>2.0.CO;2.

——, S. Kato, K. Loukachine, and N. Manalo-Smith, 2005: Angular distribution models for top-of-atmosphere radiative flux estimation from the Clouds and the Earth's Radiant Energy System instrument on the *Terra* satellite. Part I: Methodology. *J. Atmos. Oceanic Technol.*, **22**, 338–351, https://doi.org/10.1175/JTECH1712.1.

——, B. A. Wielicki, D. R. Doelling, G. L. Smith, D. F. Keyes, S. Kato, N. Manalo-Smith, and T. Wong, 2009: Toward optimal closure of the Earth's top-of-atmosphere radiation budget. *J. Climate*, **22**, 748–766, https://doi.org/10.1175/2008JCLI2637.1.

——, J. M. Lyman, G. C. Johnson, R. P. Allan, D. R. Doelling, T. Wong, B. J. Soden, and G. L. Stephens, 2012: Observed changes in top-of-the-atmosphere radiation and upper-ocean heating consistent within uncertainty. *Nat. Geosci.*, **5**, 110–113, https://doi.org/10.1038/ngeo1375.

——, H. Wang, A. Cheng, S. Kato, J. T. Fasullo, K.-M. Xu, and R. P. Allan, 2016a: Observational constraints on atmospheric and oceanic cross-equatorial heat transports: Revisiting the precipitation asymmetry problem in climate models. *Climate Dyn.*, **46**, 3239–3257, https://doi.org/10.1007/s00382-015-2766-z.

——, N. Manalo-Smith, W. Su, M. Shankar, and S. Thomas, 2016b: CERES top-of-atmosphere Earth radiation budget climate data record: Accounting for in-orbit changes in instrument calibration. *Remote Sens.*, **8**, 182, https://doi.org/10.3390/rs8030182.

——, W. Su, D. R. Doelling, T. Wong, P. Minnis, S. Thomas, and W. F. Miller, 2018: Earth's top-of-atmosphere radiation budget. *Comprehensive Remote Sensing*, Vol. 5, Elsevier, 67–84, https://doi.org/10.1016/B978-0-12-409548-9.10367-7.

Lonfat, M., F. D. Marks Jr., and S. S. Chen, 2004: Precipitation distribution in tropical cyclones using the Tropical Rainfall Measuring Mission (TRMM) microwave imager: A global perspective. *Mon. Wea. Rev.*, **132**, 1645–1660, https://doi.org/10.1175/1520-0493(2004)132<1645:PDITCU>2.0.CO;2.

Luntama, J.-P., and Coauthors, 2008: Prospects of the EPS GRAS mission for operational atmospheric applications. *Bull. Amer. Meteor. Soc.*, **89**, 1863–1875, https://doi.org/10.1175/2008BAMS2399.1.

Luther, M. R., J. E. Cooper, and G. R. Taylor, 1986: The Earth Radiation Budget Experiment non-scanning instrument. *Rev. Geophys.*, **24**, 391–399, https://doi.org/10.1029/RG024i002p00391.

Mace, G. G., and Q. Zhang, 2014: The CloudSat radar-lidar geometrical profile product (RL-GeoProf): Updates, improvements, and selected results. *J. Geophys. Res. Atmos.*, **119**, 9441–9462, https://doi.org/10.1002/2013JD021374.

——, Y. Zhang, S. Platnick, M. D. King, and P. Yang, 2005: Evaluation of cirrus cloud properties derived from MODIS radiances using cloud properties derived from ground-based data collected at the ARM SGP site. *J. Appl. Meteor.*, **44**, 221–240, https://doi.org/10.1175/JAM2193.1.

——, Q. Zhang, M. Vaughan, R. Marchand, G. Stephens, C. Trepte, and D. Winker, 2009: A description of hydrometeor layer occurrence statistics derived from the first year of merged Cloudsat and CALIPSO data. *J. Geophys. Res.*, **114**, D00A26, https://doi.org/10.1029/2007JD009755.

Maddox, R. A., 1980: Mesoscale convective complexes. *Bull. Amer. Meteor. Soc.*, **61**, 1374–1387, https://doi.org/10.1175/1520-0477(1980)061<1374:MCC>2.0.CO;2.

Maggioni, V., M. R. P. Sapiano, R. F. Adler, Y. Tian, and G. J. Huffman, 2014: An error model for uncertainty quantification in high-time-resolution precipitation products. *J. Hydrometeor.*, **15**, 1274–1292, https://doi.org/10.1175/JHM-D-13-0112.1.

Marchant, B., S. Platnick, K. Meyer, G. T. Arnold, and J. Riedi, 2016: MODIS Collection 6 shortwave-derived cloud phase classification algorithm and comparisons with CALIOP. *Atmos. Meas. Tech.*, **9**, 1587–1599, https://doi.org/10.5194/amt-9-1587-2016.

Marshak, A., and Coauthors, 2018: Earth Observations from DSCOVR EPIC Instrument. *Bull. Amer. Meteor. Soc.*, **99**, 1829–1850, https://doi.org/10.1175/BAMS-D-17-0223.1.

Marshall, J., A. Donohoe, D. Ferreira, and D. McGee, 2014: The ocean's role in setting the mean position of the inter-tropical convergence zone. *Climate Dyn.*, **42**, 1967–1979, https://doi.org/10.1007/s00382-013-1767-z.

Martin, R. V., A. M. Fiore, and A. Van Donkelaar, 2004: Space-based diagnosis of surface ozone sensitivity to anthropogenic emissions. *Geophys. Res. Lett.*, **31**, L06120, https://doi.org/10.1029/2004GL019416.

Marvel, K., M. Zelinka, S. A. Klein, C. Bonfils, P. Caldwell, C. Doutriaux, B. D. Santer, and K. E. Taylor, 2015: External influences on modeled and observed cloud trends. *J. Climate*, **28**, 4820–4840, https://doi.org/10.1175/JCLI-D-14-00734.1.

Masaki, T., and Coauthors, 2015: Current status of GPM/DPR level 1 algorithm development and DPR calibration. *2015 IEEE Int. Geoscience and Remote Sensing Symp.*, Milan, Italy, IEEE, 2615–2618, https://doi.org/10.1109/IGARSS.2015.7326348.

Mateer, C. L., D. F. Heath, and A. J. Krueger, 1971: Estimation of total ozone from satellite measurements of backscattered ultraviolet earth radiance. *J. Atmos. Sci.*, **28**, 1307–1311, https://doi.org/10.1175/1520-0469(1971)028<1307:EOTOFS>2.0.CO;2.

Matus, A., and T. S. L'Ecuyer, 2017: The role of cloud phase in Earth's radiation budget. *J. Geophys. Res. Atmos.*, **122**, 2559–2578, https://doi.org/10.1002/2016JD025951.

——, ——, J. E. Kay, J.-F. Lamarque, and C. Hannay, 2015: The role of clouds in modulating global aerosol direct radiative effects in spaceborne active observations and the Community Earth System Model. *J. Climate*, **28**, 2986–3003, https://doi.org/10.1175/JCLI-D-14-00426.1.

McCann, D. W., 1983: The enhanced-V: A satellite observable severe storm signature. *Mon. Wea. Rev.*, **111**, 887–894, https://doi.org/10.1175/1520-0493(1983)111<0887:TEVASO>2.0.CO;2.

McCormick, M. P., 1987: SAGE II: An overview. *Adv. Space Res.*, **7**, 219–226, https://doi.org/10.1016/0273-1177(87)90151-7.

——, 1993: Scientific investigations planned for the Lidar In-space Technology Experiment (LITE). *Bull. Amer. Meteor. Soc.*, **74**, 205–214, https://doi.org/10.1175/1520-0477(1993)074<0205:SIPFTL>2.0.CO;2.

——, and R. E. Veiga, 1992: SAGE II measurements of early Pinatubo aerosols. *Geophys. Res. Lett.*, **19**, 155–158, https://doi.org/10.1029/91GL02790.

——, ——, and W. P. Chu, 1992: Stratospheric ozone profile and total ozone trends derived from the SAGE I and SAGE II data. *Geophys. Res. Lett.*, **19**, 269–272, https://doi.org/10.1029/92GL00187.

McNally, A. P., and M. Vesperini, 1996: Variational analysis of humidity information from TOVS. *Quart. J. Roy. Meteor. Soc.*, **122**, 1521–1544, https://doi.org/10.1002/qj.49712253504.

Mecikalski, J. R., and Coauthors, 2007: Aviation applications for satellite-based observations of cloud properties, convective initiation, in-flight icing, turbulence and volcanic ash. *Bull. Amer. Meteor. Soc.*, **88**, 1589–1607, https://doi.org/10.1175/BAMS-88-10-1589.

Menzel, W. P., and J. F. W. Purdom, 1994: Introducing GOES-I: The first of a new generation of Geostationary Operational Environmental Satellites. *Bull. Amer. Meteor. Soc.*, **75**, 757–781, https://doi.org/10.1175/1520-0477(1994)075<0757:IGITFO>2.0.CO;2.

——, W. L. Smith, and T. R. Stewart, 1983: Improved cloud motion wind vector and altitude assignment using VAS. *J. Climate Appl. Meteor.*, **22**, 377–384, https://doi.org/10.1175/1520-0450(1983)022<0377:ICMWVA>2.0.CO;2.

Meyer, K., S. Platnick, and Z. Zhang, 2015: Simultaneously inferring above-cloud absorbing aerosol optical thickness and underlying liquid phase cloud optical and microphysical properties using MODIS. *J. Geophys. Res. Atmos.*, **120**, 5524–5547, https://doi.org/10.1002/2015JD023128.

Miller, D. J., Z. Zhang, A. S. Ackerman, S. Platnick, and B. A. Baum, 2016: The impact of cloud vertical structure on cloud liquid water path retrieval based on the bispectral solar reflection method: A theoretical study based on large-eddy simulations of shallow marine boundary-layer clouds. *J. Geophys. Res. Atmos.*, **121**, 4122–4141, https://doi.org/10.1002/2015JD024322.

Minnis, P., and E. F. Harrison, 1984a: Diurnal variability of the regional cloud and clear-sky radiative parameters derived from GOES data. Part I: Analysis method. *J. Climate Appl. Meteor.*, **23**, 993–1011, https://doi.org/10.1175/1520-0450(1984)023<0993:DVORCA>2.0.CO;2.

——, and ——, 1984b: Diurnal variability of regional cloud and clear-sky radiative parameters derived from GOES data. Part III: November 1978 radiative parameters. *J. Climate Appl. Meteor.*, **23**, 1032–1052, https://doi.org/10.1175/1520-0450(1984)023<1032:DVORCA>2.0.CO;2.

——, ——, L. L. Stowe, G. G. Gibson, F. M. Denn, D. R. Doelling, and W. L. Smith Jr., 1993: Radiative climate forcing by the Mt. Pinatubo eruption. *Science*, **259**, 1411–1415, https://doi.org/10.1126/science.259.5100.1411.

——, and Coauthors, 2008: Cloud detection in non-polar regions for CERES using TRMM VIRS and Terra and Aqua MODIS data. *IEEE Trans. Geosci. Remote Sens.*, **46**, 3857–3884, https://doi.org/10.1109/TGRS.2008.2001351.

——, and Coauthors, 2011a: CERES Edition-2 cloud property retrievals using TRMM VIRS and Terra and Aqua MODIS data—Part I: Algorithms. *IEEE Trans. Geosci. Remote Sens.*, **49**, 4374–4400, https://doi.org/10.1109/TGRS.2011.2144601.

——, and Coauthors, 2011b: CERES Edition-2 cloud property retrievals using TRMM VIRS and Terra and Aqua MODIS data—Part II: Examples of average results and comparisons with other data. *IEEE Trans. Geosci. Remote Sens.*, **49**, 4401–4430, https://doi.org/10.1109/TGRS.2011.2158492.

Minzner, R. A., W. E. Shenk, J. Steranka, and R. D. Teagle, 1976: Cloud heights determined stereographically from imagery recorded simultaneously by two synchronous meteorological satellites, SMS-1 and SMS-2. *Eos, Trans. Amer. Geophys. Union*, **57**, 593.

Munchak, S. J., and G. Skofronick-Jackson, 2013: Evaluation of precipitation detection over various surfaces from passive microwave imagers and sounders. *Atmos. Res.*, **131**, 81–94, https://doi.org/10.1016/j.atmosres.2012.10.011.

Nakajima, T., and M. D. King, 1990: Determinations of the optical thickness and effective particle radius of clouds from reflected solar radiation measurements. Part I: Theory. *J. Atmos. Sci.*, **47**, 1878–1893, https://doi.org/10.1175/1520-0469(1990)047<1878:DOTOTA>2.0.CO;2.

Nalli, N. R., and Coauthors, 2013: Validation of satellite sounder environmental data records: Application to the Cross-track Infrared Microwave Sounder Suite. *J. Geophys. Res. Atmos.*, **118**, 13 628–13 643, https://doi.org/10.1002/2013JD020436.

——, and Coauthors, 2016: Satellite sounder observations of contrasting tropospheric moisture transport regimes: Saharan air layers, Hadley cells, and atmospheric rivers. *J. Hydrometeor.*, **17**, 2997–3006, https://doi.org/10.1175/JHM-D-16-0163.1.

——, and Coauthors, 2018a: Validation of atmospheric profile retrievals from the SNPP NOAA-Unique Combined Atmospheric Processing System. Part 1: Temperature and moisture. *IEEE Trans. Geosci. Remote Sens.*, **56**, 180–190, https://doi.org/10.1109/TGRS.2017.2744558.

——, and Coauthors, 2018b: Validation of atmospheric profile retrievals from the SNPP NOAA-Unique Combined Atmospheric Processing System. Part 2: Ozone. *IEEE Trans. Geosci. Remote Sens.*, **56**, 598–607, https://doi.org/10.1109/TGRS.2017.2762600.

NASA, 2014: The Nimbus Program History. Doc. NP-2004-10-188-GSFC, 34 pp., https://atmospheres.gsfc.nasa.gov/uploads/files/Nimbus_History.pdf.

NASEM, 2015: *Continuity of NASA Earth Observations from Space: A Value Framework*. National Academies Press, 118 pp., https://doi.org/10.17226/21789.

——, 2016: *Achieving Science with CubeSats: Thinking Inside the Box*. National Academies Press, 130 pp., https://doi.org/10.17226/23503.

——, 2018: *Thriving on Our Changing Planet: A Decadal Strategy for Earth Observation from Space*. National Academies Press, 716 pp., https://doi.org/10.17226/24938.

Negri, A. J., 1982: Cloud-top structure of tornadic storms on 10 April 1979 from rapid scan and stereo satellite observations. *Bull. Amer. Meteor. Soc.*, **63**, 1151–1159, https://doi.org/10.1175/1520-0477-63.10.1151.

Nesbitt, S. W., and E. J. Zipser, 2003: The diurnal cycle of rainfall and convective intensity according to three years of TRMM measurements. *J. Climate*, **16**, 1456–1475, https://doi.org/10.1175/1520-0442-16.10.1456.

Njoku, E., T. J. Jackson, V. Lakshmi, T. K. Chan, and S. V. Nghiem, 2003: Soil moisture retrieval from AMSR-E. *IEEE Trans. Geosci. Remote Sens.*, **41**, 215–229, https://doi.org/10.1109/TGRS.2002.808243.

Norris, J. R., and A. T. Evan, 2015: Empirical removal of artifacts from the ISCCP and PATMOS-x satellite cloud records. *J. Atmos. Oceanic Technol.*, **32**, 691–702, https://doi.org/10.1175/JTECH-D-14-00058.1.

O'Dell, C. W., F. J. Wentz, and R. Bennartz, 2008: Cloud liquid water path from satellite-based passive microwave observations: A new climatology over the global oceans. *J. Climate*, **21**, 1721–1739, https://doi.org/10.1175/2007JCLI1958.1.

Ohring, G., B. A. Wielicki, R. Spencer, B. Emery, and R. Datla, 2005: Satellite instrument calibration for measuring global climate change: Report of a workshop. *Bull. Amer. Meteor. Soc.*, **86**, 1303–1313, https://doi.org/10.1175/BAMS-86-9-1303.

Olander, T. L., and C. S. Velden, 2007: The Advanced Dvorak Technique: Continued development of an objective scheme to estimate tropical cyclone intensity using geostationary infrared satellite data. *Wea. Forecasting*, **22**, 287–298, https://doi.org/10.1175/WAF975.1.

Olson, W. S., and Coauthors, 2006: Precipitation and latent heating distributions from satellite passive microwave radiometry. Part I: Improved method and uncertainties. *J. Appl. Meteor. Climatol.*, **45**, 702–720, https://doi.org/10.1175/JAM2369.1.

——, and Coauthors, 2016: The microwave radiative properties of falling snow derived from nonspherical ice particle models. Part II: Initial testing using radar, radiometer and in situ observations. *J. Appl. Meteor. Climatol.*, **55**, 709–722, https://doi.org/10.1175/JAMC-D-15-0131.1.

Oreopoulos, L., N. Cho, and D. Lee, 2017: New insights about cloud vertical structure from CloudSat and CALIPSO observations. *J. Geophys. Res. Atmos.*, **122**, 9280–9300, https://doi.org/10.1002/2017JD026629.

Painemal, D., P. Minnis, J. K. Ayers, and L. O'Neill, 2012: GOES-10 microphysical retrievals in marine warm clouds: Multi-instrument validation and daytime cycle over the southeast Pacific. *J. Geophys. Res.*, **117**, D19212, https://doi.org/10.1029/2012JD017822.

——, ——, and S. Sun-Mack, 2013: The impact of horizontal heterogeneities, cloud fraction, and cloud dynamics on warm cloud effective radii and liquid water path from CERES-like Aqua MODIS retrievals. *Atmos. Chem. Phys.*, **13**, 9997–10 003, https://doi.org/10.5194/acp-13-9997-2013.

——, S. Kato, and P. Minnis, 2014: Boundary layer regulation in the southeast Atlantic cloud microphysics during the biomass burning season as seen by the A-train satellite constellation. *J. Geophys. Res. Atmos.*, **119**, 11 288–11 302, https://doi.org/10.1002/2014JD022182.

——, T. Greenwald, M. Cadeddu, and P. Minnis, 2016: First extended validation of satellite microwave liquid water path with ship-based observations of marine low clouds. *Geophys. Res. Lett.*, **43**, 6563–6570, https://doi.org/10.1002/2016GL069061.

Pan, W., O. Branch, and B. Zaitchik, 2014: Impact of climate change on vector-borne disease in the Amazon. *Global Climate Change and Public Health*, K. Pinkerton and W. Rom, Eds., Respiratory Medicine, Vol. **7**, Humana Press, 193–210, https://doi.org/10.1007/978-1-4614-8417-2_11.

Park, S., C. S. Bretherton, and P. J. Rasch, 2014: Integrating cloud processes in the Community Atmosphere Model, version 5. *J. Climate*, **27**, 6821–6856, https://doi.org/10.1175/JCLI-D-14-00087.1.

Pavolonis, M. J., A. K. Heidinger, and J. Sieglaff, 2013: Automated retrievals of volcanic ash and dust cloud properties from upwelling infrared measurements. *J. Geophys. Res. Atmos.*, **118**, 1436–1458, https://doi.org/10.1002/jgrd.50173.

Peters-Lidard, C. D., F. Hossain, L. R. Leung, N. McDowell, M. Rodell, F. J. Tapiador, F. J. Turk, and A. Wood, 2019: 100 years of progress in hydrology. *A Century of Progress in Atmospheric and Related Sciences: Celebrating the American Meteorological Society Centennial*, *Meteor. Monogr.*, No. 59, Amer. Meteor. Soc., https://doi.org/10.1175/AMSMONOGRAPHS-D-18-0019.1.

Petersen, W. A., H. J. Christian, and S. A. Rutledge, 2005: TRMM observations of the global relationship between ice water content and lightning. *Geophys. Res. Lett.*, **32**, L14819, https://doi.org/10.1029/2005GL023236.

——, R. Fu, M. Chen, and R. Blakeslee, 2006: Intraseasonal forcing of convection and lightning activity in the southern Amazon as a function of cross-equatorial flow. *J. Climate*, **19**, 3180–3196, https://doi.org/10.1175/JCLI3788.1.

——, R. A. Houze, L. McMurdie, J. Zagrodnik, S. Tanelli, J. Lundquist, and J. Wurmann, 2016: The Olympic Mountains Experiment: From ocean to summit. *Meteorological Technology International*, September issue, UKi Media and Events, Dorking, United Kingdom, 22—26, https://www.ukimediaevents.com/pub-meteorological.php.

Petkovic, V., and C. D. Kummerow, 2015: Performance of the GPM passive microwave retrieval in the Balkan flood event of 2014. *J. Hydrometeor.*, **16**, 2501–2518, https://doi.org/10.1175/JHM-D-15-0018.1.

Phulpin, T., M. Derrien, and A. Brard, 1983: A two-dimensional histogram procedure to analyze cloud cover from NOAA satellite high-resolution imagery. *J. Climate Appl. Meteor.*, **22**, 1332–1345, https://doi.org/10.1175/1520-0450(1983)022<1332:ATDHPT>2.0.CO;2.

Pierce, R. B., and Coauthors, 2003: Regional Air Quality Modeling System (RAQMS) predictions of the tropospheric ozone budget over east Asia. *J. Geophys. Res.*, **108**, 8825, https://doi.org/10.1029/2002JD003176.

——, and Coauthors, 2007: Chemical data assimilation estimates of continental U.S. ozone and nitrogen budgets during the Intercontinental Chemical Transport Experiment–North America. *J. Geophys. Res.*, **112**, D12S21, https://doi.org/10.1029/2006JD007722.

Pilewskie, P., and S. Twomey, 1987: Discrimination of ice from water in clouds by optical remote sensing. *Atmos. Res.*, **21**, 113–122, https://doi.org/10.1016/0169-8095(87)90002-0.

Pincus, R., S. Platnick, S. A. Ackerman, R. S. Hemler, and R. J. Hofmann, 2012: Reconciling simulated and observed views of clouds: MODIS, ISCCP, and the limits of instrument simulators. *J. Climate*, **25**, 4699–4720, https://doi.org/10.1175/JCLI-D-11-00267.1.

Pistone, K., I. Eisenman, and V. Ramanathan, 2014: Observational determination of albedo decrease caused by vanishing Arctic sea ice. *Proc. Natl. Acad. Sci. USA*, **111**, 3322–3326, https://doi.org/10.1073/pnas.1318201111.

Platnick, S., and S. Twomey, 1994: Determining the susceptibility of cloud albedo to changes in droplet concentrations with the Advanced Very High Resolution Radiometer. *J. Appl. Meteor.*, **33**, 334–347, https://doi.org/10.1175/1520-0450(1994)033<0334:DTSOCA>2.0.CO;2.

——, M. D. King, S. A. Ackerman, W. P. Menzel, B. A. Baum, J. C. Riedi, and R. A. Frey, 2003: The MODIS cloud products: Algorithms and examples from Terra. *IEEE Trans. Geosci. Remote Sens.*, **41**, 459–473, https://doi.org/10.1109/TGRS.2002.808301.

——, and Coauthors, 2017: The MODIS cloud optical and microphysical products: Collection 6 updates and examples from Terra and Aqua. *IEEE Trans. Geosci. Remote Sens.*, **55**, 502–525, https://doi.org/10.1109/TGRS.2016.2610522.

Poole, L. R., and M. P. McCormick, 1990: Major results from SAGE II. *The Role of the Stratosphere in Global Change*, M. L. Chanin, Ed., NATO ASI Series, Vol. 8, Springer, 377–386, https://doi.org/10.1007/978-3-642-78306-7_18.

Poulsen, C. A., and Coauthors, 2012: Cloud retrievals from satellite data using optimal estimation: evaluation and application to ATSR. *Atmos. Meas. Tech.*, **5**, 1889–1910, https://doi.org/10.5194/amt-5-1889-2012.

Prospero, J. M., E. Bonatti, C. Schubert, and T. N. Carlson, 1970: Dust in the Caribbean atmosphere traced to an African dust storm. *Earth Planet. Sci. Lett.*, **9**, 287–293, https://doi.org/10.1016/0012-821X(70)90039-7.

Purdom, J. F. W., 1976: Some uses of high resolution GOES imagery in the mesoscale forecasting of convection and its behavior. *Mon. Wea. Rev.*, **104**, 1474–1483, https://doi.org/10.1175/1520-0493(1976)104<1474:SUOHRG>2.0.CO;2.

——, and W. P. Menzel, 1996: Evolution of satellite observations in the United States and their use in meteorology. *Historical Essays on Meteorology 1919–1995*, J. R. Fleming, Ed., Amer. Meteor. Soc., 99–155, https://doi.org/10.1007/978-1-940033-84-6_5.

Rajapakshe, C., Z. Zhang, J. E. Yorks, H. Yu, Q. Tan, K. Meyer, S. Platnick, and D. M. Winker, 2017: Seasonally transported aerosol layers over southeast Atlantic are closer to underlying clouds than previously reported. *Geophys. Res. Lett.*, **44**, 5818–5825, https://doi.org/10.1002/2017GL073559.

Ramanathan, V., R. D. Cess, E. F. Harrison, P. Minnis, B. R. Barkstrom, E. Ahmed, and D. Hartmann, 1989: Cloud-radiative forcing and climate: Results from the Earth radiation Budget Experiment. *Science*, **243**, 57–63, https://doi.org/10.1126/science.243.4887.57.

Rappaport, E. N., and Coauthors, 2009: Advances and challenges at the National Hurricane Center. *Wea. Forecasting*, **24**, 395–419, https://doi.org/10.1175/2008WAF2222128.1.

Raschke, E., and W. R. Bandeen, 1970: The radiation balance of the planet earth from radiations measurements of the satellite Nimbus II. *J. Climate Appl. Meteor.*, **9**, 215–238, https://doi.org/10.1175/1520-0450(1970)009<0215:TRBOTP>2.0.CO;2.

——, T. H. Vonder Haar, W. R. Bandeen, and M. Pasternak, 1973: The annual radiation budget of the Earth-atmosphere system during 1969–70 from Nimbus 3 measurements. *J. Atmos. Sci.*, **30**, 341–364, https://doi.org/10.1175/1520-0469(1973)030<0341:TARBOT>2.0.CO;2.

Rausch, J., A. Heidinger, and R. Bennartz, 2010: Regional assessment of microphysical properties of marine boundary layer cloud using the PATMOS-x dataset. *J. Geophys. Res.*, **115**, D23212, https://doi.org/10.1029/2010JD014468.

Rawlins, F., and J. S. Foot, 1990: Remotely sensed measurements of stratocumulus properties during FIRE using the C130 aircraft multichannel radiometer. *J. Atmos. Sci.*, **47**, 2488–2503, https://doi.org/10.1175/1520-0469(1990)047<2488:RSMOSP>2.0.CO;2.

Reber, C. A., 1993: The Upper Atmosphere Research Satellite (UARS). *Geophys. Res. Lett.*, **20**, 1215–1218, https://doi.org/10.1029/93GL01103.

Reitebuch, O., 2012: The spaceborne wind lidar mission ADM-Aeolus. *Atmospheric Physics: Background, Methods, Trends*, U. Schumann, Ed., Research Topics in Aerospace, Springer, 815–827, https://doi.org/10.1007/978-3-642-30183-4_49.

Remer, L. A., and Coauthors, 2008: Global aerosol climatology from the MODIS satellite sensors. *J. Geophys. Res.*, **113**, D14S07, https://doi.org/10.1029/2007JD009661.

Riedi, J., and Coauthors, 2010: Cloud thermodynamic phase inferred from merged POLDER and MODIS data. *Atmos. Chem. Phys.*, **10**, 11 851–11 865, https://doi.org/10.5194/acp-10-11851-2010.

Rodgers, C. D., 2000: *Inverse Methods for Atmospheric Sounding: Theory and Practice*. World Scientific, 238 pp.

Romatschke, U., and R. A. Houze Jr., 2010: Extreme summer convection in South America. *J. Climate*, **23**, 3761–3791, https://doi.org/10.1175/2010JCLI3465.1.

——, and ——., 2011: Characteristics of precipitating convective systems in the south Asian monsoon. *J. Hydrometeor.*, **12**, 3–26, https://doi.org/10.1175/2010JHM1289.1.

Ross, A., R. E. Holz, and S. A. Ackerman, 2017: Correlations of oriented ice and precipitation in marine midlatitude low clouds using collocated, CloudSat, CALIOP, and MODIS observations. *J. Geophys. Res. Atmos.*, **122**, 8056–8070, https://doi.org/10.1002/2016JD026407.

Rossow, W. B., 1989: Measuring cloud properties from space: A review. *J. Climate*, **2**, 201–213, https://doi.org/10.1175/1520-0442(1989)002<0201:MCPFSA>2.0.CO;2.

——, and L. C. Garder, 1993: Cloud detection using satellite measurements of infrared and visible radiances for ISCCP. *J. Climate*, **6**, 2341–2369, https://doi.org/10.1175/1520-0442(1993)006<2341:CDUSMO>2.0.CO;2.

——, ——, and A. A. Lacis, 1989: Global, seasonal cloud variations from satellite radiance measurements. Part I: Sensitivity of analysis. *J. Climate*, **2**, 419–458, https://doi.org/10.1175/1520-0442(1989)002<0419:GSCVFS>2.0.CO;2.

Ruf, C. R., A. Lyons, M. Unwin, J. Dickinson, R. Rose, D. Rose, and M. Vincent, 2013: CYGNSS: Enabling the future of hurricane prediction. *IEEE Geosci. Remote Sens. Mag.*, **1**, 52–67, https://doi.org/10.1109/MGRS.2013.2260911.

——, C. Chew, T. Lang, M. G. Morris, K. Nave, A. Ridley, and R. Balasubramaniam, 2018: A new paradigm in Earth environmental monitoring with the CYGNSS small satellite constellation. *Sci. Rep.*, **8**, 8782, https://doi.org/10.1038/s41598-018-27127-4.

Rutan, D. A., S. Kato, D. R. Doelling, F. G. Rose, L. T. Nguyen, T. E. Caldwell, and N. G. Loeb, 2015: CERES Synoptic product: Methodology and validation of surface radiant flux. *J. Atmos. Oceanic Technol.*, **32**, 1121–1143, https://doi.org/10.1175/JTECH-D-14-00165.1.

Sahany, S., V. Venugopal, and R. S. Nanjundiah, 2010: Diurnal-scale signatures of monsoon rainfall over the Indian region from TRMM satellite observations. *J. Geophys. Res.*, **115**, D02103, https://doi.org/10.1029/2009JD012644.

Salomonson, V. V., W. L. Barnes, P.W. Maymon, H. E. Montgomery, and H. Ostrow, 1989: MODIS: Advanced facility instrument for studies of the Earth as a system. *IEEE*

Trans. Geosci. Remote Sens., **27**, 145–153, https://doi.org/10.1109/36.20292.

Saunders, R., and K. Kriebel, 1988: An improved method for detecting clear sky and cloudy radiances from AVHRR data. *Int. J. Remote Sens.*, **9**, 123–150, https://doi.org/10.1080/01431168808954841.

Sayer, A. M., L. A. Munchak, N. C. Hsu, R. C. Levy, C. Bettenhausen, and M.-J. Jeong, 2014: MODIS Collection 6 aerosol products: Comparison between Aqua's e-Deep Blue, Dark Target, and "merged" data sets, and usage recommendations. *J. Geophys. Res. Atmos.*, **119**, 13 965–13 989, https://doi.org/10.1002/2014JD022453.

Schmetz, J., P. Pili, S. Tjemkes, D. Just, J. Kerkmann, S. Rota, and A. Ratier, 2002: An introduction to Meteosat Second Generation (MSG). *Bull. Amer. Meteor. Soc.*, **83**, 977–992, https://doi.org/10.1175/1520-0477(2002)083<0977:AITMSG>2.3.CO;2.

Schmit, T. J., P. Griffith, M. M. Gunshor, J. M. Daniels, S. J. Goodman, and W. J. Lebair, 2017: A closer look at the ABI on the GOES-R series. *Bull. Amer. Meteor. Soc.*, **98**, 681–698, https://doi.org/10.1175/BAMS-D-15-00230.1.

——, S. S. Lindstrom, J. J. Gerth, and M. M. Gunshor, 2018: Applications of the 16 spectral bands on the Advanced Baseline Imager (ABI). *J. Oper. Meteor.*, **6**, 33–46, https://doi.org/10.15191/nwajom.2018.0604.

Scofield, R., and V. J. Oliver, 1977: A scheme for estimating convective rainfall from satellite imagery. NOAA Tech. Memo NESS 86, 47 pp., https://repository.library.noaa.gov/view/noaa/18514.

Seto, S., and T. Iguchi, 2015: Intercomparison of attenuation correction methods for the GPM Dual-Frequency Precipitation Radar. *J. Atmos. Oceanic Technol.*, **32**, 915–926, https://doi.org/10.1175/JTECH-D-14-00065.1.

Shepherd, J. M., S. Burian, C. Liu, and S. Bernardes, 2016: Satellite precipitation metrics to study the energy-water-food nexus within the backdrop of an urbanized globe. Earthzine, 31 May, https://earthzine.org/satellite-precipitation-metrics-to-study-the-energy-water-food-nexus-within-the-backdrop-of-an-urbanized-globe/.

Shige, S., Y. N. Takayabu, W.-K. Tao, and C.-L. Shie, 2007: Spectral retrieval of latent heating profiles from TRMM PR data. Part II: Algorithm improvement and heating estimates over tropical ocean regions. *J. Appl. Meteor. Climatol.*, **46**, 1098–1124, https://doi.org/10.1175/JAM2510.1.

Skofronick-Jackson, G., and Coauthors, 2017: The Global Precipitation Measurement (GPM) mission for science and society. *Bull. Amer. Meteor. Soc.*, **98**, 1679–1695, https://doi.org/10.1175/BAMS-D-15-00306.1.

Smith, N., K. D. White, E. Berndt, B. T. Zavodsky, A. Wheeler, M. A. Bowlan, and C. D. Barnet, 2018: NUCAPS in AWIPS—Rethinking information compression and distribution for fast decision making. *22nd Conf. on Satellite Meteorology and Oceanography*, Austin, TX, Amer. Meteor. Soc., 6A.6, https://ams.confex.com/ams/98Annual/webprogram/Paper336846.html.

Smith, W. L., 1968: An improved method for calculating tropospheric temperature and moisture from satellite radiometer measurements. *Mon. Wea. Rev.*, **96**, 387–396, https://doi.org/10.1175/1520-0493(1968)096<0387:AIMFCT>2.0.CO;2.

——, 1991: Atmospheric soundings from satellites—False expectation or the key to improved weather prediction? *Quart. J. Roy. Meteor. Soc.*, **117**, 267–297, https://doi.org/10.1002/qj.49711749802.

——, and Coauthors, 1986: The meteorological satellite: Overview of 25 years of operation. *Science*, **231**, 455–462, https://doi.org/10.1126/science.231.4737.455.

——, and Coauthors, 2009: Technical note: Evolution, current capabilities, and future advances in satellite ultra-spectral IR sounding of the lower atmosphere. *Atmos. Chem. Phys.*, **9**, 5563–5574, https://doi.org/10.5194/acp-9-5563-2009.

——, H. M. Woolf, P. G. Abel, C. M. Hayden, M. Chalfant, and N. Grody, 1974: Nimbus-5 sounder data processing system—Part I: Measurement characteristics and data reduction procedures. NOAA Tech. Memo. NESS 57, 99 pp., https://repository.library.noaa.gov/view/noaa/18552.

——, E. Weisz, S. Kirev, D. K. Zhou, Z. Li, and E. E. Borbas, 2012: Dual-regression retrieval algorithm for real-time processing of satellite ultraspectral radiances. *J. Appl. Meteor. Climatol.*, **51**, 1455–1476, https://doi.org/10.1175/JAMC-D-11-0173.1.

Soden, B. J., 1997: Variations in the tropical greenhouse effect during El Niño. *J. Climate*, **10**, 1050–1055, https://doi.org/10.1175/1520-0442(1997)010<1050:VITTGE>2.0.CO;2.

Stanley, T., and D. B. Kirschbaum, 2017: A heuristic approach to global landslide susceptibility mapping. *Nat. Hazards*, **87**, 145–164, https://doi.org/10.1007/s11069-017-2757-y.

Stano, G. T., C. J. Schultz, L. D. Carey, D. R. MacGorman, and K. M. Calhoun, 2014: Total lightning observations and tools for the 20 May 2013 Moore, Oklahoma, tornadic supercell. *J. Oper. Meteor*, **2**, 71–88, https://doi.org/10.15191/nwajom.2014.0207.

Stephens, G. L., G. G. Campbell, and T. H. V. Haar, 1981: Earth radiation budgets. *J. Geophys. Res.*, **86**, 9739–9760, https://doi.org/10.1029/JC086iC10p09739.

——, and Coauthors, 2002: The CloudSat Mission and the A-Train. *Bull. Amer. Meteor. Soc.*, **83**, 1771–1790, https://doi.org/10.1175/BAMS-83-12-1771.

——, and Coauthors, 2008: CloudSat Mission: Performance and early science after the first year of operation. *J. Geophys. Res.*, **113**, D00A18, https://doi.org/10.1029/2008JD009982.

——, M. Wild, J. P. W. Stackhouse, T. L'Ecuyer, S. Kato, and D. S. Henderson, 2012a: An update on the Earth's energy balance in light of new surface energy flux estimates. *Nat. Geosci.*, **5**, 691–696, https://doi.org/10.1038/ngeo1580.

——, ——, P. W. Stackhouse Jr., T. L'Ecuyer, S. Kato, and D. S. Henderson, 2012b: The global character of the flux of downward longwave radiation. *J. Climate*, **25**, 2329–2340, https://doi.org/10.1175/JCLI-D-11-00262.1.

——, D. Winker, J. Pelon, C. Trepte, D. Vane, C. Yuhas, T. L'Ecuyer, and M. Lebsock, 2018: *CloudSat* and *CALIPSO* within the A-Train: Ten years of actively observing the Earth system. *Bull. Amer. Meteor. Soc.*, **99**, 569–581, https://doi.org/10.1175/BAMS-D-16-0324.1.

Stowe, L. L., E. P. McClain, R. Carey, P. Pellegrino, G. Gutman, P. Davis, C. Long, and S. Hart, 1991: Global distribution of cloud cover derived from NOAA/AVHRR operational satellite data. *Adv. Space Res.*, **11**, 51–54, https://doi.org/10.1016/0273-1177(91)90402-6.

——, H. Jacobowitz, G. Ohring, K. R. Knapp, and N. R. Nalli, 2002: The Advanced Very High Resolution Radiometer (AVHRR) Pathfinder Atmosphere (PATMOS) climate dataset: Initial analyses and evaluations. *J. Climate*, **15**, 1243–1260, https://doi.org/10.1175/1520-0442(2002)015<1243:TAVHRR>2.0.CO;2.

Strabala, K. I., S. A. Ackerman, and W. P. Menzel, 1994: Cloud properties inferred from 8–12 μm data. *J. Appl. Meteor.*, **33**, 212–229, https://doi.org/10.1175/1520-0450(1994)033<0212:CPIFD>2.0.CO;2.

Stubenrauch, C. J., and Coauthors, 2013: Assessment of global cloud datasets from satellites: Project and database initiated by the GEWEX Radiation Panel. *Bull. Amer. Meteor. Soc.*, **94**, 1031–1049, https://doi.org/10.1175/BAMS-D-12-00117.1.

Su, W., J. Corbett, Z. Eitzen, and L. Liang, 2015: Next-generation angular distribution models for top-of-atmosphere radiative flux calculation from CERES instruments: Methodology. *Atmos. Meas. Tech.*, **8**, 611–632, https://doi.org/10.5194/amt-8-611-2015.

Sullivan, W., 1985: Low level ozone found above Antarctica. *New York Times*, 7 November, B21, https://www.nytimes.com/1985/11/07/us/low-ozone-level-found-above-antarctica.html.

Sun, B., A. Reale, F. H. Tilley, M. E. Pettey, N. R. Nalli, and C. D. Barnet, 2017: Assessment of NUCAPS S-NPP CrIS/ATMS sounding products using reference and conventional radiosonde observations. *IEEE J. Sel. Top. Appl. Earth Obs. Remote Sens.*, **10**, 2499–2509, https://doi.org/10.1109/JSTARS.2017.2670504.

Suomi, V. E., and R. Parent, 1968: A color view of planet Earth. *Bull. Amer. Meteor. Soc.*, **49**, 74–75, https://doi.org/10.1175/1520-0477-49.2.74.

Susskind, J., C. D. Barnet, and J. M. Blaisdell, 2003: Retrieval of atmospheric and surface parameters from AIRS/AMSU/HSB data in the presence of clouds. *IEEE Trans. Geosci. Remote Sens.*, **41**, 390–409, https://doi.org/10.1109/TGRS.2002.808236.

——, J. M. Blaisdell, L. Iredell, and F. Keita, 2011: Improved temperature sounding and quality control methodology using AIRS/AMSU data: The AIRS science team version 5 retrieval algorithm. *IEEE Trans. Geosci. Remote Sens.*, **49**, 883–907, https://doi.org/10.1109/TGRS.2010.2070508.

Suttles, J. T., and Coauthors, 1988: Angular radiation models for Earth–atmosphere systems: Volume I—Shortwave radiation. NASA Reference Publ. 1184, Vol. I, 144 pp., https://ntrs.nasa.gov/archive/nasa/casi.ntrs.nasa.gov/19880018293.pdf.

——, R. N. Green, G. L. Smith, B. A. Wielicki, I. J. Walker, V. R. Taylor, and L. L. Stowe, 1989: Angular radiation models for earth–atmosphere systems: Volume II—Longwave radiation. NASA Reference Publ. 1184, Vol. II, 84 pp., https://ntrs.nasa.gov/archive/nasa/casi.ntrs.nasa.gov/19890011216.pdf.

Takahashi, H. G., H. Fujinami, T. Yasunari, and J. Matsumoto, 2010: Diurnal rainfall pattern observed by Tropical Rainfall Measuring Mission Precipitation Radar (TRMM-PR) around the Indochina peninsula. *J. Geophys. Res.*, **115**, D07109, https://doi.org/10.1029/2009JA015243.

Takayabu, Y. N., 2006: Rain-yield per flash calculated from TRMM PR and LIS data and its relationship to the contribution of tall convective rain. *Geophys. Res. Lett.*, **33**, L18705, https://doi.org/10.1029/2006GL027531.

Tan, B. Z., W. A. Petersen, and A. Tokay, 2016: A novel approach to identify sources of errors in IMERG for GPM ground validation. *J. Hydrometeor.*, **17**, 2477–2491, https://doi.org/10.1175/JHM-D-16-0079.1.

Tao, W.-K., S. Lang, X. Zeng, S. Shige, and Y. Takayabu, 2010: Relating convective and stratiform rain to latent heating. *J. Climate*, **23**, 1874–1893, https://doi.org/10.1175/2009JCLI3278.1.

——, and Coauthors, 2013: Precipitation intensity and variation during MC3E: A numerical modeling study. *J. Geophys. Res. Atmos.*, **118**, 7199–7218, https://doi.org/10.1002/jgrd.50410.

Tapiador, F. J., and Coauthors, 2017: Global precipitation measurements for validating climate models. *Atmos. Res.*, **197**, 1–20, https://doi.org/10.1016/j.atmosres.2017.06.021.

Torres, O., P. K. Bhartia, J. R. Herman, Z. Ahmad, and J. Gleason, 1998: Derivation of aerosol properties from satellite measurements of backscattered ultraviolet radiation: Theoretical basis. *J. Geophys. Res.*, **103**, 17 099–17 110, https://doi.org/10.1029/98JD00900.

Trenberth, K. E., and J. T. Fasullo, 2017: Atlantic meridional heat transports computed from balancing Earth's energy locally. *Geophys. Res. Lett.*, **44**, 1919–1927, https://doi.org/10.1002/2016GL072475.

Trepte, Q. Z., and Coauthors, 2019: Global cloud detection for CERES Edition 4 using Terra and Aqua MODIS data. *IEEE Trans. Geosci. Remote Sens.*, in press.

Trishchenko, A. P., L. Garand, L. D. Trichtchenko, and L. V. Nikitina, 2016: Multiple-apogee highly elliptical orbits for continuous meteorological imaging of polar regions: challenging the classical 12-h Molniya orbit concept. *Bull. Amer. Meteor. Soc.*, **97**, 19–24, https://doi.org/10.1175/BAMS-D-14-00251.1.

Twomey, S., and T. Cocks, 1989: Remote sensing of cloud parameters from spectral reflectance measurements in near-infrared. *Beitr. Phys. Atmos.*, **62**, 172–179.

Uhlenbrock, N. L., K. M. Bedka, W. F. Feltz, and S. A. Ackerman, 2007: Mountain waves signatures in MODIS 6.7-μm imagery and their relation to pilot reports of turbulence. *Wea. Forecasting*, **22**, 662–670, https://doi.org/10.1175/WAF1007.1.

Vanbauce, C., J. Buriez, F. Parol, B. Bonnel, G. Seze, and P. Couvert, 1998: Apparent pressure derived from ADEOS-POLDER observations in the oxygen A-band over ocean. *Geophys. Res. Lett.*, **25**, 3159–3162, https://doi.org/10.1029/98GL02324.

van Diedenhoven, B., A. Fridlind, A. Ackerman, and B. Cairns, 2012: Evaluation of hydro- meteor phase and ice properties in cloud-resolving model simulations of tropical deep convection using radiance and polarization measurements. *J. Atmos. Sci.*, **69**, 3290–3314, https://doi.org/10.1175/JAS-D-11-0314.1.

Van Tricht, K., and Coauthors, 2016: Clouds enhance Greenland ice sheet meltwater runoff. *Nat. Commun.*, **7**, https://doi.org/10.1038/ncomms10266.

Velden, C. S., 1987: Satellite observations of hurricane Elena (1985) using the VAS 6.7-μm "water vapor" channel. *Bull. Amer. Meteor. Soc.*, **68**, 210–215, https://doi.org/10.1175/1520-0477(1987)068<0210:SOOHEU>2.0.CO;2.

——, and W. L. Smith, 1983: Monitoring tropical cyclone evolution with NOAA satellite microwave observations. *J. Climate Appl. Meteor.*, **22**, 714–724, https://doi.org/10.1175/1520-0450(1983)022<0714:MTCEWN>2.0.CO;2.

——, ——, and M. Mayfield, 1984: Applications of VAS and TOVS to tropical cyclones. *Bull. Amer. Meteor. Soc.*, **65**, 1059–1067, https://doi.org/10.1175/1520-0477(1984)065<1059:AOVATT>2.0.CO;2.

——, T. L. Olander, and R. M. Zehr, 1998: Development of an objective scheme to estimate tropical cyclone intensity from digital geostationary satellite infrared imagery. *Wea. Forecasting*, **13**, 172–186, https://doi.org/10.1175/1520-0434(1998)013<0172:DOAOST>2.0.CO;2.

Vernier, J.-P., and Coauthors, 2011: Major influence of tropical volcanic eruptions on the stratospheric aerosol layer during the last decade. *Geophys. Res. Lett.*, **38**, L12807, https://doi.org/10.1029/2011GL047563.

Vianna, M. L., V. V. Menezes, A. B. Pezza, and I. Simmonds, 2010: Interactions between Hurricane Catarina (2004) and warm core rings in the South Atlantic Ocean. *J. Geophys. Res. Oceans*, **115**, C07002, https://doi.org/10.1029/2009JC005974.

von Schuckmann, K., and Coauthors, 2016: An imperative to monitor Earth's energy imbalance. *Nat. Climate Change*, **6**, 138–144, https://doi.org/10.1038/nclimate2876.

Vonder Haar, T. H., 1994: The global energy budget and satellite observations. *Adv. Space Res.*, **14**, 131–144, https://doi.org/10.1016/0273-1177(94)90362-X.

——, and V. E. Suomi, 1969: Satellite observations of the Earth's radiation budget. *Science*, **163**, 667–669, https://doi.org/10.1126/science.163.3868.667.

——, ——, E. Raschke, M. Pasternak, and W. Bandeen, 1972: The radiation budget of the Earth-atmosphere system as measured from the Nimbus 3 satellite (1969–1970). *Space Res.*, **12**, 491–498.

Waliser, D., and Coauthors, 2009: MJO simulation diagnostics. *J. Climate*, **22**, 3006–3030, https://doi.org/10.1175/2008JCLI2731.1.

Wang, C., S. Platnick, Z. Zhang, K. Meyer, G. Wind, and P. Yang, 2016: Retrieval of ice cloud properties using an optimal estimation algorithm and MODIS infrared observations: 2. Retrieval evaluation. *J. Geophys. Res. Atmos.*, **121**, 5827–5845, https://doi.org/10.1002/2015JD024528.

Wang, J., and S. A. Christopher, 2003: Intercomparison between satellite-derived aerosol optical thickness and PM2.5 mass: Implications for air quality studies. *Geophys. Res. Lett.*, **30**, 2095, https://doi.org/10.1029/2003GL018174.

Waquet, F., and Coauthors, 2013: Retrieval of aerosol microphysical and optical properties above liquid clouds from POLDER/PARASOL polarization measurements. *Atmos. Meas. Tech.*, **6**, 991–1016, https://doi.org/10.5194/amt-6-991-2013.

Ward, A., 2015: Nimbus celebrates fifty years. *The Earth Observer*, Vol. 27 (2), NASA Science Communications Support Office, Greenbelt MD, 18–31, https://eospso.nasa.gov/earthobserver/mar-apr-2015.

Ware, R., and Coauthors, 1996: GPS Sounding of the atmosphere from low Earth orbit: Preliminary results. *Bull. Amer. Meteor. Soc.*, **77**, 19–40, https://doi.org/10.1175/1520-0477(1996)077<0019:GSOTAF>2.0.CO;2.

Weinstein, M., and V. E. Suomi, 1961: Analysis of satellite infrared radiation measurements on a synoptic scale. *Mon. Wea. Rev.*, **89**, 419–428, https://doi.org/10.1175/1520-0493-89.11.419.

Weisz, E., H.-L. Huang, J. Li, E. Borbas, and K. Baggett, 2007: International MODIS and AIRS processing package: AIRS products and applications. *J. Appl. Remote Sens.*, **1**, 013519, https://doi.org/10.1117/1.2766867.

——, W. L. Smith, and N. Smith, 2013: Advances in simultaneous atmospheric profile and cloud parameter regression based retrieval from high-spectral resolution radiance measurements. *J. Geophys. Res. Atmos.*, **118**, 6433–6443, https://doi.org/10.1002/jgrd.50521.

——, N. Smith, and W. L. Smith, 2015: The use of hyperspectral sounding information to monitor atmospheric tendencies leading to severe local storms. *Earth Space Sci.*, **2**, 369–377, https://doi.org/10.1002/2015EA000122.

Weldon, R. B., and S. J. Holmes, 1991: Water vapor imagery: Interpretation and applications to weather analysis and forecasting. NOAA Tech. Rep. NESDIS 57, 213 pp.

Wen, Y., P. Kirstetter, Y. Hong, J. J. Gourley, Q. Cao, J. Zhang, Z. Flamig, and X. Xue, 2016: Evaluation of a method to enhance real-time, ground radar based rainfall estimates using climatological profiles of reflectivity from space. *J. Hydrometeor.*, **17**, 761–775, https://doi.org/10.1175/JHM-D-15-0062.1.

Wentz, F. J., 1997: A well calibrated ocean algorithm for special sensor microwave / imager. *J. Geophys. Res.*, **102**, 8703–8718, https://doi.org/10.1029/96JC01751.

——, and D. Draper, 2016: On-orbit absolute calibration of the Global Precipitation Measurement Microwave Imager. *J. Atmos. Oceanic Technol.*, **33**, 1393–1412, https://doi.org/10.1175/JTECH-D-15-0212.1.

Werner, F., G. Wind, Z. Zhang, S. Platnick, L. Di Girolamo, G. Zhao, N. Amarasinghe, and K. Meyer, 2016: Marine boundary layer cloud property retrievals from high-resolution ASTER observations: case studies and comparison with Terra MODIS. *Atmos. Meas. Tech.*, **9**, 5869–5894, https://doi.org/10.5194/amt-9-5869-2016.

Wexler, H., 1954: Observing the weather from a satellite vehicle. *J. Br. Interplanet. Soc.*, **13**, 269–276.

Wheeler, A., N. Smith, A. Gambacorta, C. D. Barnet, and M. Goldberg, 2018: Evaluation of NUCAPS products in AWIPS-II: results from the 2017 HWT. *14th Annual Symp. on New Generation Operational Environmental Satellite Systems*, Austin, TX, Amer. Meteor. Soc., 237, https://ams.confex.com/ams/98Annual/webprogram/Paper337401.html.

Wielicki, B. A., B. R. Barkstrom, E. F. Harrison, R. B. Lee III, G. L. Smith, and J. E. Cooper, 1996: Clouds and the Earth's Radiant Energy System (CERES): An Earth observing system experiment. *Bull. Amer. Meteor. Soc.*, **77**, 853–868, https://doi.org/10.1175/1520-0477(1996)077<0853:CATERE>2.0.CO;2.

Wimmers, A. J., and C. S. Velden, 2011: Seamless advective blending of total precipitable water retrievals from polar-orbiting satellites. *J. Appl. Meteor. Climatol.*, **50**, 1024–1036, https://doi.org/10.1175/2010JAMC2589.1.

Winker, D. M., R. H. Couch, and M. P. McCormick, 1996: An overview of LITE: NASA's Lidar In-space Technology Experiment. *Proc. IEEE*, **84**, 164–180, https://doi.org/10.1109/5.482227.

——, W. H. Hunt, and M. J. McGill, 2007: Initial performance assessment of CALIOP. *Geophys. Res. Lett.*, **34**, L19803, https://doi.org/10.1029/2007GL030135.

——, and Coauthors, 2010: The CALIPSO mission: A global 3D view of aerosols and clouds. *Bull. Amer. Meteor. Soc.*, **91**, 1211–1229, https://doi.org/10.1175/2010BAMS3009.1.

——, J. L. Tackett, B. J. Getzewich, Z. Liu, M. A. Vaughan, and R. R. Rogers, 2013: The global 3-D distribution of tropospheric aerosols as characterized by CALIOP. *Atmos. Chem. Phys.*, **13**, 3345–3361, https://doi.org/10.5194/acp-13-3345-2013.

Wolfe, R. E., G. Lin, M. Nishihama, K. P. Mewari, J. C. Tilton, and A. R. Isaacman, 2013: Suomi NPP VIIRS prelaunch and on-orbit geometric calibration and characterization. *J. Geophys. Res. Atmos.*, **118**, 11 508–11 521, https://doi.org/10.1002/jgrd.50873.

Wood, R., and D. L. Hartmann, 2006: Spatial variability of liquid water path in marine low clouds: Part I. Probability distribution and mesoscale cellular scales. *J. Climate*, **19**, 1748–1764, https://doi.org/10.1175/JCLI3702.1.

——, and Coauthors, 2018: Ultraclean layers and optically thin clouds in the stratocumulus transition: Part I: Observations. *J. Atmos. Sci.*, **75**, https://doi.org/10.1175/JAS-D-17-0213.1.

Wright, D. B., D. B. Kirschbaum, and S. Yatheendradas, 2017: Satellite precipitation characterization, error modeling, and error correction using censored shifted gamma distributions. *J. Hydrometeor.*, **18**, 2801–2815, https://doi.org/10.1175/JHM-D-17-0060.1.

Wu, H., R. F. Adler, Y. Tian, G. J. Huffman, H. Li, and J. Wang, 2014: Real-time global flood estimation using satellite-based precipitation and a coupled land surface and routing model. *Water Resour. Res.*, **50**, 2693–2717, https://doi.org/10.1002/2013WR014710.

Wylie, D. P., and W. P. Menzel, 1989: Two years of cloud cover statistics using VAS. *J. Climate*, **2**, 380–392, https://doi.org/10.1175/1520-0442(1989)002<0380:TYOCCS>2.0.CO;2.

——, ——, H. M. Woolf, and K. I. Strabala, 1994: Four years of global cirrus cloud statistics using HIRS. *J. Climate*, **7**, 1972–1986, https://doi.org/10.1175/1520-0442(1994)007<1972:FYOGCC>2.0.CO;2.

Xi, B., X. Dong, P. Minnis, and S. Sun-Mack, 2014:Comparison of marine boundary layer cloud properties from CERES-MODIS Edition 4 and DOE ARM AMF measurements at the Azores. *J. Geophys. Res. Atmos.*, **119**, 9509–9529, https://doi.org/10.1002/2014JD021813.

Xie, P., and P. A. Arkin, 1995: An intercomparison of gauge observations and satellite estimates of monthly precipitation. *J. Appl. Meteor.*, **34**, 1143–1160, https://doi.org/10.1175/1520-0450(1995)034<1143:AIOGOA>2.0.CO;2.

——, and ——, 1997: Global precipitation: A 17-year monthly analysis based on gauge observations, satellite estimates, and numerical model outputs. *Bull. Amer. Meteor. Soc.*, **78**, 2539–2558, https://doi.org/10.1175/1520-0477(1997)078<2539:GPAYMA>2.0.CO;2.

Xiong, X., and Coauthors, 2014: VIIRS on-orbit calibration methodology and performance. *J. Geophys. Res. Atmos.*, **119**, 5065–5078, https://doi.org/10.1002/2013JD020423.

Xu, K.-M., and A. Cheng, 2013a: Evaluating low-cloud simulation from an upgraded multiscale modeling framework model. Part I: Sensitivity to spatial resolution and climatology. *J. Climate*, **26**, 5717–5740, https://doi.org/10.1175/JCLI-D-12-00200.1.

——, and ——, 2013b: Evaluating low-cloud simulation from an upgraded multiscale modeling framework model. Part II: Seasonal variations over the Eastern Pacific. *J. Climate*, **26**, 5741–5760, https://doi.org/10.1175/JCLI-D-12-00276.1.

Yang, P., L. Zhang, G. Hong, S. L. Nasiri, B. A. Baum, H.-L. Huang, M. D. King, and S. Platnick, 2007: Differences between collection 4 and 5 MODIS ice cloud optical/microphysical products and their impact on radiative forcing simulations. *IEEE Trans. Geosci. Remote Sens.*, **45**, 2886–2899, https://doi.org/10.1109/TGRS.2007.898276.

Yost, C. R., and Coauthors, 2018: A prototype method for diagnosing high ice water content probability using satellite imager data. *Atmos. Meas. Tech.*, **11**, 1615–1637, https://doi.org/10.5194/amt-11-1615-2018.

You, Y., N.-Y. Wang, R. Ferraro, and S. Rudlosky, 2017: Quantifying the snowfall detection performance of the GPM Microwave Imager channels over land. *J. Hydrometeor.*, **18**, 729–751, https://doi.org/10.1175/JHM-D-16-0190.1.

Yu, H., and Coauthors, 2015: Quantification of trans-Atlantic dust transport from seven-year (2007–2013) record of CALIPSO lidar measurements. *Remote Sens. Environ.*, **159**, 232–249, https://doi.org/10.1016/j.rse.2014.12.010.

Yumimoto, K., and T. Takemura, 2015: Long-term inverse modeling of Asian dust: Interannual variations of its emission, transport, deposition and radiative forcing. *J. Geophys. Res. Atmos.*, **120**, 1582–1607, https://doi.org/10.1002/2014JD022390.

Zhang, S. Q., T. Matsui, S. Cheung, M. Zupanski, and C. Peters-Lidard, 2017: Impact of assimilated precipitation-sensitive radiances on the NU-WRF simulation of West African monsoon. *Mon. Wea. Rev.*, **145**, 3881–3900, https://doi.org/10.1175/MWR-D-16-0389.1.

Zhang, Z., and S. Platnick, 2011: An assessment of differences between cloud effective particle radius for marine water clouds from three MODIS spectral bands. *J. Geophys. Res.*, **116**, D20215, https://doi.org/10.1029/2011JD016216.

——, X. Dong, B. Xi, H. Song, P.-L. Ma, S. Ghan, S. Platnick, and P. Minnis, 2017: Intercomparisons of marine boundary layer cloud properties from the ARM CAP-MBL campaign and two MODIS cloud products. *J. Geophys. Res. Atmos.*, **122**, 2351–2365, https://doi.org/10.1002/2016JD025763.

Zhao, B., and Coauthors, 2017: Decadal-scale trends in regional aerosol particle properties and their linkage to emission changes. *Environ. Res. Lett.*, **12**, 054021, https://doi.org/10.1088/1748-9326/aa6cb2.

Zhou, C., M. D. Zelinka, A. E. Dessler, and S. A. Klein, 2015: The relationship between interannual and long-term cloud feedbacks. *Geophys. Res. Lett.*, **42**, 10 463–10 469, https://doi.org/10.1002/2015GL066698.

Zhao, X., A. K. Heidinger, and A. Walther, 2016: Climatology analysis of aerosol effect on marine water cloud from long-term satellite climate data records. *Remote Sens.*, **8**, 300, https://doi.org/10.3390/rs8040300.

Ziemke, J. R., S. Chandra, and P. K. Bhartia, 1998: Two new methods for deriving tropospheric column ozone from TOMS measurements: The assimilated UARS MLS/HALOE and convective cloud differential techniques. *J. Geophys. Res.*, **103**, 22 115–22 127, https://doi.org/10.1029/98JD01567.

——, ——, B. N. Duncan, L. Froidevaux, P. K. Bhartia, P. F. Levelt, and J. W. Waters, 2006: Tropospheric ozone determined from Aura OMI and MLS: Evaluation of measurements and comparison with the Global Modeling Initiative's Chemical Transport Model. *J. Geophys. Res.*, **111**, D19303, https://doi.org/10.1029/2006JD007089.